Associate Professorship of Molecular Electronics
Department of Electrical and Computer Engineering
Technical University of Munich

Memristive switching in self-assembled nanoparticle composites

Maximilian Speckbacher
Professur für Molekularelektronik
Fakultät für Elektrotechnik und Informationstechnik

Vollständiger Abdruck der von der Fakultät für Elektrotechnik und Informationstechnik der Technischen Universität München zur Erlangung des akademischen Grades eines
Doktors der Naturwissenschaften (Dr. rer. nat.)
genehmigten Dissertation.

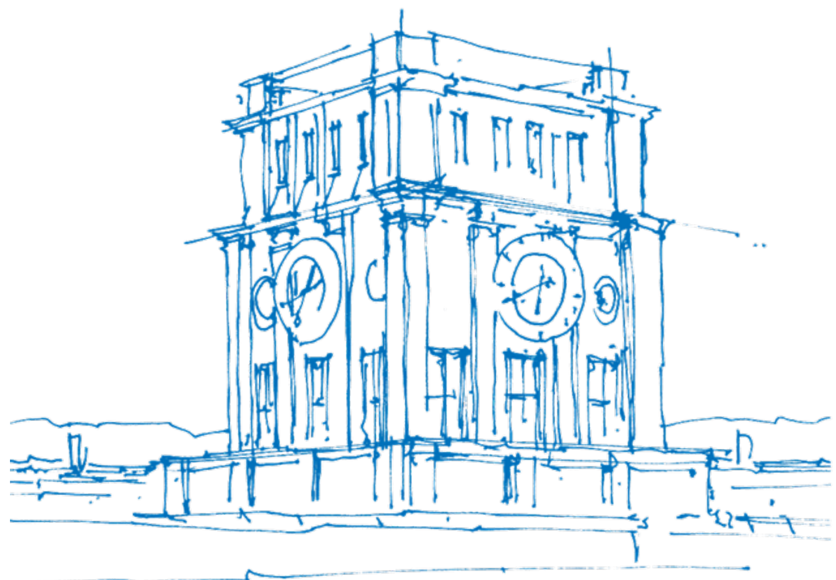

Associate Professorship of Molecular Electronics
Department of Electrical and Computer Engineering
Technical University of Munich

Fakultät für Elektrotechnik und Informationstechnik
Professur für Molekularelektronik

Memristive switching in self-assembled nanoparticle composites

Maximilian Speckbacher

Vollständiger Abdruck der von der Fakultät für Elektrotechnik und Informationstechnik der Technische Universität München zur Erlangung des akademischen Grades eines
Doktors der Naturwissenschaften (Dr. rer. nat.)
genehmigten Dissertation.

Vorsitzende(r): Prof. Dr. Erwin Biebl
Prüfer der Dissertation:

1. Prof. Dr. Marc Tornow
2. Priv.-Doz. Dr. Gregor Koblmüller

Die Dissertation wurde am 20.11.2019 bei der Technische Universität München eingereicht und durch die Fakultät für Elektrotechnik und Informationstechnik am 20.05.2020 angenommen.

Abstract

In post-Moore's law era, besides integration of novel materials, also new fabrication and device concepts towards the third dimension are intensively discussed and investigated. However, to date these novel concepts are based on top-down fabrication approaches, restricting down-scaling options, material variation and complexity of systems. Therefore, bottom-up approaches such as self-assembly of functional building blocks are promising candidates to overcome these restrictions. Such self-organized devices should i) form in a well-defined, directed manner, ii) find their place on-chip for integration into electrical circuitry and iii) deliver a certain electrical function reliably. In the course of this work, these issues were addressed by developing concepts for directed self-assembly of nanoparticle-based functional building blocks and for immobilization of respective structures on-chip for future device integration.
Towards autonomous on-chip integration of functional building blocks, site-selective immobilization via self-assembly of silver nanocubes (AgNCs) with sizes of 100 nm into highly ordered arrays on oxide surface was demonstrated using a 'click'-reaction based self-assembly approach. For this purpose, highly doped Si wafers were coated by thin titanium dioxide (TiO_2) layers with a thickness of 2 nm to 20 nm by sputter coating and oxygen plasma oxidation. Subsequently, these oxide layers were patterned by arrays of square-shaped p-azidophenyltrimethoxysilane (APTMS) SAMs by evaporating molecules into holes, which were previously defined by electron-beam lithography (EBL), from the gas phase. After removal of the EBL resist, remaining SAM areas then act as immobilization sites for AgNCs in the subsequent self-assembly process, with AgNCs having previously been surface functionalized by SAMs of thiols featuring alkyne terminal groups. Performing self-assembly in solution with Cu(I)-catalyst, azide-alkyne 1,3-cycloaddtion yielded covalent triazole bonds between particles and substrate. This way, AgNC arrays were successfully formed with a yield of ~36 % of particles being immobilized at anticipated positions. Hence, for the first time best to our knowledge, single-particle immobilization solely based on molecular recognition was demonstrated. Single particles contacted in conductive-probe atomic force microscopy (CP-AFM) configuration featured pronounced threshold switching behavior with ultra-low off currents in the sub-pA range, steep turn-on slopes $<$50 mV/decade and a selectivity of $\sim 10^3$ making them suitable for future integration as selectors in cross-bar arrays for the suppression of sneak-path currents. In-depth investigation of conductive filaments in the oxide layer formed during electro-forming by ex-situ experimental methods and kinetic Monte-Carlo (kMC) simulations confirmed a switching mechanism based on conductive metal filaments. In addition, filament formation times in the order of a few

100 ms obtained by kMC simulations were in good agreement with experimental values.
As a next step, the directed self-assembly of fully functional memristive switching units was shown, only consisting of two nanoparticles (NPs) of different materials. For this purpose, AgNCs and spherical, chemically synthesized Si-nanoparticles (SiNPs) (size ~60 nm) were assembled into binary oligomers using different thiol- and silane-based surfactants in polar solvents. Resulting agglomerate geometries mainly yielded side facets of single AgNCs covered by one or more SiNP. Tuning surfactant and polarity of solvents, aggregate sizes could be effectively tuned between quadromers and trimers. Single AgNC-SiNP-dimers were electrically contacted by drop-casting onto interdigitated nanogap electrodes, with the AgNC and the poly-crystalline SiNP acting as active electrode and solid electrolyte, respectively, in an electrochemical metallization cell (ECM) configuration. DC-IV sweeps of NP-dimer memristors showed non-volatile bipolar memristive switching with narrow distribution of SET voltages of $\overline{V_{SET}}$ =(3.1 ± 0.2) V and an ON/OFF-state ratio of ~10^3. Additional excellent retention properties make this binary NP-system well suitable for non-volatile data storage applications.
To fabricate additional promising building blocks based on Si, the fabrication, functionalization and directed self-assembly of highly doped Si-nanocubes (SiNCs) with edge-length of 110 nm was investigated. SiNCs were first fabricated by electron-beam lithography (EBL) and reactive-ion etching (RIE) out of device layers of silicon-on-insulator (SOI) wafers. To enhance SiNC yield, nano-imprint lithography (NIL) was used next, yielding an amount of ~2x10^7 particles on a typical sample. Providing cubic NP geometry is of particular interest, as it potentially offers the possibility of side-selective functionalization and therefore selective assembly of different agglomerate geometries. As a first step in this direction, dispersion and directed SiNC-agglomerate assembly in dispersion was subsequently demonstrated following a silane-based 'click' reaction approach. This reaction forms covalent triazole bonds between adjacent SiNCs, with SiNCs being functionalized by SAMs of trimethoxysilane surfactants featuring complementary terminal groups prior to self-assembly. Reference cycloaddtion experiments using same SAMs on planar substrates indicated successful formation of anticipated reaction products.

Zusammenfassung

In der heutigen Zeit, in der das Moore'sche Gesetz nur noch eingeschränkt gültig ist, werden nicht nur die Einbindung neuartiger Materialien, sondern auch neuartige Herstellungs- und Bauteilkonzepte in die dritte Dimension intensiv diskutiert und untersucht. Diese neuen Konzepte basieren jedoch auf Top-down-Herstellungsprozessen, welche Miniaturisierungsmöglichkeiten sowie die Möglichkeit der Variation von Materialien und die Komplexität der Systeme einschränkt. In dieser Hinsicht sind Bottom-up-Ansätze wie die Selbst-Assemblierung von funktionalen Bausteinen vielversprechend, um diese Einschränkungen zu umgehen. Solche selbst-organisierten Bauteile sollten i) sich in einer wohldefinierten und gerichteten Weise bilden, ii) ihren Platz auf einer Oberfläche für die Einbindung in etwaige elektronische Schaltkreise selbstständig finden, und iii) eine spezielle elektrische Funktion auf zuverlässige Weise erfüllen. Im Laufe dieser Arbeit wurden diese Problemstellungen adressiert, indem Konzepte entwickelt wurden, um nanopartikel-basierte funktionale Bausteine auf gerichtete Weise zu assemblieren und um etwaige Strukturen auf Oberflächen auf geordnete Weise zu binden.
Auf dem Weg in Richtung der eigenständigen Einbindung von funktionalen Bausteinen auf Oberflächen wurde die platzspezifische Immobilisierung von Silber-Nanowürfeln (SNW) mit einer Größe von 100 nm mittels Selbst-Assemblierung in geordnete Matrizen auf Oxidoberflächen gezeigt. Dies geschah unter Anwendung einer Selbst-Assemblierungsmethode, die auf einer chemischen "Klick"-Reaktion basiert. Hierfür wurden zuerst Silizium-Wafer mit hoher p-Typ Dotierkonzentration mit Dünnschichten aus Titanoxid (TiO_2) mit einer Dicke zwischen 2 nm und 20 nm mittels Sputter-Abscheidung und Oxidation in Sauerstoffplasma beschichtet. Danach wurden diese Oxidschichten mit Matrizen aus selbst-assemblierten Monolagen (SAM) aus p-Azidophenyltrimethoxysilan Molekülen beschichtet, welche die Form von Rechtecken aufwiesen. Die Strukturierung und Gasphasenabscheidung dieser SAMs erfolgte mittels Lacklöchern, welche zuvor durch Elektronenstrahllithografie aufgebracht wurden. Nach dem Entfernen des Elektronenstrahllacks dienten die strukturierten SAM-Bereiche als Bindungsplätze für SNW im anschließenden Selbst-Assemblierungsprozess, wobei die Oberfläche der SNW zuvor mit Thiolen funktionalisiert wurde, welche Alkin-Endgruppen aufwiesen. Während der Durchführung des Selbst-Assemblierungsprozesses in Lösung mit Kupfer(I)-Katalysator wurden über Azid-Alkin 1,3-Zykloaddition kovalente Triazol-Bindungen zwischen Partikeln und dem Substrat gebildet. Hierdurch wurden erfolgreich geordnete Strukturen aus SNW gebildet, wobei ein Anteil von ~36 % an SNW an vorgegebenen Stellen immobilisiert wurde. Folglich wurde zu ersten mal, soweit bekannt, die Immobilisierung von einzelnen Partikeln, ausschließlich

basierend auf molekularer Erkennung, gezeigt. Einzelne Partikel, welche mittels Rasterkraftmikroskopie kontaktiert wurden, zeigten ausgeprägtes Schwellspannungs-Schaltverhalten mit sehr kleinen Leckströmen im Sub-pA-Bereich, steile Anschaltsteigungen <50 mV/Dekade und eine Selektivität von $\sim 10^3$. Diese Parameter machen diese Bauteile geeignet für die zukünftige Integration in Kreuzkontakt-Bauteilen, wo sie zum Unterdrücken sogenannter "Kriechströme" eingesetzt werden könnten. Die detaillierte Untersuchung leitfähiger Filamente, welche sich in der Oxidschicht während des Einschaltvorgangs gebildet hatten, mittels experimenteller ex-situ Methoden und kinetischen Monte-Carlo (kMC) Simulationen bestätigten die Annahme eines auf metallischen Filamenten basierenden Schaltmechanismus. Mittels kMC Simulationen wurden Filamentbildungszeiten im Bereich einiger 100 ms erhalten, welche gut mit experimentell bestimmten Werten übereinstimmen.

Als nächstes wurde die gerichtete Selbst-Assemblierung von voll funktionsfähigen memristiven Schaltbauteilen gezeigt, welche aus nur zwei verschiednen NP-Sorten bestanden. Zu diesem Zweck wurden SNW und sphärische, chemisch synthetisierte Si-Nanopartikel (SiNP) (Größe ca. 60 nm) zu binären Oligomeren mittels unterschiedlicher Netzmittel und polarer Lösemittel assembliert. Resultierende Agglomerat-Geometrien lagen hauptsächlich als einzelne SNW, benetzt mit einem oder mehreren SiNP vor. Durch Veränderung der Netzmittel und der Polarität der Lösemittel konnte die Größe der Aggregate zwischen Quadrumeren und Trimeren verändert werden. Einzelne SNW-SiNP-Dimere wurden durch Tropfen und Trocknen der entsprechenden Dispersion auf interdigitale Fingerstrukturen kontaktiert, wobei der SNW und der SiNP als aktive Elektrode bzw. Elektrolyt wie in einer Elektrochemischen Metallisierungszelle fungierten. Strom-Spannungskurven an NP-Dimeren zeigte nicht-volatiles, bipolares memristives Schaltverhalten mit einer engen Verteilung der Set-Spannung von $\overline{V_{SET}} = (3.1 \pm 0.2)$ V und einem Aus/An-Widerstandsverhältnis von $\sim 10^3$. Zusätzlich sehr gute Lebensdauer Eigenschaften machen dieses binäre NP-System gut geeignet für nicht-volatile Datenspeicherung.

Um zusätzlich vielversprechende Bausteine basierend auf Si zu realisieren wurde die Herstellung, Funktionalisierung und die gerichtete Selbst-Assemblierung von hoch-dotierten Si-Nanowürfeln (SiNW) mit einer Kantenlänge von 110 nm untersucht. SiNW wurden zuerst mittels Elektronentrahllithographie und reaktivem Ionenätzen aus der aktiven Schicht von Si-auf-Isolator Wafern hergestellt. Um die Ausbeute zu erhöhen wurde als nächstes Nano-Imprintlithografie verwendet, wodurch eine Anzahl von $\sim 2 \mathrm{x} 10^7$ Partikeln pro Probe erzielt wurde. Kubische NP-Form zu erhalten ist besonders interessant, da es die Möglichkeit seitenspezifischer Oberfunktionalisierung und deshalb die gerichtete Assemblierung verschiedener Agglomeratgeometrien ermöglicht. Als erster Schritt in diese Richtung wurde das Dispergieren und die gerichtete Assemblierung von SiNW-Agglomeraten in Lösung gezeigt, durch Folgen eines Silan-basierten "Klick"-Reaktionsansatzes. Diese Reaktion bildet kovalente Triazolbindungen zwischen sich berührenden SiNW wenn sie vor der Selbst-Assemblierung mit SAMs, die komplementäre Endgruppen aufweisen, funktionalisiert wurden. Referenzexperimente an

SAMs auf planaren Proben zeigte, dass das Reaktionsschema erfolgreich durchgeführt werden kann.

Contents

Abstract i

List of abbreviations xi

1 Introduction 1

2 Theoretical background 5
2.1 Nanoparticles and colloidal self-assembly . . . 5
2.2 Memristive switching phenomena and mechanisms . . . 7
2.2.1 History and basic principle of memristors . . . 7
2.2.2 Classification of memristive effects . . . 9
2.3 Self-assembled monolayers . . . 11
2.4 Charge transport through organic thin films . . . 12
2.5 Click-chemistry: azide-alkyne cycloaddition . . . 16
2.6 Kinetic Monte-Carlo method . . . 17

3 Materials 19
3.1 Silicon-on-insulator . . . 19
3.2 Highly doped Si wafer . . . 20
3.3 Silver nanocubes . . . 20
3.4 Spherical Si nanoparticles . . . 21
3.5 Ag-SiO_x-core-shell nanoparticles . . . 22
3.6 Molecular precursors and chemicals . . . 23

4 Fabrication methods 25
4.1 Thin film deposition techniques . . . 25
4.1.1 Atomic layer deposition . . . 25
4.1.2 Sputter-coating . . . 26
4.1.3 Evaporation . . . 26
4.1.4 Self-assembled monolayer growth . . . 27
4.2 Plasma oxidation and cleaning . . . 28
4.3 Reactive-ion etching . . . 28
4.4 Electron-beam lithography . . . 29

4.5 Ion-beam lithography . . . 30
4.6 Nano-imprint lithography . . . 31

5 Characterization methods **35**
5.1 Scanning electron microscopy . . . 35
5.2 Transmission electron microscopy . . . 36
5.3 Atomic Force Microscopy . . . 37
5.4 X-ray photoelectron spectroscopy . . . 39
5.5 Ellipsometry . . . 40
5.6 Current-voltage spectroscopy . . . 41
5.6.1 Conductive-probe AFM . . . 41
5.6.2 Vacuum-probestation . . . 41
5.6.3 Hanging mercury droplet electrode . . . 43

6 Directed assembly of silver nanocube threshold selector arrays **47**
6.1 Introduction . . . 47
6.2 Preparation of AgNC arrays . . . 47
6.2.1 Substrate oxide coating . . . 47
6.2.2 Patterned self-assembled monolayer growth . . . 49
6.2.3 AgNC ligand exchange . . . 50
6.2.4 Site-selective immobilization of AgNCs . . . 51
6.2.5 Planarization of AgNC arrays for CP-AFM measurements . . . 53
6.3 Electrical characterization of AgNC arrays by CP-AFM . . . 53
6.4 Electrical characterization of individual AgNCs by CP-AFM . . . 54
6.5 Kinetic Monte-Carlo simulation of ion migration . . . 58
6.6 Characterization of conductive filaments . . . 63
6.6.1 Structural investigation of conductive filaments by CP-AFM . . . 63
6.6.2 Cross-sectional SEM studies . . . 65
6.6.3 Finite element simulations of the electric field distribution in TiO_2 . . . 66
6.6.4 Comparison with aluminum oxide layers . . . 67
6.6.5 Kinetic Monte-Carlo simulations with electric field distribution . . . 70
6.7 Summary . . . 72

7 Memristive switching in self-assembled AgNC-SiNP dimers **73**
7.1 Introduction . . . 73
7.2 Self-assembly of AgNC-SiNP agglomerates . . . 73
7.3 Electrical characterization of AgNC-SiNP dimers on interdigitated electrodes . 77
7.4 Model for resistance switching . . . 80
7.5 Summary . . . 83

8 Fabrication and directed self-assembly of silicon nanocubes 85
8.1 Introduction . . . 85
8.2 SiNC fabrication by electron-beam lithography . . . 85
8.3 SiNC fabrication by nano-imprint lithography . . . 88
8.4 Electrical characterization of single SiNCs on interdigitated electrodes . . . 91
8.5 Silane-based Cu(I)-catalyzed azide-alkyne cycloaddition on planar substrates . 92
8.5.1 Structural characterization of self-assembled monolayers . . . 93
8.5.2 Electrical characterization of SAMs by Hg droplet electrode . . . 96
8.6 Functionalization and self-assembly of SiNCs . . . 97
8.7 Summary . . . 99

9 Conclusion and Outlook 101

A Resistive switching in single core-shell nanoparticles 105
A.1 Fabrication of core-shell nanoparticle devices . . . 105
A.2 Bipolar and unipolar resistive switching . . . 107
A.3 Stability of bipolar resistive switching . . . 108
A.4 Model for the switching mechanism . . . 109
A.5 Summary . . . 111

B Side-selective coverage of SiNCs by metal evaporation 113

C Self-assembly of 3D germanium-oxide-nanocube colloidal crystals 115

Bibliography 117

List of publications 131

Acknowledgments 133

List of abbreviations

AC	alternating current
AFM	atomic force microscopy
Ag	silver
AgNC	silver nanocube
Al	aluminum
Al_2O_3	aluminum oxide
ALD	atomic layer deposition
APTMS	p-azidophenyltrimethoxysilane
Au	gold
CA	contact angle
CF	conductive filament
CMOS	complementary metal-oxide-semiconductor
CP-AFM	conductice probe atomic force microscopy
CSNP	silver-silicon oxide core-shell nanoparticle
CuAAC	copper-catalyzed azide-alkyne cycloaddition
DC	direct current
DMF	dimethylformamide
EBL	electron-beam lithography
ECM	electrochemical metallization
EDX	energy dispersive X-ray spectroscopy
EtOH	ethanol

FIB	focused-ion beam
H_2O_2	hydogen peroxide
H_2SO_4	sulfuric acid
HF	hydrofluoric acid
HRS	high resistance state
HSQ	hydrogen silsesquioxane
I_{CC}	compliance current
IDE	interdigitated electrode
IV	current-voltage
kMC	kinetic monte-carlo
LRS	low resistance state
MIM	metal-insulator-metal
MPTMS	(3-mercaptopropyl)trimethoxysilane
MTEP	N-[2-(methylthio)ethyl]-3(2-propyn-1-yloxy)
N_2	nitrogen
NIL	nano-imprint lithography
NP	nanoparticle
OT	1-octanethiol
PCM	phase change memory
PTMS	phenyltrimethoxysilane
PVD	physical vapor deposition
PVP	polyvinylpyrrolidone
QCM	quartz-crystal microbalance
ReRAM	resistive random acces memory
RF	radio frequency
RIE	reactive-ion etching

SAM	self-assembled monolayer
SEM	scanning electron microscopy
Si	silicon
SiNC	silicon nanocube
SiNP	silicon nanoparticle
SiO_2	silicon dioxide
SMU	source meter unit
SOI	silicon-on-insulator
T	temperature
TEM	transmission electron microscopy
Ti	titanium
TiO_2	titanium dioxide
TPS	trichloro(1H,1H,2H,2H-perfluorooctyl)silane
TS	threshold switch
VCM	valence change memory
XPS	X-ray photoelectron spectroscopy

1 Introduction

In fast growing semiconductor industry, the limit of down-scaling has nearly been reached in the past years. In particular, Moore's law, which predicts that the packing density of devices in integrated circuits roughly doubles every one and a half years is no longer valid [1]. For device dimensions in the range of 7 nm, which is the technology node of most recent device architectures, conventional top-down lithography technology reaches its limitations and non-classical physical effects play a more and more important role. In fact, conventional immersion optics need to be replaced by extreme-UV steppers and problems arising from quantum mechanical effects such as leakage currents due to tunneling at the gate need to be considered. Hence, on the one hand, the trend goes towards multi-core architectures, where each core is specifically designed for a certain task and optical interconnects between cores should be implemented to increase communication speed between cores in future configurations. Such core architectures and tasks could be, e.g., conventional transistor cores to perform logical operations, non-volatile flash memory for data storage and artificial neuronal networks in 3D cross-point geometry for pattern recognition and machine- or deep learning.
In addition, the integration of novel material systems beyond Si and new device architectures are under intense investigation also to further boost device performance concerning power consumption, which is a big issue as battery technology lags behind power consumption of new displays and processors in cell phones and laptops. New materials include III-V and II-VI semiconductors for novel tunnel field effect transistors (TFET) or lasers, 2D materials such as graphene, functional polymers for flexible electronics and also metallic, semiconductor and oxide nanoparticles (NPs). Chemical synthesis of NPs is of particular interest, as it allows for reliable fabrication of NPs in large yields (milligrams) and in very small sizes down to a few nm. Novel strategies towards expansion of electronic circuitry into the third dimension to further enhance packing density and interconnectivity include wafer bonding and cross-point architectures. However, these concepts are restricted concerning down-scaling options and complexity of systems, as they are all based on top-down fabrication approaches.
Hence, there has been a tremendous increase of interest in next generation bottom-up fabrication approaches such as self-assembly of functional building blocks. Such building blocks could be used for novel neuromorphic computation schemes, with major applications envisaged in pattern recognition, navigation and machine learning [2–4]. Large progress has been made to emulate or realize synapse function with new device types such as memristive junctions, in particular those showing gradual or multi-level, hysteretic resistance changes depending on the

excitation history [5, 6]. Besides, memristive systems are also promising candidates for future nonvolatile memory applications and neuromorphic computation, owing to their excellent scalability, low power consumption and fast operation rates [7–11]. In particular, compared to conventional FET-based memory, no gate potential needs to applied to retain a certain state in non-volatile memristors, yielding the advantage of less power consumption during operation. While promising arrangements of interconnected artificial neurons have already been demonstrated, the degree of interconnectivity still remains small compared to the human brain [12]. In this context, an extension of the electronic circuitry, beyond common cross-point geometries, into the third dimension appears to be the first, indispensable approach [13, 14]. To construct a scalable, interconnected network of memristive junctions, a controlled bottom-up self-assembly process of NPs is a potentially viable approach. Large-scale 2D and 3D colloidal assemblies of NPs have been demonstrated [15–17], and also memristive function has been shown for various assemblies of NPs, even including neuromorphic function [18–26]. However, in these studies, mainly layers of NPs have been addressed with large top contacts, decisively limiting down-scaling options and control over device performance. Therefore, single NPs or single NP-colloids need to be assembled and contacted in a directed manner for future integration. Such a 3D functional composite made from memristive 'neuromorphic' NPs would require the controlled combination of heterogeneous materials –a basic requirement common to all memristive junction architectures: depending on switching mechanism, two either active or passive electrodes from conductive material, together with an insulating solid electrolyte in-between them are required [9, 10]. In this regard, a first important step would be the controlled, bottom-up self-assembly of heterogeneous nanoparticle aggregates, and the demonstration of their reliable, tailored memristive function. In addition, towards self-organized neuromorphic systems, such functional building blocks would also need to find their place on chip on their own without the need of a physical template. In this work, these points are addressed in a step wise manner.

The structure of this thesis is as follows:

- In **chapter 2**, a brief introduction on the theory of memristive devices is given. In addition, the theoretical background of self-assembly of colloidal crystals and the growth of self-assembled monolayers of molecules is described as well as on charge transport through such monolayers. Moreover, a theoretical description of the 'click'-reaction used for self-assembly of NPs and the physical model of kinetic Monte-Carlo (kMC) simulations for simulation of metal ion migration dynamics in oxide layers is given.

- **Chapter 3** gives an overview over all materials and chemicals used to fabricate functional nanoparticle composites, whereas

- in **chapters 4** and **5**, all the methods used to fabricate and characterize these systems on the nano-scale are described.

- **Chapter 6** covers the results on fabrication and electrical characterization of silver-nanocube threshold selector arrays via directed self-assembly and conductive-probe atomic force microscopy. Additional detailed ex-situ studies of these devices after electrical operation as well as kMC simulations are additionally performed to investigate the origin and mechanisms behind threshold switching behavior.
- **Chapter 7** subsequently describes the directed self-assembly and electrical characterization of binary Ag-nanocube/Si-nanoparticle colloids, which showed non-volatile bipolar memristive switching.
- In **chapter 8**, the fabrication of Si-nanocubes (SiNCs) by nano-imprint lithography and reactive-ion etching and the subsequent surface functionalization and directed self-assembly of SiNC-aggregates in suspension is described.
- At the end, **chapter 9** summarizes the results obtained in this work and gives an outlook on possible future experiments.

2 Theoretical background

The following chapter gives a theoretical introduction on the self-assembly of colloidal crystals and the growth of self-assembled monolayers, the working principle of memristive switching devices, the most important charge transport mechanisms through self-assembled monolayers, the chemical azide-alkyne cycloaddtion reaction and the model of kinetic Monte-Carlo simulations.

2.1 Nanoparticles and colloidal self-assembly

For the directed self-assembly of nanoparticles (NPs), various approaches and techniques have been developed over the past decades [27–29]. In a colloidal self-assembly process, particles of different shapes and sizes can be assembled into higher order superlattices, so-called colloidal crystals. The final shape of these crystals is not only pre-defined by the structure and surface-morphology of each individual building block (or particle) participating in the self-assembly process, but also by other factors such as temperature or polarity of solvents. These crystals can have one-dimensional (1D), two-dimensional (2D) and three-dimensional (3D) structure and can be devided into mono, binary and polynary colloidal crystals depending on their composition [15]. In the following, a basic overview over colloidal crystals and their most commonly used assembly strategies will by given.

One-dimensional chains of nanoparticles, also referred to as 1D colloidal crystals, are chains of NPs ordered in lines either in solution or on a surface. In Fig. 2.1 (a) (I) and (III), binary chains of spherical and cubic NPs are shown, whereas the dimer in (a II) is also referred to as a 1D system. Chains of NPs can be formed by various techniques, including a modified type of Langmuir-Blodgett process, where a monolayer of NPs on the surface of a liquid is transferred into grooves in a surface of a substrate by capillary forces [30]. Other techniques reported are sintering of a precursor or sonication of tiopronin-stabilized Ag-nanospheres in DI water [31, 32]. Dimers and chains of cubic NPs can be achieved by rendering one or two sides of nanocubes (NCs) to be hydrophobic, as shown in Fig. 2.1 (a) (II) and (III), respectively. By executing the self-assembly process in a polar solvent, NCs tend to minimize their surface-free energy yielding directed agglomerate formation [17]. Another approach is the directed assembly of NPs via complementary DNA, enabling directed aggregate formation in solution and on surface [33, 34]. Similar procedures can be used to form two-dimensional colloidal crystals consisting of monolayers of nanoparticles with different geometries, as shown in Fig. 2.1 (b)

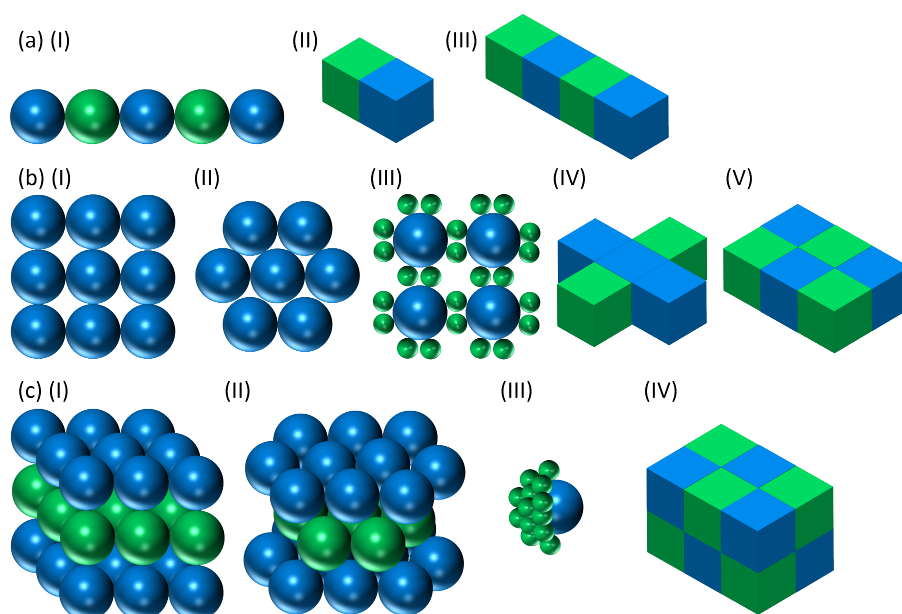

Figure 2.1 Schematic representation of a selection of different (a) one-dimensional, (b) two-dimensional and (c) three-dimensional colloidal crystals consisting of spherical or cubic building blocks such as nanoparticles. Following different self-assembly approaches with spherical nanoparticles, which may or may not have equal sizes, mono- (only blue color) and binary (blue and green color) systems can be targeted, exhibiting different packing modes. In addition, selective functionalization of side facets of nanocubes allows for directed self-assembly of dimers (a II), chains (a III), 2D aggregates of different shapes (a IV and V) and 3D assemblies (c IV).

(I) to (V). By transferring NP layers on a liquid either onto a smooth, hydrophilic surface of a substrate or into pre-defined holes with a certain pitch and diameter on a substrate, by block co-polymer techniques, or by de-wetting of precursors, two-dimensional monolayers of NPs can be realized with different packing densities and inter-particle spacings [35–39]. By tuning the amount of functionalized NC facets, two-dimensional structures shown in Fig. 2.1 (b) (IV) and (V) can be obtained. To obtain NC sheets, four adjacing sides of NCs are rendered hydrophobic, whereas 'cross-like' systems are obtained with a mixture of NCs featuring one or four hydrophobic surfaces in polar solvents [17]. In addition, ordered NP structures on surface can be formed by site-selective immobilization of NPs onto pre-defined self-assembled monolayers (SAMs) exhibiting terminal groups enabling covalent chemical bond formation to NPs. Popular methods include immobilization of AuNPs onto thiolated SAMs [40], via 'click' reaction (cf. section 2.5, [26, 41, 42]) or by using complementary DNA strands [33]. Three-dimensional colloidal crystals such as shown in Fig. 2.1 (c) (I) to (IV) can be fabricated using layer-by-layer growth modes, via surface functionalization enabling covalent chemical bond formation during self-assembly and by making use of hydrophobic and electrostatic interactions in solution [43, 44]. This way, complex aggregates such as core-shell structures (cf. Fig. 2.1 (c IV) [45]) and even macroscopic crystals in the millimeter range can be fabricated [46].

In general, self-assembly processes can be classified into static and dynamic processes, where

static self-assembly commonly corresponds to irreversible superlattice or agglomerate formation. However, using dynamic approaches such as dissipative self-assembly of NPs enables time-dependent agglomerate formation, for, i.e., self-healing compounds or transient functional materials for drug delivery. This can be achieved using a driving force which is consumed over time, such as a fuel, controlling the interaction strength between NPs [47].

2.2 Memristive switching phenomena and mechanisms

In the following, the history, theoretical background and most important types of memristive switching devices are described to provide a broad but focused overview. This section closely relates to [48].

2.2.1 History and basic principle of memristors

The existence of a fourth fundamental passive circuit element in addition to the resistor, the capacitor and the inductor was first proposed by Leon Chua et al. in 1971 [49]. From symmetry arguments, he concluded that there should be a fourth fundamental element connecting the quantities charge and flux as

$$d\Phi = M dq \tag{2.1}$$

with Φ being the magnetic flux, M the so-called memristance and q the electric charge. In the most simple case of linear elements, where M is a constant, M is equal to the resistance. However, if M is a variable of the charge itself, the memristor is a more complex nonlinear circuit element. The most simple mathematical definition of a current-driven memristive system can be written in the differential form as

$$v = R(\omega)i \tag{2.2}$$

$$\frac{d\omega}{dt} = i \tag{2.3}$$

with v the differential voltage, i the differential current, ω the state variable and R a generalized resistance which depends on the internal state of the device. In the most simple case, ω is simply the charge. An experimental realization of a functional memristive device has been missing until 2008, when Strukov et al. proposed a simple structure as a voltage-driven memristive device [50]. As can be seen in Fig. 2.2 (a), such a device consists of a top electrode (blue color) and a bottom electrode (green color) crossing each other, comprising a solid electrolyte in-between at the cross-point (orange color). In their work, they used chemically inert Pt electrodes on the top and bottom of the crossbar and TiO_2 as intermediate layer (or also referred to as solid electrolyte). When a voltage bias is applied to one of the electrodes, a conductive filament (CF) starts to grow in the oxide. As long as this filament is not complete, the device is in the initial high resistance state (HRS), as depicted by the blue line in the IV-curve in Fig.

2.2 (b). However, as soon as the filament is complete, it electrically bridges the two electrodes and the device is set, featuring a transition from the HRS to the low resistance state (LRS, red line). Usually, a compliance current I_{CC} is set in order to prevent the device from irreversible hard breakdown as indicated by the black dashed line. Subsequently, the information can be erased, i.e. the device can be reset applying a certain voltage of opposite polarity as shown by the dashed red arrow. This type of hysteresis-like IV-characteristic shown in Fig. 2.2 (b) is also referred to as bipolar memristive switching. By contrast, when the device is reset applying a voltage of same polarity, as indicated in Fig. 2.2 (c), the system features unipolar memristive switching behavior. During RESET operation, the CF is removed and the electrical contact between the top and bottom electrodes disconnected resulting in a change to large resistance [7, 51–53].

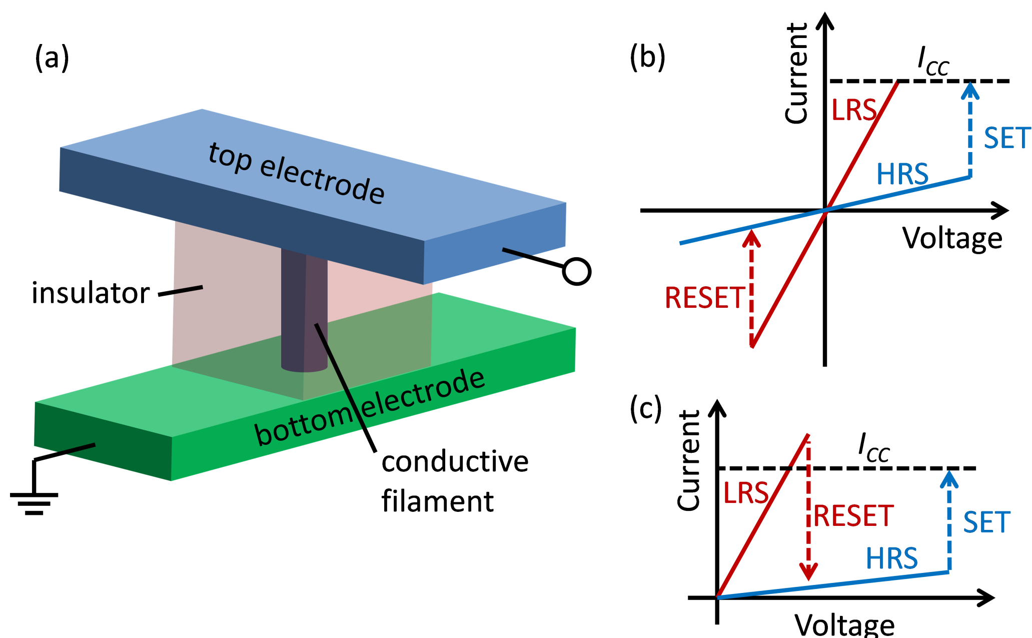

Figure 2.2 (a) Schematic of a basic crossbar memristive device, being composed of a top electrode (blue), an insulating intermediate layer (orange) and a bottom electrode (green). When a voltage is applied to the top electrode, a conductive filament grows and bridges the two electrodes. Filament formation results in a change in resistance of the device from a high resistance state (HRS) to a low resistance state (LRS) as depicted by the blue IV-curve in (b), corresponding to the SET operation. Filament rupture, corresponding to the RESET process is achieved by applying a voltage of opposite polarity such as shown in red color in (b) (bipolar memristive switching), or of same voltage polarity, such as depicted in (c) (unipolar memristive switching). Adapted from Pan et al. [9].

2.2.2 Classification of memristive effects

Electrochemical metallization memory

One of the most important realizations of a resistive random access memory (ReRAM) device is the Electrochemical Metallization Memory (ECM), which is a type of conductive bridge memory (CBM). It usually consists of

- a chemically inert metal bottom electrode, also called passive electrode (PE), which can be Pt, W or highly doped Si for example,
- an insulating material as intermediate layer, also referred to as solid electrolyte, which can consist of a variety of amorphous or poly-crystalline materials including TiO_2, SiO_2, Al_2O_3, Ta_2O_5, WO_3, ZrO_2, GeO_x, a-Si, etc. [7, 51–55],
- and a chemically active top electrode, also being referred to as active electrode (AE) consisting of a metal which can be oxidized and reduced under external electric potentials. Ag and Cu are the most commonly used metals for this purpose.

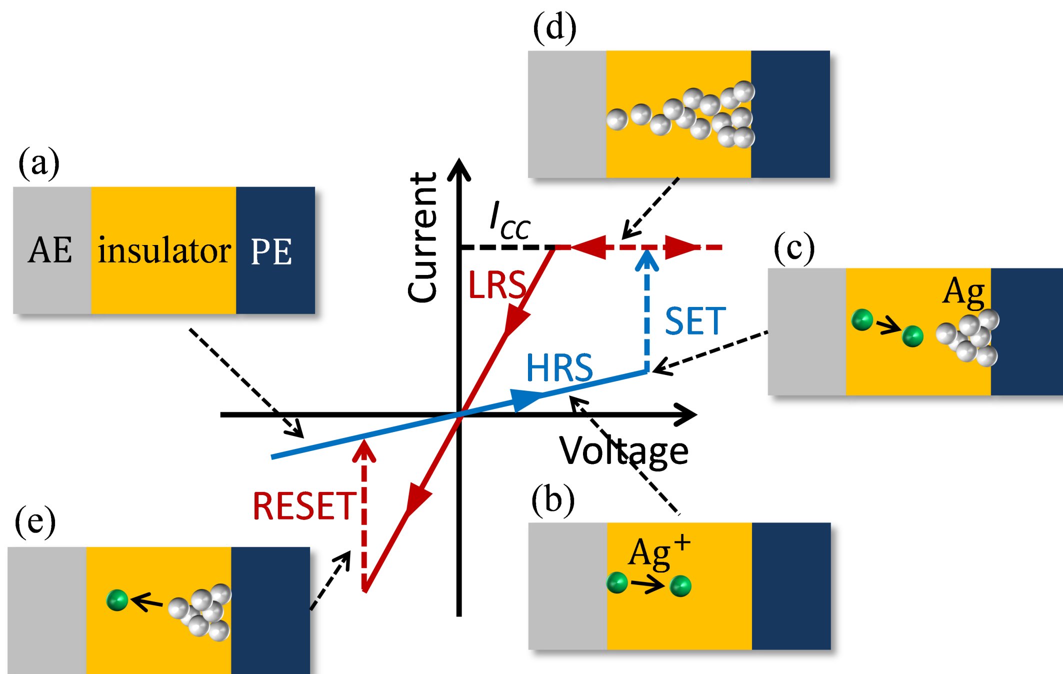

Figure 2.3 Basic principle of electrochemical metallization memory. (a) The active electrode (AE), which consists of Ag in this case, insulator and passive electrode (PA) components of the device before electrical operation are shown in gray, orange and blue color, respectively. (b) and (c) When a positive bias is applied to the AE, Ag-ions (green dots) migrate towards the PE, where they are reduced. Therefore, a conductive filament grows (composed of silver dots) from PE to AE. (d) As soon as the filament bridges both electrodes, current can flow and the device is set. (e) The device is reset applying a voltage of opposite polarity, oxidizing the CF apex and therefore removing the filament. Adapted from Waser et al. [52].

An exemplary IV-sweep of an ECM is schematically described in Fig. 2.3, with (a) illustrating the geometry of the device including the three functional layers mentioned before. In this case, the AE is made of Ag, the electrolyte is some sort of oxide and the PE consists of an inert metallic material. If an external, positive bias is applied to the AE, some Ag atoms are oxidized to Ag^+-ions and start to migrate through the oxide towards the PE along the direction of the electric field (green dots). As soon as they get into contact with the PE, they are reduced again and therefore immobilized. Hence, as can be seen in (C) Ag-atoms agglomerate at the PE and a filament starts to grow from CE to AE. Also, Ag-ions preferentially migrate towards the still incomplete CF due to local electric field enhancement. During this SET process, the current is very small and the device is in the HRS (blue line). As soon as the filament reaches the AE, as shown in (d), both electrodes are connected and the current rapidly increases until the pre-set compliance current I_{CC} is reached. Being set, the device is in the LRS (red line). Sweeping back to smaller positive and negative voltages, the device therefore shows Ohmic conductance. However, applying a small negative bias, as depicted in (e), Ag^+-ions flow into the other direction towards the AE again, and therefore the filament is being partly removed opening an insulating gap in the oxide. The event when the filament breaks is therefore called the reset event, with the device switching from LRS to HRS.
As the filament is stable with no external bias being applied, this memory device is non-volatile. However, a drawback of ECMs is on the one hand rather slow ion migration dynamics, therefore limiting the switching speed to a range of microseconds. On the other hand, a forming step is required in ECMs, as the very first application of voltage yields a larger SET voltage being a disadvantage for industrial implementation.

Valence change memory

Another prominent realization of a memristive device is the so-called Valence Change Memory (VCM). In a VCM cell, the resistive switching can be filamentary or area-type switching. It commonly consists of the same layer structure as ECMs, however, in contrast to ECMs, a VCM device does not involve any mobile metal ions. In fact, the insulating layer is commonly sandwiched between two inert electrodes (also referred to as metal/insulator/metal (MIM) structure) and the resistance switching mechanism is solely based on the migration and re-distribution of mobile charges and respective vacancies generated in the oxide material itself. Commonly used materials are $SrTiO_3$, TiO_x, HfO_x TaO_x and WO_x. Multilayer structures containing combinations of these materials or combinations of sub-stoichiometric layers are also possible enabling tuning of switching parameters. A prominent example is a Pt/TiO_2/Pt structure, where O_2^--ions are generated in the binary oxide applying a bias voltage to the system. When these mobile ions are generated, they leave two-times positively charged oxygen vacancies V_O^{++} behind. These vacancies, ordered in the geometry of a filament, can serve as conductive bridge for negative charges, analogue to doped semiconductors. Hence, respective set and reset processes rely on vacancy filament migration in a gap between an incomplete vacancy

filament and the counter electrode. The IV-curve and respective nanoionic mechanisms behind the switching mechanism strongly remind on the characteristics of neurons. Therefore, VCMs are mainly in the focus for possible applications in artificial neuronal networks [51, 53, 56].

Phase change memory

The third and most important candidate for industrial RRAM applications is the Phase Change Memory (PCM) owing to it's fast switching speed of several ns and excellent endurance. Here, a phase change material., i.e., a material which can undergo a phase transition between an insulating amorphous phase and a conductive crystalline phase is sandwiched between two inert electrodes. Suitable materials can be found on the pseudo-binary line between GeTe and Sb_2Te_2. Initially, when a small voltage is applied, the device is in the OFF state. When a certain threshold voltage is reached, Joule heating causes the device to locally heat above its critical transition temperature and a crystalline domain is formed inside the insulating material. Through this crystalline domain, current can flow and the device is set featuring Ohmic conductance also for small voltages. To reset the device, an even higher voltage has to be applied, heating the material above its characteristic glass transition temperature. During this reset process, the crystalline material melts and undergoes a second transition to its amorphous phase again. Hence, in contrast to the previously described bipolar ECM and VCM devices, the IV characteristics of the PCM is unipolar with the set and reset processes occurring at the same voltage polarity (cf. 2.2 (c)) [51, 57].

2.3 Self-assembled monolayers

In general, the term self-assembly describes the spontaneous formation of ordered superstructures from pre-defined building blocks undergoing an energy minimization process. Self-assembled monolayers (SAMs) of molecules on solid substrates are ordered assemblies of surfactants exhibiting headgroups that have the ability to adsorb to a surface [58–62]. SAMs commonly consist of amphiphilic molecules that feature hydrophilic headgroups (blue circles) and hydrophobic endgroups (yellow rectangles), as shown in Fig. 2.4 [61, 63]. Usually, also a spacer moiety is located in-between head- and endgroup, which is also called backbone. It critically influences the stiffness and length l of molecules, which is crucial to obtain good SAM quality. Frequently used headgroups are thiols, silanes and phosphonic acids, as they can bind covalently to noble-metals or hydroxyl-terminated oxides, respectively. However, there are various other techniques to achieve chemical binding of molecules to solid interfaces, such as hydrosilylation [64, 65]. Spacers can consist of any non-polar backbone such as alkanes, whereas endgroups can also deliver certain chemical functions such as for rendering surface potential or for immobilization and label-free detection of organic material [66]. During the formation of SAMs on solid substrates, the headgroup physically adsorbs, whereas backbone and endgroup point away from the liquid-solid interface, making the molecule stand upright

under a certain tilt angle Θ_t. This tilt-angle depends on the maximum packing density of molecules in the SAM and is measured with respect to the surface normal, as depicted in Fig. 2.4. It can be determined by measuring d experimentally and simulating the molecule length l. This way, Θ_t can be calculated via

$$\Theta_t = \arccos\left(\frac{d}{l}\right). \tag{2.4}$$

SAM quality on planar substrates is determined by evaluating characteristic parameters such as thickness, roughness and surface potential. SAM thickness is measured comparing values obtained by AFM nanolithography scratching (cf. sec 5.3) and ellipsometry (cf. sec 5.5), whereas water contact angle measurements are used to determine SAM endgroup polarity. In addition, pin-holes or multilayers are visualized by tapping-mode AFM (cf. sec 5.3).

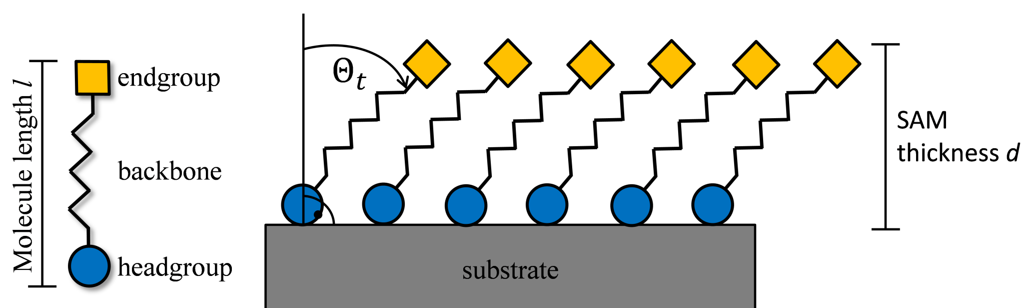

Figure 2.4 Schematic structure of a self-assembled monolayer of molecules. The substrate can be any solid-state material such as a novel metal, an oxide or a semiconductor. The blue circles indicate the headgroups of the molecules, which bind to the substrate. They are separated by the backbones (black lines) from the endgroups (yellow rectangles). The ordered molecules exhibit a certain tilt-angle Θ_t, which is measured with respect to the surface normal.

2.4 Charge transport through organic thin films

Since the early seventies, when Mann and Kuhn measured the electrical properties of an organic monolayer for the first time, the field of molecular electronics was rapidly growing [67]. The main reason for vast interest in implementing electrical function to single or ensembles of organic molecules is the ultimate lateral down-scaling option for data storage and computation. However, making reliable solid-state contacts to soft organic monolayers or even to single molecules is very challenging, as most standard semiconductor processes fail. This is why mostly ensembles of molecules on surfaces, so-called self-assembled monolayers, or single molecules at low temperatures have been studied using special contact formation schemes on the nano-scale which have been developed over the last four decades [68, 69]. These techniques mainly rely on using soft metals or sharp conductive probes. The most popular contact formation techniques are:

- Scanning tunneling microscopy (STM) [70–73]. In STM, a very sharp conductive tip (only a few atoms at the tip apex) is raster-scanned across the sample with a distance of a few nm and the tunneling current is recorded enabling atomic resolution;

- Conductive-probe atomic force microscopy (CP-AFM, cf. section 5.3) [74];

- Break junction method [75, 76], where typically a thin gold strip line on a flexible glass slide is functionalized by molecules of interest. For IV-measurements, the glass slide with the gold is slowly bend by application of a force from below the glass by a piezo actuator until the Au breaks at a pre-defined position. This way a small gap of a few nm in the Au line is formed, which is bridged by a single or only a few molecules;

- Hanging mercury droplet electrode (cf. section 5.6.3) [77–80];

- Eutectic gallium indium electrode (EGaIn) [81, 82], whose working principle is very similar to hanging Hg droplet electrode. However, the top contact is formed by EGaIn, featuring the advantage of not implicitly needing inert atmosphere in the setup. Also, SAMs on metallic substrates can be measured as the EGaIn does not attack metals (in most configurations);

- Cross-wire method [83], where typically two conductive nanowires are surface-functionalized by molecules of interest. Subsequently, these two wires are crossed with each other forming a nano-junction and separately electrically contacted;

- Nanogap electrodes [84, 85], where electrical charge transport is measured through SAMs or organic layers in horizontal direction in a small gap. These gaps may consist of metal contacts on an insulator, or highly doped Si on SOI fabricated by top-down or bottom-up fabrication techniques;

- Nanotransfer printing and 'µ-contact printing' [86], where flexible stamps are used to either deposit SAMs on a conductive surface or to print metal contacts onto SAMs, respectively;

- Metal nanoparticles method [87–89], where metallic nanoparticles are functionalized and immobilized in nanogaps;

- Nanopore method [90], where nanopores are used to immobilize molecules. The pore commonly separates two reservoirs featuring different ionic concentrations, such that molecules flow from one side of the pore to the other while simultaneously measuring the current between reservoirs. This way, when a molecule is immobilized in a pore, it partly blocks the current. When the inside of the pore is functionalized, such blocking event is selective and characteristic.

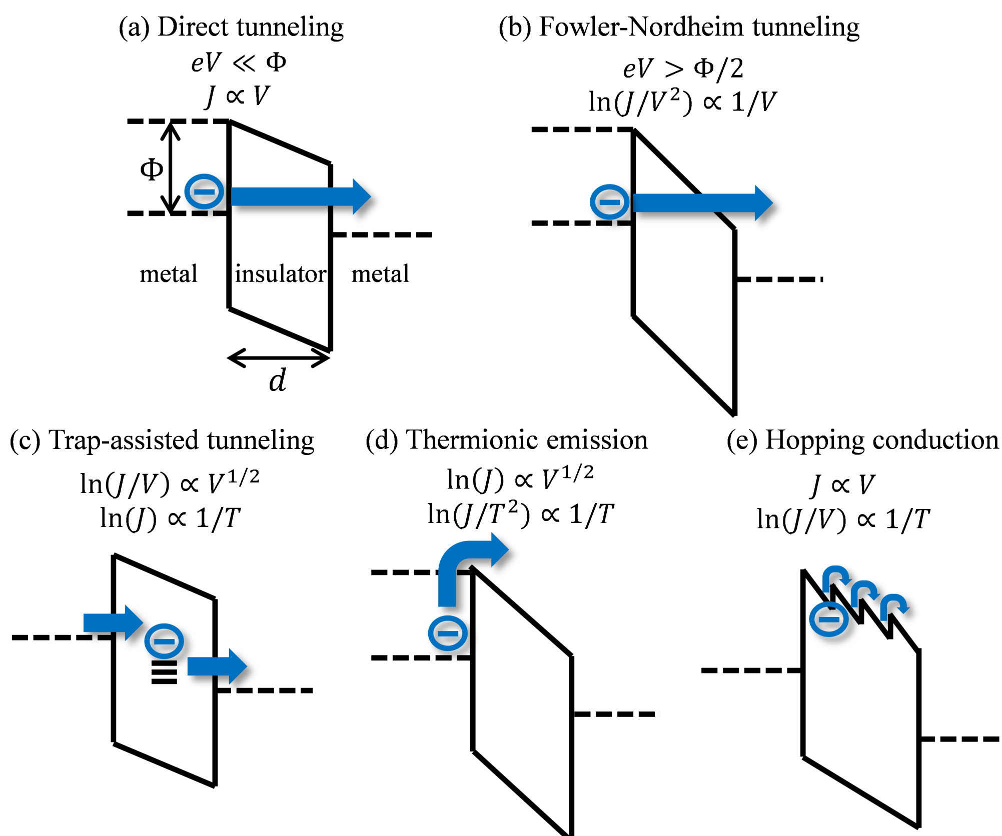

Figure 2.5 Schematic representation of most important charge transport mechanisms through organic thin films. (a) Direct tunneling and (b) Fowler-Nordheim tunneling are based on quantum mechanical tunneling mechanisms and therefore mainly dependent on the barrier height Φ, whereas (c) trap-assisted tunneling, (d) thermionic emission and (e) hopping conduction are kinetic effects and therefore also dependent on temperature. Adopted from Aswal et al. [68].

For more detailed information on different contact schemes, please refer to the indicated references. In the following, the basic principles of theoretical models for charge transport through ensembles or few molecules will be described. These general physical models can also partly by used to explain charge transport through similar nano-systems such as thin oxide layers or ensembles of nanoparticles. In the most simple case, a SAM of aliphatic chains is sandwiched between two metal electrodes, yielding a so-called metal-insulator-metal (MIM) structure [80]. In such system, the most important charge transport mechanisms are (a) direct tunneling, (b) Fowler-Nordheim tunneling, (c) trap-assisted tunneling or Poole-Frenkel emission, (d) thermionic emission and (e) hopping conduction, as illustrated in Fig. 2.5 [68, 69, 91, 92]. Tunneling is a quantum mechanical concept stating that the probability density of the electron wavefunction has a finite value also on the other side of an energetic barrier of height Φ, with the wavefunction exponentially dropping in the barrier. For a trapezoidal barrier, the

Simmons model is a commonly used approximation linking the direct tunneling current J_{DT} to most relevant quantities [68, 93, 94]:

$$J_{DT} = \frac{e}{2\pi h d^2}\left[\Phi \exp\left(-\frac{4\pi d}{h}\sqrt{2m^*\Phi}\right) + (\Phi + eV)\exp\left(-\frac{4\pi d}{h}\sqrt{2m^*(\Phi + eV)}\right)\right], \quad (2.5)$$

with e the elemental charge, h the Planck constant, Φ the average barrier height, d the barrier width, m^* the electron effective mass in the insulator and V the applied voltage between the two metal electrodes. This general expression can be simplified for different voltage regimes. For small voltages of $eV << \Phi$, it has been shown that eqn. 2.5 can be simplified to

$$J = J_0 \cdot \exp(-\beta d), \quad (2.6)$$

with

$$\beta = 2\sqrt{\frac{2m^*\Phi}{\hbar^2}} \quad (2.7)$$

being the tunneling decay coefficient, an important figure of merit characterizing the decay of tunnel current through thin films such as SAMs and J_0 a constant depending on the barrier width d. In the near-equilibrium regime close to $V \approx 0$, Φ can be considered to be independent of V, and therefore $J \propto V$. For intermediate voltages, i.e. $eV < \Phi/2$, the current density can be considered to be approximately proportional to $J \propto V + V^3$. However, for large voltages, i.e. $eV > \Phi$, the potential barrier is modeled to exhibit triangular shape, as shown in Fig. 2.5 (b) and Fowler-Nordheim tunneling occurs. In this high voltage regime, the current density J_{FN} can be expressed as

$$J_{FN} = AE^2 \exp\left(-\frac{B}{E}\right), \quad (2.8)$$

with $A = e^3/16\pi^2\hbar m^*\Phi$, $B = (4\sqrt{2m^*}/3e\hbar)\Phi^{3/2}$ and $E = V/d$ the electric field across the insulator. Hence, if charge transport is governed by Fowler-Nordheim like transport, plotting $\ln(J_{FN}/E^2)$ against $1/E$, also known as Fowler-Nordheim plot, should result in a linear correlation. By fitting, m^* and Φ can be extracted assuming A and B to be known quantities. In experimental configurations, non-ideal systems have to be considered exhibiting structural defects. In SAMs, such defects might be surface reconstruction sites at the interface between molecules and substrate or other structural imperfections such as impurity atoms forming localized trap states in the energy gap, illustrated as small horizontal bars in Fig. 2.5 (c). In such systems, charge transport not only occurs via direct tunneling, but also via trap-assisted tunneling, where charges are trapped at localized trap states in the tunnel barrier. These trapped charges can be thermally excited (Poole-Frenkel emission) and removed by an external electric field. At elevated temperatures and large fields, a portion of electrons statistically has enough energy to directly overcome the energy barrier via thermionic emission as illustrated in Fig. 2.5 (d). By contrast, if the insulator exhibits large extended defects, charges can jump from defect to defect and hopping transport dominates, as shown in Fig. 2.5 (e).

2.5 Click-chemistry: azide-alkyne cycloaddition

In general, 'click'-reactions are assigned to a class of highly efficient, fast, simple and selective chemical reactions only requiring moderate reaction conditions featuring large chemical yields with only small amount of by-products [95–98]. These reactions allow for the formation of a vast variety of compounds not requiring complicated reaction schemes or purification procedures and are highly reliable and reproducible, making click chemistry very popular in organic and inorganic chemistry. The most common and powerful click reaction reported to date is the Cu(I)-catalyzed version of the 1,3-dipolar cycloaddition of alkynes and azides yielding 1,2,3-triazoles, which is a special type Huisgen cycloaddition [99]. In general, alkynes and azides do not readily react with one another, such that cycloaddition requires an additional driving force such as heat or strain [100]. Fig. 2.6 shows the basic reaction scheme of the Huisgen 1,3-dipolar cycloaddition with azide (I) and alkyne and (II) as educts and two different triazole isomer products (III) and (IV) (1,4- and 1,5-regioisomers). During the reaction, the dipole of the azide group attacks the carbon triple bond of the alkyne, which is a dipolarophile, re-distributing charges to form 1,2,3-triazole. For this to happen, a driving force Δ is needed to weaken the alkyne triple bond. Depending on how bulky functional groups R^1 and R^2 are, a 1,4- or 1,5-regioisomer is favored. In detail, if functional groups are bulky, the cycloaddition reaction yields more 1,4-regioisomers (type (III)), as due to steric interactions, bulky functional groups tend to be more separated from each other, making them distribute at positions 1 and 4 in the triazole ring. Hence, the reaction of azides and alkynes without a catalyst yields mixtures of 1,4- and 1,5-regioisomer products. However, introducing Cu(I)-ions as catalyst, the reaction speed is drastically increased by a

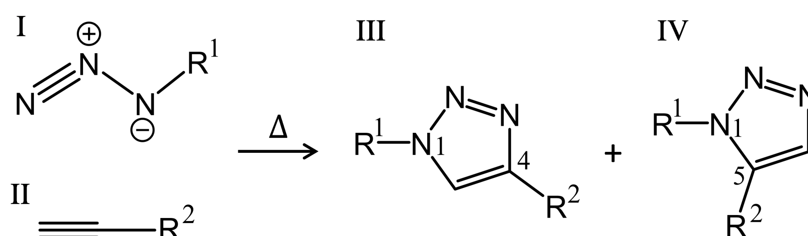

Figure 2.6 Thermal dipolar 1,3-cycloaddition reaction. Under the application of a thermal potential Δ, no regioselectivity is obtained with (I) azides and (II) alkynes forming (III) 1,4- and (IV) 1,5-regioisomer 1,2,3-triazole product due to steric interactions. Adopted from [96].

factor of $\sim 10^7$ making the application of a driving force unnecessary and regioselectivity is achieved [101]. In fact, Cu(I) catalysis exclusively yields 1,4-regioisomer product and it is mostly not sensitive to the type of interacting functional groups, making it the ideal click reaction. This is due to a different cycloaddition mechanism, in which the Cu-ions weaken carbon triple bonds of alkynes. These advantages are utilized in the cycloaddition reaction performed on planar Si/SiO_2 substrates and for the self-assembly of nanoparticles in this work, as described in chapters 6 and 8. Fig. 2.7 schematically illustrates the respective Cu(I)-catalyzed cycloaddition on surface, where the functional groups are trimethoxysilanes to form organic

self-assembled monolayers (SAMs, cf. sections 2.3 and 4.1.4) featuring different terminal groups in a step-wise manner. At first, SAMs of trimethoxysilanes with amine terminal groups are reacted with NHS-ester to obtain SAMs with alkyne terminal groups. Subsequent click-reaction with azido-silanes finally yields 1,2,3-triazole (1,4-regioisomer) linkers connecting both silane terminal groups (denoted as CuAAC as abbreviation for Cu-catalyzed azide-alkyne cycloaddition).

CuAAC reactions can be performed in a variety of solvents, pH values and tolerate a broad range of temperatures. Popular sources for Cu(I) are copper salts such as Cu(I)-iodide and Cu(II)-sulfate in combination with solvents and ligands stabilizing the oxidation state in solution. For this purpose, Cu(II)-sulfate with ascorbic acid in DMF or Cu(I)-iodide in water can be used [102].

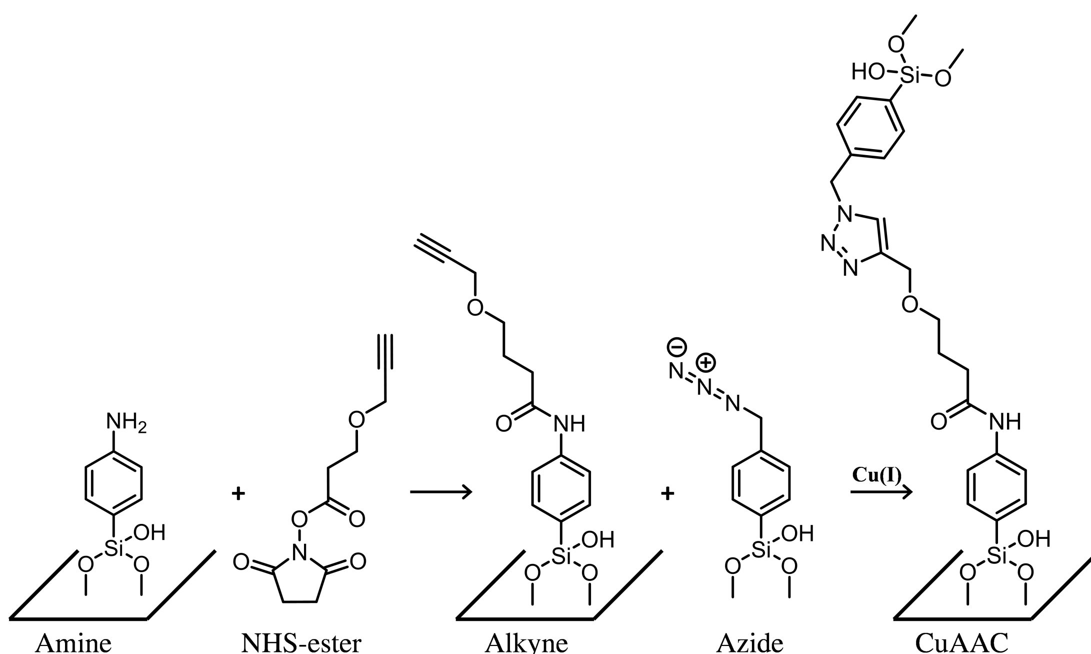

Figure 2.7 Schematic representation of silane based Cu(I)-catalyzed azide-alkyne cycloaddition (CuAAC) on planar substrates. Self-assembled monolayers of trimethoxysilane surfactants featuring different terminal groups and thickness are formed in a step-wise manner. At first, amino-SAMs are reacted with NHS-ester to yield alkyne terminal groups. Subsequent regioselective CuAAC reaction with azido-silanes results in the formation of a 1,2,3-triazole bond connecting both silane moieties.

2.6 Kinetic Monte-Carlo method

Monte Carlo methods are a class of stochastic algorithms used to simulate complex physical systems, often with many coupled degrees of freedom, on the basis of repeated random sampling. Hence, the origin of the name stems from the casino in Monte Carlo. The kinetic Monte-Carlo (kMC) model is a special type of Monte Carlo method, which describes the dynamic time

evolution of a system undergoing transitions $T_{i,j}$ from an initial state i to final states j, as schematically illustrated in Fig. 2.8 [103]. This is why the kMC model is a versatile and established method to simulate the dynamics of particles or charges within nano-structured systems such as diffusion of electrons in electron-beam resists or the movement of charges generated in organic photoconductors [104]. The respective transition rates $\nu_{i,j}$ correspond to the probability of pathways chosen between states in the system and are known inputs to the simulation. Stochastic algorithms are used to correctly propagate the system from state to state. In a typical kMC simulation, the order of tasks executed is as follows:

- At first, an initial state at $t = 0$ is chosen, which can be usually defined by macroscopic, measurable quantities such as an energetic state of a particle.
- Next, all possible transitions are identified and corresponding rates and the total number of rates calculated.
- Subsequently, two uniform random numbers are generated from a uniform distribution in a unit interval to choose a certain step and transition.
- After the transition was carried out, all transitions are recalculated and if necessary, transitions are removed or new ones added to the system.
- In the end, the simulation time is updated by adding the according time step. If the system is now in its global final state, the simulation is over. If not, new transition rates are calculated and the next steps described above executed again.

This way, the time-evolution of complex systems can be simulated with a small amount of input, as only the initial state and transition rates are known quantities in the algorithm. In this work, a kMC framework developed by the group of Prof. A. Gagliardi (simulation of nanosystems for energy conversion, department of electrical and computer engineering, TUM) was used to simulate the movement of Ag^+-ions in TiO_2 and Al_2O_3 layers, as described in more detail in sec. 6.5.

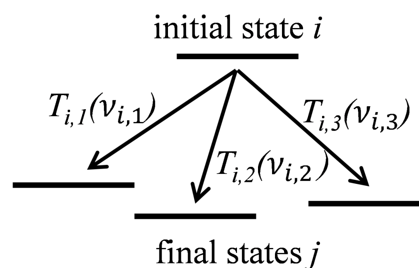

Figure 2.8 Schematic illustration of the kinetic Monte Carlo method. The system undergoes possible transitions $T_{i,j}$ from an initial state i to final states j with the probability of known transition rates $\nu_{i,j}$. The choice of transition is generated from random numbers.

3 Materials

In the following, materials used in this work will be specified, including various types of wafers, nanoparticles and chemicals.

3.1 Silicon-on-insulator

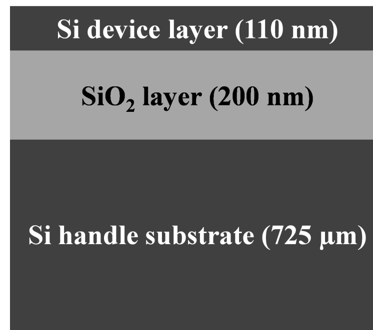

Figure 3.1 Structure of the silicon-on-insulator (SOI) wafer used for the fabrication of Si nanocubes, consisting of a highly doped top Si device layer of 110 nm thickness, a buried Si oxide layer of 200 nm thickness and a 725 µm thick Si handle substrate.

The silicon-on-insulator wafers (SOI) used for the preparation of silicon nanocubes (SiNCs) were purchased from *Soitec, France* (Unibond^{TM} wafers, 200 mm) and consist of a top Si device layer (110 nm, a thermally grown buried Si oxide (SiO_2) layer ((200 ± 5) nm thickness) and a bottom Si handle wafer (725 µm, as depicted in Fig. 3.1. The device layer was highly implanted and annealed at *Fraunhofer EMFT* by either boron (target doping concentration ∼ $5 \times 10^{19}\,\text{cm}^{-3}$) or phosphorous atoms (target doping concentration ∼ $5 \times 10^{17}\,\text{cm}^{-3}$) to yield p- or n-type conductivity. After annealing, wafers were diced into pieces of 8 mm × 8 mm or 12 mm × 12 mm for further processing. Conductivities of n- and p-type top Si layers were evaluated by four-point probe measurements on mesa structures. These mesa structures were etched into the Si layer by negative-tone electron-beam lithography (EBL) and reactive ion etching and contacted by optical lithography and Ti/ Au evaporation and lift-off.

Measuring two samples of each kind resulted in values of conductivity ρ listed in table 3.1. These values of ρ translate into impurity concentration of $N_D = 3 \times 10^{19}\,\text{cm}^{-3}$ and $N_A = 9 \times 10^{19}\,\text{cm}^{-3}$ of donors and acceptors, respectively. The other specifications listed in table 3.1 are provided from *Soitec*.

layer	thickness	crystal orientation	measured resistivity $\rho\,(\Omega\,\text{cm})$	
			n-type	p-type
Si device layer	(110.0 ± 7.5) nm	⟨100⟩	4.3±0.16	2.8±0.08
Si substrate	725 µm	⟨100⟩		8 to 22

Table 3.1 Characteristic parameters of the Si layers of SOI wafers. Values of resistivity of the Si top layer were evaluated by four-point-probe measurements.

3.2 Highly doped Si wafer

Highly doped Si wafers (4 inch, p-type boron, ⟨100⟩, $\rho < 0.005\,\Omega\,\text{cm}$, (525 ± 25) µm thickness, single-side polished) covered by a thermally grown, dry silicon dioxide (SiO_2) layer of thickness 50 nm were purchased from *Active Business Company GmbH, Germany*. These wafers were diced into pieces of 8 mm × 8 mm or 12 mm × 12 mm and used as substrates for interdigitated electrodes (IDEs).
Single-side polished, highly p-type (Boron, $\rho < 0.005\,\Omega\,\text{cm}$) wafers with a thickness of (350 ± 25) µm were also purchased from *Active Business Company GmbH, Germany* and were mainly used for scanning electron microscopy (SEM) studies of NP self-assembly processes. Additionally, these wafers were also covered by titanium dioxide (TiO_2) or aluminum oxide (Al_2O_3) for on-chip self-assembly experiments as described in chapter 6.
The respective surface roughness of both types of wafers was measured by tapping-mode atomic force microscopy (AFM) and was < 0.5 nm.

3.3 Silver nanocubes

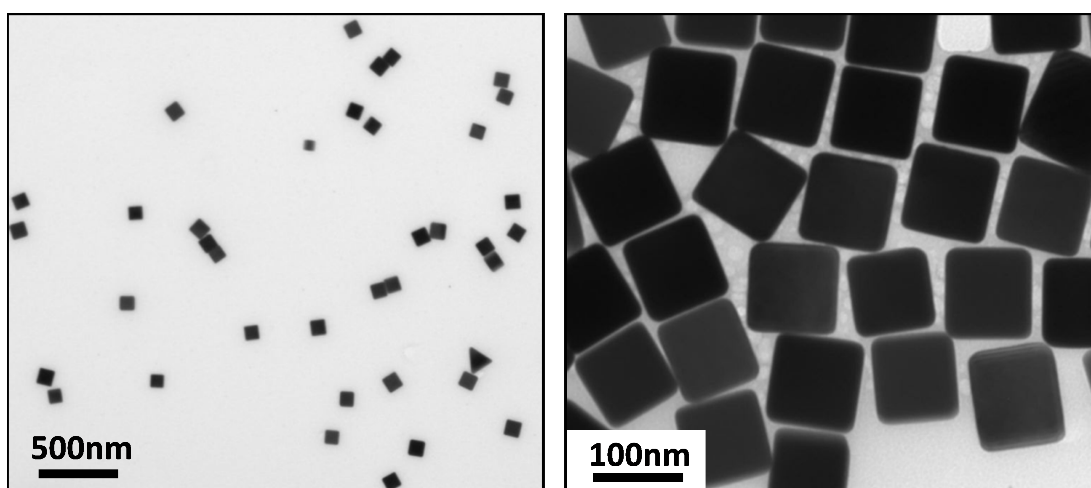

Figure 3.2 Transmission electron microscopy images of AgNCs revealing narrow size distribution and excellent NP quality with sharp edges (reprinted with permission from *nanoComposix, Inc*).

Silver nanocubes (AgNCs) with edge length (98.5 ± 7.0) nm were purchased from *nanoComposix, Inc, USA* (100 nm PVP NanoXact^{TM} Silver Nanocubes). Typical transmission electron microscope (TEM) images with different magnifications are shown in Fig. 3.2 (reprinted with permission from *nanoComposix, Inc*), revealing narrow size distribution and excellent NP quality. These NPs are dispersed in ethanol (EtOH) with a mass concentration of 1.00 mg/mL, which relates to a particle concentration of 9.9×10^{10} particles/mL and are surface-functionalized by a dense layer of polyvinylpyrrolidone (PVP) molecules to prevent agglomeration. AgNCs are used as building blocks for the directed assembly of NP-threshold selector arrays, as described in chapter 7.

3.4 Spherical Si nanoparticles

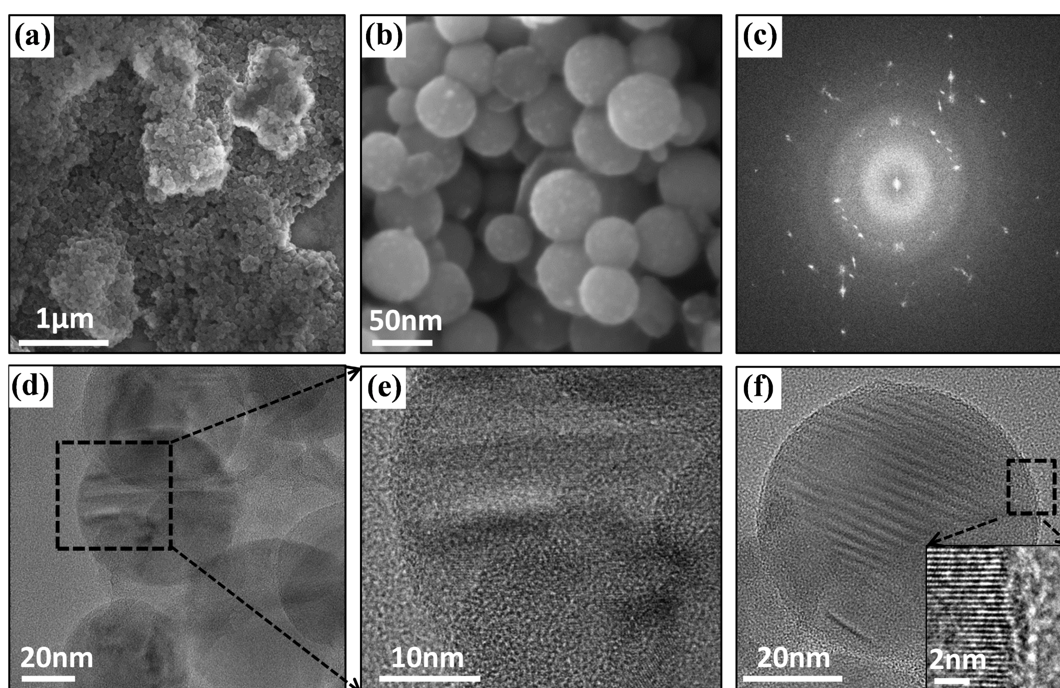

Figure 3.3 (a) and (b) scanning electron microscopy images of alkyl-functionalized SiNPs revealing spherical shape and variation in NP sizes. (c) Diffraction pattern of a typical SiNP obtained with transmission electron microscopy (TEM) showing unordered crystal structure. (d) High-resolution-TEM (HR-TEM) image of a few SiNPs and (e) zoom-in image of one of them, revealing differently sized grains and crystal orientations indicative for poly-crystalline SiNP microstructure. (f) HR-TEM image of an as-synthesized SiNP showing it‘s poly-crystalline structure and a very thin oxide outer layer in the close-up view in the inset.

Spherical Silicon nanoparticles (SiNPs) of size (58 ± 11) nm were fabricated by Dr. M. Jakob at the department of chemistry at TUM as described else-where [64, 105]. Typical scanning electron microscopy (SEM) and transmission electron microscopy (TEM) images of SiNPs obtained with different magnifications can be seen in Fig. 3.3. The TEM images were obtained

from Dr. M. Döblinger at the department of chemistry at Ludwig-Maximilians-University in Munich. SEM images in Fig. 3.3 (a) and (b) reveal spherical NP shape and decent variation in size. The diffraction pattern in Fig. 3.3 (c) and HR-TEM images in Fig. 3.3 (d) and (e) reveal poly-crystalline SiNP micro structure featuring un-ordered crystal orientations. A zoom-in TEM image at the position of SiNP side in Fig. 3.3 (f) indicates very small oxide layer in a range < 2 nm, hence in the range of native Si oxide.
Briefly, for SiNP fabrication, an amount of 2 g hydrogen silsesquioxane (HSQ) was sintered in an oven at 1500 °C (ramp rate 8 °C/min) for 1 h in a gas mixture of 95% Ar : 5% H_2. Then, the temperature was ramped down to 1300 °C with the same ramp rate and the sintering oven switched off. Subsequently, 200 mg of the composite was grinded and ball-milled, before HF –etching for 1 h (3 mL HF and 3 mL EtOH) under constant stirring. Particles were then extracted with toluene by centrifugation and decantation, before re-dispersion in dry toluene in a schlenk flask (3-times freeze pump thaw). As a last step, SiNPs were dodecyl-functionalized by hydrosilylation in a schlenk line and stored in dry toluene.

3.5 Ag-SiO_x-core-shell nanoparticles

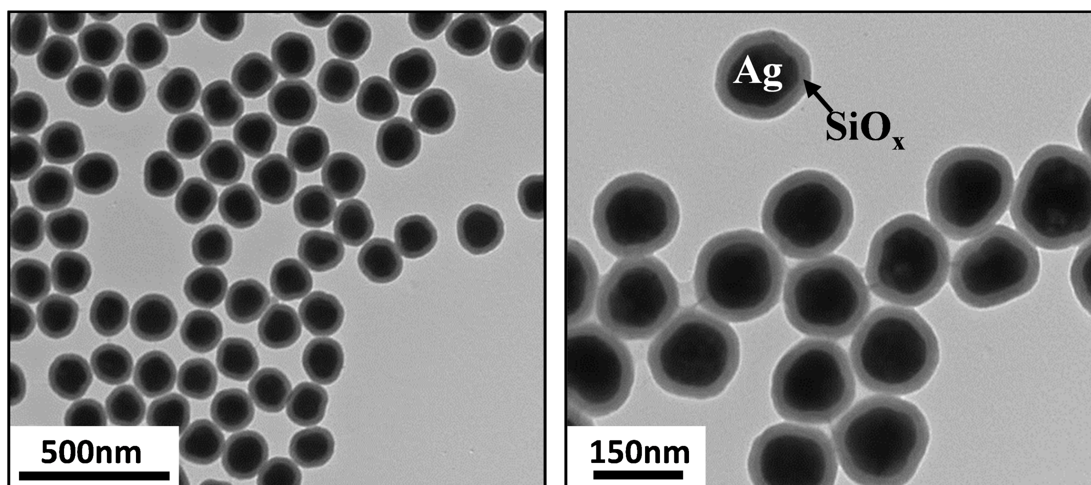

Figure 3.4 Transmission electron microscopy images of CSNPs. The core-shell structure can be clearly identified, with the Ag-core in the middle and the SiO_x-shell covering the NP (reprinted with permission from *nanoComposix, Inc*).

Silver-Si-oxide-core-shell nanoparticles (CSNP) are also purchased from *nanoComposix, Inc, USA* (Silica Shelled 100 nm NanoXact^{TM} Silver). These CSNPs consist of a (107 ± 11) nm-sized Ag core and a 22 nm thick SiO_x shell, relating to an overall NP diameter of (151 ± 11) nm. The NP shell is an amorphous network of silicon and oxygen and was added to the previously synthesized Ag particle surface via the base catalyzed condensation of silanes such as tetraethylorthosilicate in a Stöber growth based procedure. Typical TEM images of CSNPs with different magnifications are shown in Fig. 3.4 (reprinted with permission from *nanoComposix, Inc*), ex-

hibiting slight imperfections of spherical geometry, but homogeneous coverage of the Ag-core by SiO_x. The as-purchased particles are dispersed in ethanol and have a mass concentration of 1.10 mg/mL, which relates to a particle concentration of 1.7×10^{11} particles/mL. For single-particle measurements, the as-obtained suspension was diluted down to a concentration of 15 ng/mL (2.4×10^6 particles/mL).

3.6 Molecular precursors and chemicals

For surface functionalization and self-assembly of nanoparticles, nano-imprint lithography, wet etching and substrate cleaning, various chemicals, surface active molecules and precursors were used. In table 3.2, the most important chemical compounds including their suppliers and specifications are listed.

chemical compound	supplier	CAS number
p-azidophenyltrimethoxysilane	Gelest, Inc.	83315-74-6
Aminophenyltrimethoxysilane	Gelest, Inc.	33976-43-1
Propagyl-N-hydroxysuccinimidyl ester	Sigma-Aldrich Co.	1174157-65-3
Copper(I) iodide	Sigma-Aldrich Co.	7681-65-4
Cysteamine	Sigma-Aldrich Co.	60-23-1
1-octanethiol	Sigma-Aldrich Co.	111-88-6
(3-mercaptopropyl)trimethoxysilane	Sigma-Aldrich Co.	4420-74-0
Trichloro(1H,1H,2H,2H-perfluorooctyl)silane	Sigma-Aldrich Co.	78560-45-9
Acetone	Chemsolute	67-64-1
Isopropanol	Chemsolute	67-63-0
Ethanol	VWR Chemicals	64-17-5
N,N-dimethylformamide	Sigma-Aldrich Co.	68-12-2
Pyridine	Sigma-Aldrich Co.	110-86-1
Sulfuric acid	VWR Chemicals	7664-93-9
Hydrogen peroxide	Merck KGaA	7722-84-1

Table 3.2 Table of chemicals used in this work including respective suppliers and CAS numbers (Chemical Abstracts Service).

4 Fabrication methods

In this chapter, the most important fabrication methods will be described. For thin film deposition, atomic layer deposition (ALD), physical vapor deposition (PVD) techniques such as sputter-coating and evaporation and the growth of self-assembled monolyers (SAMs) of surface-active molecules were used. In addition, for layer modification and pattern formation, plasma oxidation, reactive-ion etching (RIE), electron-beam lithography (EBL), focused ion-beam milling (FIB) and nano-imprint lithography (NIL) procedures were optimized and employed for various applications.

4.1 Thin film deposition techniques

4.1.1 Atomic layer deposition

Atomic layer deposition (ALD) is a widely used technique for the growth of thin films of various kinds of dielectrics, metals and semiconductors with a highly defined thickness with precision on the atomic scale [106, 107]. ALD provides ultimate control over layer thickness, as only one atomic layer at a time is grown in a step-wise manner. In detail, in a typical pulsed reaction scheme, chemical bonds are formed between the gaseous precursor molecules in the growth chamber of type A and the substrate. As soon as there are no more reaction sites available for these molecules on the surface, the growth of this first layer A stops. Hence, the monolayer growth is self-terminating and not dependent on deposition time. Once the surface is completely covered with molecules of type A, the next layer can be grown. For this purpose, after cleaning the substrate from physically adsorbed molecules of type A by purging with inert gas such as nitrogen, a precursor of type B is provided, which can chemically bind to type A. This way, multilayers can be grown in a pulsed layer-by-layer growth mode. As the layer thickness is not dependent on deposition time, ALD is especially advantageous when very rough surfaces have to be overgrown. For example, samples featuring deep holes or high steps can be homogeneously covered with a constant, highly defined thickness by providing a sufficient amount of reaction time. This procedure would not work with more basic thin film deposition techniques, such as physical vapor deposition (PVD), as this would lead to isotropic coverage from one direction. However, ALD is not suitable for layer thicknesses exceeding several 10 nm, as the growth rate is rather slow, i.e., in the range of several nm/min.

4.1.2 Sputter-coating

Sputter-coating is a special type of PVD technique and is mainly used for the deposition of dielectrics and metals [108]. During a typical sputtering process, a high direct current (DC) voltage is applied between a target material (cathode) and the substrate (anode). In the evacuated chamber, usually a gas-mixture of argon (Ar) and nitrogen (N_2) is supplied ('bleeding gas'), yielding a typical chamber pressure of $\sim 1 \times 10^{-2}$ mbar. This gas mixture forms a plasma under the application of an external electric field. Ar-ions (Ar^+) from this glow discharge plasma are accelerated towards the negatively biased target. Once a ion hits the target, it ejects an atom. This target material atom is transported towards the substrate and deposited on the surface. Some of the deposited material is also desorbed again, hence, by carefully tuning of DC voltage and chamber pressure, the desired deposition rate can be adjusted. If dielectrics need to be deposited, an additional radio frequency (RF) voltage is applied to the target. This is not possible for metallic targets due to charging. With an additional RF field, higher deposition rates are possible, as electrons couple energy more efficiently to the plasma when oscillating in the field. The most commonly used configuration is magneton sputtering, where a magnet behind the target confines electrons making ionization more efficient, also yielding higher deposition rates in the order of 1-10 nm/s. In this work, sputter-coating was executed with a *Quorum Q150T ES* system with deposition rates of ~2 nm/min.

4.1.3 Evaporation

In an evaporation process, which is another type of PVD process, metals such as gold (Au), titanium (Ti), platinum (Pt) or aluminum (Al) are either heated by a heat coil (thermal evaporation) or locally by an highly energetic electron beam (electron-beam evaporation) in a ceramic crucible [108]. High-vacuum conditions of $\sim 1 \times 10^{-8}$ mbar to 1×10^{-7} mbar in the evaporation chamber are necessary to facilitate metal ion evaporation from the metal source to the substrate, which are placed face-to-face to each other. To maintain good vacuum conditions, sample transfer is commonly executed via a load-lock, which also decreases sample loading times and out-gases samples prior to loading into the main chamber to minimize contamination. In addition, a double-walled cryogenic vacuum main chamber, which is supplied with liquid N_2 is used to freeze out air moisture. The low melting point of metals in high-vacuum allows metal ions to be evaporated. As the mean free path of metal ions is larger then the distance between source and substrate, ions are transported without collision with other impurity atoms inside the chamber. Hence, the material takes a line-of-sight route from source to substrate, resulting in isotropic layer growth. Typical growth rates using evaporation are in the order of 0.05 to 0.2 nm/s and can be adjusted by controlling the temperature of the metal source (i.e., the acceleration voltage of the electron beam heating the source). The growth rate can be monitored by the change of resonance frequency of a quartz-crystal microbalance (QCM) crystal, which is placed in close proximity to the substrate. In this work, evaporation of metal layers was

executed with a *Leybold L560* system and typical growth rates of Ti and Au were adjusted to be 0.05 nm/s and 0.2 nm/s, respectively.

4.1.4 Self-assembled monolayer growth

There exist various techniques for the preparation of organic monolayers such as described in 2.3. The most important ones are [58–61, 68]:

- Langmuir films at liquid-gas interfaces,
- Langmuir-Blodgett films, where a Langmuir film is transferred onto a solid substrate, for example by the ”tethering by aggregation and growth”-process (T-BAG) [109],
- self-assembled monolayers grown from solution by dip-coating, and
- organic monolayers grown from the vapor phase.

In this work, SAMs of silanes on Si wafers (cf. sec. 3.2 and sec. 2.5) were fabricated by dip-coating. These SAMs then served for reference experiments on click-reactions used for SiNC self-assembly (cf. sec. 8.5) as described in [102]. For this purpose, prior to functionalization, Si samples coated with native oxide were cleaned by acetone and isopropanol (sonication for 10 min each), piranha solution (H_2SO_4 to H_2O_2 2:1, 15 min at 150 °C on a hotplate) and O_2-plasma to achieve hydroxyl-activation. Subsequently, samples were placed into a solution containing aminophenyltrimethoxysilane molecules (3 mM, 0.1% DI-H_2O in toluene, cf. sec. 3.6) for 24 h, allowing surfactants to graft onto the native Si oxide. Afterwards, samples were sonicated in toluene and methanol to remove multilayers. To achieve alkyne-termination, SAMs were further reacted with propargyl-N-hydroxysuccinimidyl ester (3 mM, toluene, 24 h). Final cycloaddition reaction of alkyne-SAMs was performed exposing samples to p-azidophenyltrimethoxysilane (3 mM) together with catalyst solution for >24 h (5 ml DMF, 8.8 mg sodium L-ascorbate, 6.2 mg copper(II) sulfate pentahydrate). Finally, samples were again sonicated in toluene and methanol to remove multilayers.
Square-shaped pattern of SAMs on p-Si/TiO_2 were fabricated by adsorption of silanes from the gas phase into pre-defined square-shaped holes fabricated by EBL, as described in more detail in sec. 6.2.2 [40, 41, 110]. In brief, the EBL-patterned TiO_2-sample was placed in a vacuumed desiccator next to a droplet of p-azidophenyltrimethoxysilane molecules (APTMS, cf. sec. 3.6) for 30 min. The vacuum allows APTMS molecules to distribute in the desiccator and to adsorb onto the hydroxyl-activated TiO_2 surface in the EBL-resist holes. Chemical binding of APTMS molecules and removal of multilayers is achieved by subsequent heating on a hotplate for 15 min at 130 °C. The EBL-resist pattern was removed by sonication in acetone for 15 min and the SAM-pattern characterized by tapping-mode AFM.
Functionalization and ligand exchange of nanoparticles (NPs) such as silver nanocubes (Ag-NCs) and Si-nanoparticles (SiNPs) was realized by dispersing NPs in a respective mixture of

molecular precursor and a suitable solvent. The solvent was chosen with respect to NP stability and precursor solubility (cf. sec. 7.2). During ligand exchange, NP suspensions were sonicated and placed on a vortexer for agitation. After functionalization, solvent exchange and cleaning of NPs was done by repeated centrifugation, separation of solvent and precipitate by pipetting and re-dispersion of the precipitate by sonication.
Most important parameters during SAM growth in solution are temperature, polarity of the solvent, molecular concentration and surface free energy of the substrate, which critically influence surface coverage and tilt-angle of the SAM and therefore SAM quality. For example, choosing a too large molecular concentration above the critical micelle concentration potentially results in unintentional molecule agglomeration and multilayer formation. In addition, cross-linking of molecules can happen, when either the head- or endgroups chemically interact.

4.2 Plasma oxidation and cleaning

For oxidation of thin Ti layers up to a thickness of 20 nm, a strong oxygen plasma in a barrel ashier (*Alpha Plasma*) is used (600 W, 30 min, 1.4 mbar). For cleaning of samples from organic contamination prior to functionalization or spin-coating of resist for lithography, samples were treated for a shorter amount of time and less power (400 W, 10 min). Oxygen plasma renders the sample surface hydrophilic, being favorable for adhesion of EBL resist and molecule adsorption for the formation of SAMs. The mechanism of oxygen plasma formation in the barrel ashier relies on the same principles as described in chapter 4.1.2.

4.3 Reactive-ion etching

For pattern transfer into solid-state materials, a commonly used technique is reactive-ion etching (RIE) [108, 111, 112]. RIE is a dry chemical etch technique based on plasma of reactive gases and is widely spread in industry and research, owing to a broad range of materials and dimensions accessible for anisotropic etching. In this work, an inductively coupled plasma reactive ion etching machine (ICP-RIE) of type *Plasma Lab 80 Plus* from *Oxford Instruments* was used to transfer the pattern generated by NIL or EBL, which consisted of an array of square-shaped pillars, into the device layer of SOI wafers (cf. sec. 3.1 and chapt. 8). Prior to sample processing, the reaction chamber was cleaned by a strong oxygen plasma for 10 min and the recipe tested without samples. Subsequently, SOI samples were placed on a temperature-controlled sample stage in an evacuated reaction chamber, exhibiting a typical pressure below $2\text{x}10^{-5}$ mbar. Once this base-pressure is reached, reactive gases SF_6 and C_4F_8 are provided. A plasma from these gases is then generated by an inductively coupled radio frequency (RF) source, a coil, which is wrapped around the reaction chamber. As ions in the plasma are heavier than electrons, electrons move faster causing additional collision and therefore additional formation of ionized atoms. Hence, more electrons compared to ions are

neutralized at grounded side-walls of the chamber, leaving more ions compared to electrons in the plasma. Hence, the plasma density is controlled via ICP coupling. During the ICP-RIE process, positively charged ions both chemically and physically react with the sample surface. Reactive ions chemically react and form volatile compounds such as SiF_4. These volatile compounds either desorb directly or are removed physically via bombardment of ions in the plasma, which are accelerated by the capacitive coupled plasma source (CCP), also referred to as "forward power". Hence, this forward power introduces directionality in the etching process, additional to the speed of chemical reactions being dependent on sample crystal orientation. Careful adjustment of parameters is necessary to ensure anisotropy of the etching process and to prevent material deposition instead of material decomposition.
An optimized RIE recipe was chosen (*Si-Etch Opt. 4.1*) for anisotropic etching of cubic Si nano-structures meeting two major requirements:

- high selectivity of etch rates, and
- anisotropic etching until the end of the process.

On the one hand, high selectivity between resist mask and Si device layer has to be ensured, as both layers have approximately the same thickness (~100 nm). A slow etch rate of resist compared to the etch rate of Si ensures complete pattern transfer in vertical direction. In addition, high selectivity between buried oxide layer of the SOI wafer and Si device layer prevents over-etching, as the etching practically stops at the Si/SiO_2 interface. The parameters of this process were chosen as follows: temperature: 25 °C, set pressure: 15 mTorr, RF generator: 15 W, ICP: 220 W, He backing: 10 Torr, gas fluxes of C_4F_8: 30 sccm and SF_6: 20 sccm. As etch rates of Si strongly depend on doping concentration and crystal orientation, calibration experiments prior to sample fabrication are always necessary.

4.4 Electron-beam lithography

Electron-beam lithography (EBL) is a commonly used technique for substrate patterning on the sub-100 nm scale and is mainly used for research purposes [108, 113]. In a typical EBL process, electrons are generated by applying a high electric field to a field emission source (also referred to as electron gun), which is usually a sharp tip consisting of W or LaB_6. Main advantages of field emission sources are well defined electron energy and large brightness. The generated electrons are than extracted and accelerated by applying an acceleration voltage and focused onto the sample surface via an electron-optical system (also called electron column). An electron colum includes components for beam focusing, apertures, a beam blank and a deflection system controlling beam position on the sample. By careful calibration, electron-beam spot sizes in a range of 5 nm can be achieved. The field emission voltage controls the electron-density in the beam. High electron-densities have the advantage of small exposure times making the EBL process faster. However, the disadvantage is, that electrons repel each other in the beam due to

Coulomb-interaction, causing undesired broadening of the beam. Large acceleration voltages are commonly favorable to gain resolution, as Monte Carlo simulations show that the amount of back-scattered electrons and therefore proximity effect can be significantly suppressed using large acceleration voltages [114]. For electron-beam exposure, the beam is deflected by the electron colum deflection system inside pre-defined write fields containing the layout of the structure of interest. As beam deflection distance is limited, for exposure of neighboring structures on a chip, the sample stage is moved towards the middle of the next write field. Commonly, for high resolution processes, thin resist are needed, as the electron beam scatters as it hits the resist, which results in broadening of the exposed area. However, using thin resists can cause problems in subsequent lift-off processes. In addition, drift of the electron beam and therefore failure of the process can occur due to charging of the sample. To circumvent this issue, the backside of Si-substrates and the position of the fixing clamp was always scratched by a diamond scratch to remove native oxide prior to exposure. This enhances electrical contact to the metallic sample stage and therefore allows charge to escape. If substrates are non-conductive, such as transparent silica, special types of conductive resists have to be used.
In this work, for electron-beam exposure, layouts were designed in *Layout Editor* software and transferred as *.gds*-files to the PC of the EBL system (*eLine*, *Raith*). Positive-tone EBL resist *AR-P 6200* was used to fabricate interdigitated electrodes used in chapters 7 and 8. The resist was spin-coated at 4000 rpm for 60 sec and pre-baked on a hotplate at 150 °C for 1 min. This results in a resist thickness of ~80 nm. For exposure, a dose of 80 µC and an acceleration voltage of 30 kV were used prior to development in the developer *AR 600-546* for 1 min. The development process was stopped in isopropanol.
For SiNC fabrication as described in sec. 8.2, SOI samples were coated with negative-tone EBL resist *AR-N 7520.07* via spin-coating (4000 rpm, 1 min). Afterwards, the resist was pre-baked on a hotplate at 85 °C for 5 min and exposed with a dose of 30 µC and an acceleration voltage of 20 kV. Subsequent development of structures was executed in a developer mixture of *AR 300-47* to DI H_2O of 4 to 1 for 110 seconds.

4.5 Ion-beam lithography

Ion-beam lithography, which is also commonly referred to as focused ion-beam milling (FIB), is partially based on the same principle of EBL described before (cf. sec. 4.4). However, in the case of FIB, accelerated ions are used to structure the sample surface either by exposure of a resist or directly by sputtering of material [113, 115]. It is therefore mostly used for the formation of cross-sections for device failure analysis as well as for the fabrication TEM lamella (cf. sec. 5.2). In this work, a Gallium (Ga) gun in a *NVision 40 Dual Beam* setup from *Zeiss* was used for the cross-sectional analysis of nanoparticles as described in chapter 6. In this cross-beam tool, Ga-ions are accelerated towards the sample with an acceleration voltage of 30 kV, while the progress of the milling process was monitored in-situ by the SEM part. During

milling, Ga-ions hit the surface vertically, whereas the sample was tilted by 54° with respect to the electron-beam. Typical ion currents of 50 pA to 10 pA were used for rough and fine milling, respectively. Milling parameters were adjusted in *Elphy Quantum Software*. Prior to ion-exposure, a rectangular area of ~1 µm × 1 µm for milling was defined, as can be seen in Fig. 6.16. For analysis of SEM micrographs of cross-sections, a tilt correction of 36° was applied in *Carl Zeiss Tiff Annotation Editor* software to obtain correct dimensions.

4.6 Nano-imprint lithography

Cubic Si nano-particles were fabricated in large yields using ultra-violet nano-imprint lithography (UV-NIL) on silicon-on-insulator (SOI) wafers, as described in chapter 8 and [116]. In general, NIL is a very versatile high-throughput low-cost technique, which can generate pattern on solid substrates down to sizes of ~ 5 nm [117]. The main advantage compared to other techniques able to produce features on this length-scale such as EBL or X-ray lithography is the possibility of highly parallel generation of structures [118–121]. There are two major variations of NIL: i) thermal NIL, where an imprint resist on a solid substrate is deformed by a mold and subsequently hardened by heat, and ii) UV-NIL, in which the imprint resist is hardened by UV-light through a transparent mold. The work-flow of transparent mold fabrication and imprint process used in this work is schematically illustrated in 4.1 (a) to (d).

Si master stamp fabrication

To produce a pattern which will be used later in the process as original structure for the replication of master-stamps, a Si wafer piece of size 8 mm × 8 mm (grey color) is covered by a negative-tone EBL resist via spin-coating (red color, see Fig. 4.1 (a1)). As shown in Fig. 4.1 (a2), after electron-beam exposure and development (cf. sec. 4.4), the pattern is cleaned by 'piranha' solution (2:1 H_2SO_4:H_2O_2, 15 min, 150 °C on a hotplate) and consists of an array of 4905x4905 square-shaped holes with a size of 110 nm × 110 nm and a distance of 500 nm. Therefore, in total ~24 million holes in an area of 3 mm × 3 mm are located on the Si-mold. As can be seen in Fig. 4.1 (a3), this hole-pattern is than etched into the Si substrate by RIE as described in sec. 4.3. As a last step before replication, an anti-sticking layer (ASL, green color), also referred to as release layer, which consists of a SAM of trichloro(1H,1H,2H,2H-perfluorooctyl)silane (TPS) molecules is deposited onto the Si surface (cf. sec. 2.3). As can be seen in Fig. 4.1 (a4), a TPS-SAM is formed from gas phase by placing a droplet of molecules next to the oxygen-plasma surface-activated Si-mold (200 W, 120 s) in a desiccator for 30 min while continuously pumping. Chemical binding of trichlorosilane headgroups and multilayer removal is achieved by subsequent heating on a hotplate for 15 min at a temperature of 135 °C.

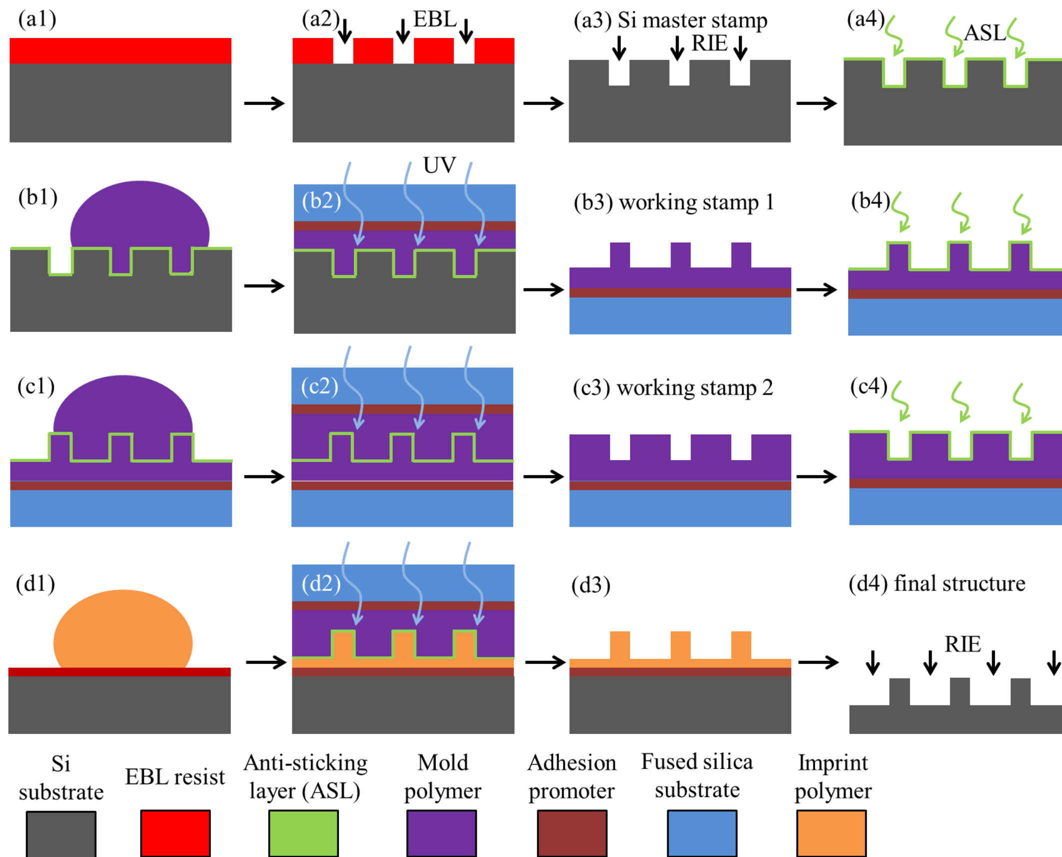

Figure 4.1 Schematic illustration of (a) to (c) stamp fabrication for (d) nano-imprint lithography (NIL). (a1) to (a4) show the steps of Si master stamp fabrication via electron-beam lithography and reactive-ion etching. (b1) to (c4) illustrate pattern replication for the fabrication of transparent working stamps, which are negative and positive replica of the master stamp and consist of UV-curable mold polymer on flexible fused silica substrates. The NIL process is depicted in Figs. (d1) to (d4), where the positive replicate of the master stamp, working stamp 2, is pressed into a UV-curable imprint polymer and hardened by UV irradiation. Subsequent pattern transfer in (d4) is realized by dry etching. The color legend indicates colors of materials used in these processes.

Polymer working stamp fabrication

Working stamps 1, which are the negative replica of the master stamp, are fabricated on round fused silica substrates (blue color) featuring a thickness of 300 µm and a diameter of 31 mm to ensure proper flexibility and transparency to UV-irradiation. These glass substrates act as support substrates for the UV-curable mold polymer (*OrmoStamp, mirco resist technology GmbH*, purple color). For fabrication of working stamps 1, glass substrates are cleaned by sonication in acetone and isopropanol for 15 min each and oxygen plasma (600 W, 2 min). Subsequently, an adhesion promoter (*OrmoPrime08, mirco resist technology GmbH*, dark red color), also referred to as prime layer, which is based on organofunctional silanes, is spin-coated onto the clean silica surface (6000 rpm, 60 s) and heated on a hotplate for 15 min at a temperature of 150 °C. After the sample is cooled down, a small droplet of mold polymer

(~4 µL) is dispensed from a pipette onto the ASL-coated master stamp, as illustrated in Fig. 4.1 (b1). Subsequently, the primer-coated silica surface is put onto the mold polymer without any pressure and the viscid polymer is allowed to distribute all over the structure equally to minimize bubble formation for a few minutes due to capillary forces as shown in Fig. 4.1 (b2). Polymer hardening is realized by irradiation with UV-light from a UV-lamp of a mask-aligner (200 W, 30 s), light blue bowed arrows). Afterwards, as shown in Fig. 4.1 (b3) and (b4), the mold is carefully removed with the help of a scalpel and the surface polymer hard-baked on a hotplate by placing the silica stamp on the cold hotplate and then ramping up the temperature to 130 °C for 30 min. As a last step, before second replication, the surface of working stamps 1 is functionalized again by ASL from vapor phase via the same procedure as described before (Fig. 4.1 (b4)).
Working stamps of type 2, constituting the positive replica of the Si master stamp and used for the actual imprint procedure, are fabricated following the same procedure as described for working stamps 1, as illustrated in Figs. 4.1 (c1) to (c4). However, smaller and thinner fused silica substrates are used featuring a thickness of 150 µm and a diameter of 15 mm being more flexible.

Imprint-lithography

The surface of SOI substrates was structured for subsequent dry etching by NIL procedure described in Fig. 4.1 (d1) to (d4). At first, as can be seen in Fig. 4.1 (d1), the substrate is cleaned (sonication in acetone and isopropanol for 15 min, oxygen plasma 200 W, 5 min) and covered by an adhesion promoter (*mr-APS1*, micro resist technology GmbH) by spin-coating (5000 rpm, 60s) followed by subsequent soft-baking of the primer on a hotplate (150 °C for 5 min). After cool down, the UV imprint polymer (*mr-UVCur21-100nm, micro resist technology GmbH*, orange color) was spin-coated onto the primer (3000 rpm, 60s), resulting in a polymer thickness of ~100 nm. Polymer thickness has to be adjusted according to feature sizes by either dilution with a thinner (*mr-T1070*) or using thicker imprint resists such as *mr-UVCur-200 nm or -300nm*. Subsequently, ASL-coated working stamp 2 was pressed into the polymer in a home-built imprint machine with a pressure of ~5 bar. Pressure was applied for a few minutes for bubble minimization. Afterwards, polymer cross-linking is achieved by UV-irradiation for 3 min by an UV-lamp (365 nm, light blue bowed arrows), as shown in Fig. 4.1 (d2). After careful demolding (see Fig. 4.1 (d3)), pattern transfer was done by RIE as described in sec. 4.3 and illustrated in Fig. 4.1 (d4). Residues of imprint polymer and primer were removed by 'piranha' solution.

5 Characterization methods

In this chapter, most relevant characterization methods will be described. For surface morphology evaluation of nano-structures and thin films, scanning electron microscopy (SEM), transmission electron microscopy (TEM) and atomic force microscopy (AFM) in various modes of operation were employed. Thin film characterization was executed by X-ray photoelectron spectroscopy (XPS) and ellipsometry, whereas electrical characterization of planar samples and nanomaterials was carried out by conductive-probe AFM (CP-AFM), by contacting in a probestation setup and by hanging mercury droplet electrodes.

5.1 Scanning electron microscopy

Similar to EBL, scanning electron microscopy (SEM) also uses a focused electron-beam, which is preferentially extracted from a field emission source [122]. As electrons have a smaller wavelength compared to photons, SEM is suited for imaging structures in a range of a few 100 micrometers down to a few nanometers, a range which is not accessible by optical microscopy. In a typical SEM setup, electrons are produced in an electron gun by application of a typical voltage of 1 kV to 30 kV. The beam is then shaped and focused in a vacuum chamber by a condenser lens, a reflecting coil and an objective onto the sample. These components work electromagnetically, deflecting the electron beam by specially designed magnets. For imaging, the beam is scanned across the sample surface line by line via the deflection coil. Secondary electrons leave the sample and are detected by a detector. Sample topography is visualized in levels of gray on the detector according to secondary electron intensity. When the beam hits the sample, different interactions can occur. The most important ones are:

- generation of secondary electrons,
- elastic backscattering,
- inelastic backscattering, and
- emission of characteristic X-rays.

Hence, depending on the type of sample information desired, different types of detectors are used.

In this work, mainly the in-lens detector in an *NVision 40 Dual Beam* setup from *Zeiss* is used, which is located inside the beam column. It detects low-energy backscattered secondary

electrons, which originate from an interaction volume close to the sample surface. By proper calibration of focus, aperture and stigmatization, this in turn gives rise to a high resolution of ~5 nm, depending on the material type investigated. Generally, the material investigated needs to be at least slightly conductive, such that negative charge deposited by the electron beam can escape from the sample to the motorized stainless steel sample stage, which is grounded. For this purpose, substrates are mounted from the backside by conductive sticky tape made for vacumm conditions. If oxides or organic materials on glass substrates need to be investigated by SEM, coverage of the sample surface by a thin conductive layer of a few nanometers of iridium or carbon by sputter-coating is required. This effectively avoids charging of the sample and therefore drift of the image while raster-scanning.

5.2 Transmission electron microscopy

Physically, the resolution limit of an electron microscope is determined by the de Broglie wavelength of electrons, which is indirectly proportional to the electron energy and therefor the used acceleration voltage. However, in practice the resolution is governed by imperfections of the electron beam column. In an transmission electron microscope (TEM), high acceleration voltages of up to 300 kV are used, and therefore higher resolution is achieved. Similar to SEM, the beam is shaped by condenser lenses before it hits the sample, which has to be transparent for electrons [122]. Therefore, for high resolution images, samples have to be thinner than ~100 nm, depending on the material. After the beam is transmitted through the sample specimen, the transmitted electron beam is shaped and collected by an objective lens and an objective aperture. The objective aperture controls the number of diffracted spots contributing to the final image. Next, electrons pass a sector aperture and lens, controlling the magnification of the image of the diffraction pattern. By controlling the opening of objective and sector apertures, the TEM mode of operation is defined, which can be varied between imaging mode and diffraction mode. Imaging mode provides large magnification and in principle works similar to optical microscopy. Diffraction mode however, which is also referred to as selected area electron diffraction (SAED) in principle shows Bragg reflections of scattered electrons carrying information about sample crystal quality and orientation. High-resolution TEM (HR-TEM) uses large magnification giving rise to resolution below atomic distances.
In high-angle annular dark-field scanning TEM mode (HAADF-STEM) an annular detector is used instead of an objective aperture to detect scattered electrons from an annulus around the main beam in a very high angle. This technique is very sensitive to the atomic number Z of a sample, as incoherently Rutherford scattered electrons are detected, and not the Bragg scattered electrons. For high Z, more electrons are scattered at higher angles due to larger interaction between incident electrons and atomic core. Therefore, high-Z materials appear brighter in the resulting image.
During the course of this work, spherical Si-nanoparticles (cf. sec. 3.4 and chapt. 7) were

transferred on copper grids covered with a thin carbon film. (Scanning-)TEM was performed with a *Titan Themis* (FEI) tool operating at an acceleration voltage of 300 kV, equipped with a *Super-X* detector for energy dispersive X-ray (EDX) spectroscopy. EDX maps were recorded in STEM-HAADF mode with a probe semiconvergence angle of ~21 mrad.

5.3 Atomic Force Microscopy

The technical realization of an atomic force microscope (AFM) was first proposed by Gerd Binnig and co-workers in 1986 following their related work on scanning tunneling microscopy. This achievement was granted with a Noble price the same year [123]. First commercial setups were available in 1989. Since then, a large number of variations emerged finding application in research and industry. AFM is a widely used technique for surface characterization due to it's excellent lateral resolution, comparatively low cost and vast variety of modes of operation and therefore large field of applications [124, 125]. The most important modes of operation are:

- contact mode,
- non-contact mode, and
- intermittent contact mode (also commonly referred to as tapping-mode).

All these modes rely on a laser being reflected from the cantilever surface onto a photodetector, as depicted in Fig. 5.1. The change in tip movement with respect to the sample surface is detected as a change in laser deflection signal at the detector, and this way converted into an electrical signal. In contact mode, the tip is in contact with the sample surface and therefore, the force acting at the tip apex is in the repulsive regime of the Lennard-Jones potential. The lateral tip position with respect to the surface is detected either in constant height (fixed tip-surface separation) or constant force (using the defection feedback system) mode. In ambient conditions, a thin water film always forms at the tip apex due to air moisture, slightly affecting the resolution. By purging the setup with inert gases such as dry N_2, this effect can be minimized. In non-contact mode, the cantilever of the tip is allowed to vibrate near it‘s resonance frequency, which depends on the stiffness of the cantilever. The tip-surface interaction is attractive and monitored by the change of amplitude and phase of the oscillation. The deflection feedback system either detects the resonance frequency or the vibration amplitude of the cantilever and keeps it constant by moving the scanner up or down in response to changes (using the Z-feedback loop). This way, the average tip-sample distance is also kept constant and the Z-feedback signal is used to image the topography.

Tapping-mode AFM is a commonly used technique for surface roughness analysis and relies on the same principle as non-contact mode. However, the tip is allowed to gently touch the surface at the end of each vibration cycle, which enhances the resolution. Another advantage of this technique is, that the tip nearly does not interfere with the surface, making this mode

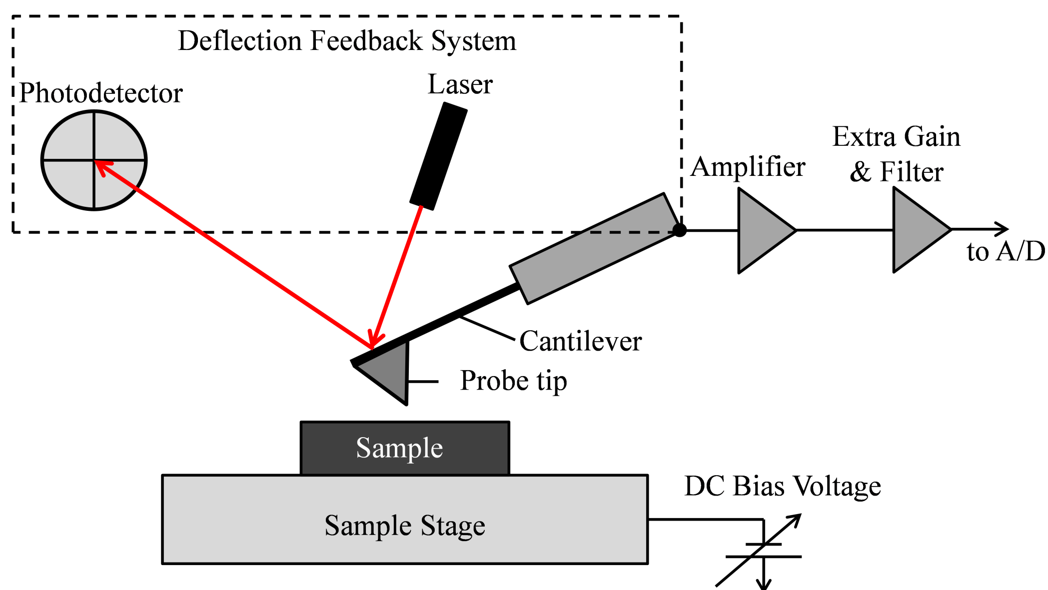

Figure 5.1 Schematic illustration of the (conductive-probe) atomic force microscopy (CP-AFM) setup. For surface characterization, samples are mounted on a motorized stainless steel sample stage on a shock-free table. The tip, consisting of the cantilever and probe tip, is raster-scanned across the surface either in contact- or non-contact mode via a piezo. The resulting deflection of a red laser, which is focused onto the cantilever surface, is detected on a photodetector and translated to an electrical signal. This signal is converted to the topographical information of the sample surface via amplifiers and gain filters. The additional option of applying a DC-bias voltage to the stage via the built-in extended TUNA module (*Tunneling Atomic Force Microscopy*) allows for conductance scans in conductive-probe AFM mode. Surface profiles are processed in *NanoScope Analysis 1.5* software.

non-destructive, also for very soft materials such as SAMs.

In this work, for topographical characterization, samples were mounted on a stainless steel chuck in an AFM setup (*Nanoscope V Controller, Dimension V Controller, Bruker Nano*), as depicted in Fig. 5.1 and fixed by applying a small under-pressure between sample and stage by a vacuum pump. For tapping-mode and contact-mode surface imaging, AFM tips of type *TAP190DLC* ("DLC": diamond-like carbon) from *Budget Sensor* were used. These tips are suitable for a wide range of applications and feature a spring constant of 48 N/m, a resonance frequency of 190 kHz and a tip radius <15 nm. Typical drive frequencies of 0.5 Hz to 1 Hz were used for larger (10 µm × 10 µm) or smaller (1 µm × 1 µm) scan fields, respectively. The resolution was set to a value of 512 points per line. In contact mode, deflection set-points in a range of 0.1 V to 0.5 V were used, depending on the stability of surfaces. In contact mode, a large value of the set-point results in a larger deflection of the cantilever and therefore a larger force being applied to the surface. Hence, for soft materials a small value is favorable. In tapping mode, the set-point was set to a value of 250 mV. In contrast to contact-mode, decreasing the value of the deflection set-point in tapping mode results in a larger tip-to-surface separation, eventually resulting in a slight loss of resolution. For image processing such as flattening, surface roughness determination and depth profiles, *NanoScope Analysis 1.5* software was

used.
For SAM thickness determination, AFM nanolithography scratching was applied [126]. The process can be divided into three steps:

- Tapping-mode: At first, a scan field of 5 µm × 5 µm is raster-scanned in tapping-mode to localize possible contamination and to determine surface roughness of the SAM.
- Contact-mode: If this area is clean and therefore suitable, an area of 1 µm × 1 µm in the middle is scratched in contact mode and the surface beneath exposed. It is crucial to use a proper value of the deflection set-point, as a too large set-point eventually results in the substrate below the SAM also being affected. However, a set-point which is too small potentially results in the SAM being not completely removed. Hence, prior to SAM characterization reference experiments have to be conducted on un-functionalized surfaces to evaluate the maximum set-point which can be applied without damage of the surface. Typically, for oxides such as TiO_2, values up to 0.5 V can be used.
- Tapping-mode: As last step, the previously evaluated scan field of size 5 µm × 5 µm is measured again in tapping-mode and the depth of the exposed area measured.

Despite the above mentioned techniques, a variety of other modes of operation exist, including conductive-probe atomic force microscopy (CP-AFM), which will be described in more detail in sec. 5.6.1, magnetic force microscopy (MFM), lateral force microscopy (LFM), scanning capacitance microscopy (SCM), electric force microscopy (EFM) and Kelvin probe force microscopy (KPFM), to mention the most important ones.

5.4 X-ray photoelectron spectroscopy

In a typical X-ray photoelectron spectroscopy (XPS) experiment, samples are illuminated by a monochromatic X-ray beam impinging on the surface under a small angle of incidence in an ultra-high vacuum chamber [122, 127, 128]. It is a very surface-sensitive technique, as the investigation depth is usually in a range <20 nm. If the energy of X-ray photons is large enough, they will remove characteristic, inner core-shell electrons from atoms of the material investigated. Ejected electrons hitting the detector then posses a kinetic energy W_{kin}, which is the energy they obtained from X-rays (the photon energy W_{ph}) minus the energy required to leave the atom (the binding energy W_b) and the workfunction difference $\Delta\Phi$ between sample and detector:

$$W_{kin} = W_{ph} - W_b - \Delta\Phi \tag{5.1}$$

In standard XPS measurements, typical photon energies of 100-200 eV are used to excite core-electrons. A typical XPS spectrum is obtained at a fixed photon energy by recording the number of photoelectrons as a function of binding energy. As binding energies are different for each chemical element of the material under investigation, the spectrum consists of a series of

distinct lines. These lines represent a sequence of characteristic core levels. However, chemical shifts of these core-levels occur when elements are present in different binding configurations. Thus, XPS provides precise information about chemical oxidation state of elements, as photoelectrons emitted from higher positive oxidation state exhibit higher binding energy due to increased Coulomb interaction with the ion core upon withdrawal of valence charge due to chemical bonding [129].

In this work, XPS spectral analysis of TiO_2 layers was performed by Domenikos Chryssikos at the Walter-Schottky-Institute at TUM using a home-built setup equipped with a non-monochromized *XR 50* X-ray source and a *Phoibos 100* hemispherical analyzer under a pressure of 6×10^{-9} mbar, a voltage of 12.5 kV and an emission current of 20.0 mA. Survey spectra were acquired at an energy step size of 1 eV and a dwell time of 0.5 s using a single scan. For single-peak spectra, the values were 0.1 eV, 1 s and two to four scans were carried out, respectively. A pass energy of 30 eV was used universally.

5.5 Ellipsometry

Ellipsometry is used for thickness determination of thin films such as oxide layers or SAMs on solid substrates [130]. It is a non-destructive and fast method based on the change of polarization of linearly polarized light being reflected from a surface featuring one or more interfaces of thin films. Being reflected, the light gets elliptically polarized, constituting the origin of the name. Enabling determination of refractive index and thicknesses in a range of some micrometers down to a few angstroms makes it a powerful tool also for industrial applications. During a typical measurement, a linearly polarized laser beam of a particular wavelength featuring certain components of s- and p-polarized light r_s and r_p is reflected at an interface. Hence, it's amplitude $\tan(\psi)$ and net phase difference between s- and p-polarized light Δ are changing according to the complex reflectance ratio ρ:

$$\rho = \left|\frac{r_p}{r_s}\right| \exp(i\Delta) = \tan(\psi) \cdot \exp(i\Delta). \tag{5.2}$$

The change in polarization generally depends on the angle of incidence, wavelength, dielectric constant and thicknesses of the thin film. Modeling of measured parameters with Fresnel and Fabry-Perot equations allows for layer thickness determination.

In this work, thickness determination of thin films was executed with an ellipsometer of type *SD 2302* from *Plasmos Prozesstechnik GmbH* with a fixed incident angle and wavelength of 45° and 633 nm, respectively. A refractive index of 1.46 was used for all types of SAMs consistently [62].

5.6 Current-voltage spectroscopy

5.6.1 Conductive-probe AFM

Conductive-probe AFM (CP-AFM) is a widely used technique to simultaneously obtain spatially resolved information on the topography as well as the local conductivity of a surface [124]. During scans, the sample is raster-scanned in contact-mode while applying a constant DC-bias to the sample. The potential difference with respect to a fixed potential at the conductive tip results in a locally varying current, which is measured at every point of the measurement grid. This signal is amplified by amplifiers of different sensitivities, accounting for the total amount of current flowing through the sample. CP-AFM tips are made of conductive materials such as degenerately doped Si or Si covered with metals such as platinum or an alloy of platinum and iridium.
In this work, samples were mounted onto a stainless steel chuck in a CP-AFM setup (*Nanoscope V Controller, Dimension V Controller, Bruker Nano, extended TUNA* (Tunneling Atomic Force Microscopy) module) with silver conductive paste. Conductance scans were obtained with Pt/Ir-coated Si tips with a curvature <25 nm (*NanoWorld, Arrow^{TM} EFM*). The resulting current of the sample with respect to the ground potential at the tip is detected via TUNA built-in current amplifiers with different sensitivities, as depicted in Fig. 5.1. For electrical characterization of single previously localized spots, such as nanoparticles on a surface or defects, the AFM-integrated closed-loop piezo-feedback control was used to place the tip at the targeted position. For small currents, sensitivities of 1 pA/V or 10 pA/V are used, whereas for higher currents, a less sensitive amplifier of 100 nA/V is applied, enabling the detection of currents up to 1 μA. Typically, a current compliance of 125 pA was set at the amplifier to avoid potential thermal damage to the device under test (DUT) at high currents. When performing DC IV-sweeps at previously defined positions, sweep rates between 0.1 V/s and 1 V/s were used.

5.6.2 Vacuum-probestation

For electrical characterization in two-terminal configuration of samples based on interdigitated electrodes (IDEs), such as described in chapters 7 and 8, samples were mounted in a vacuumed probestation setup of type *Lakeshore TTPX*, which is illustrated in the image in Fig. 5.2. The system is mounted on a shock-free table to minimize mechanical noise potentially originating from a turbo pump maintaining a vacuum of ~5x10^{-6} mbar in the measurement chamber. Vacuum is needed to perform low-temperature measurements using liquid gases such as N_2 or He. Cooling gases are pumped through a capillary, which is placed around the sample stage. Gas in- and outlets are marked in the image as gas supply and exhaust lines. Prior to sample exchange, the turbo pump is separated from the main chamber by closing the vacuum supply valve and gaseous N_2 is provided via a needle valve for venting the chamber. During sample exchange, the chamber is also constantly purged by N_2 to prevent air moisture adhering to the

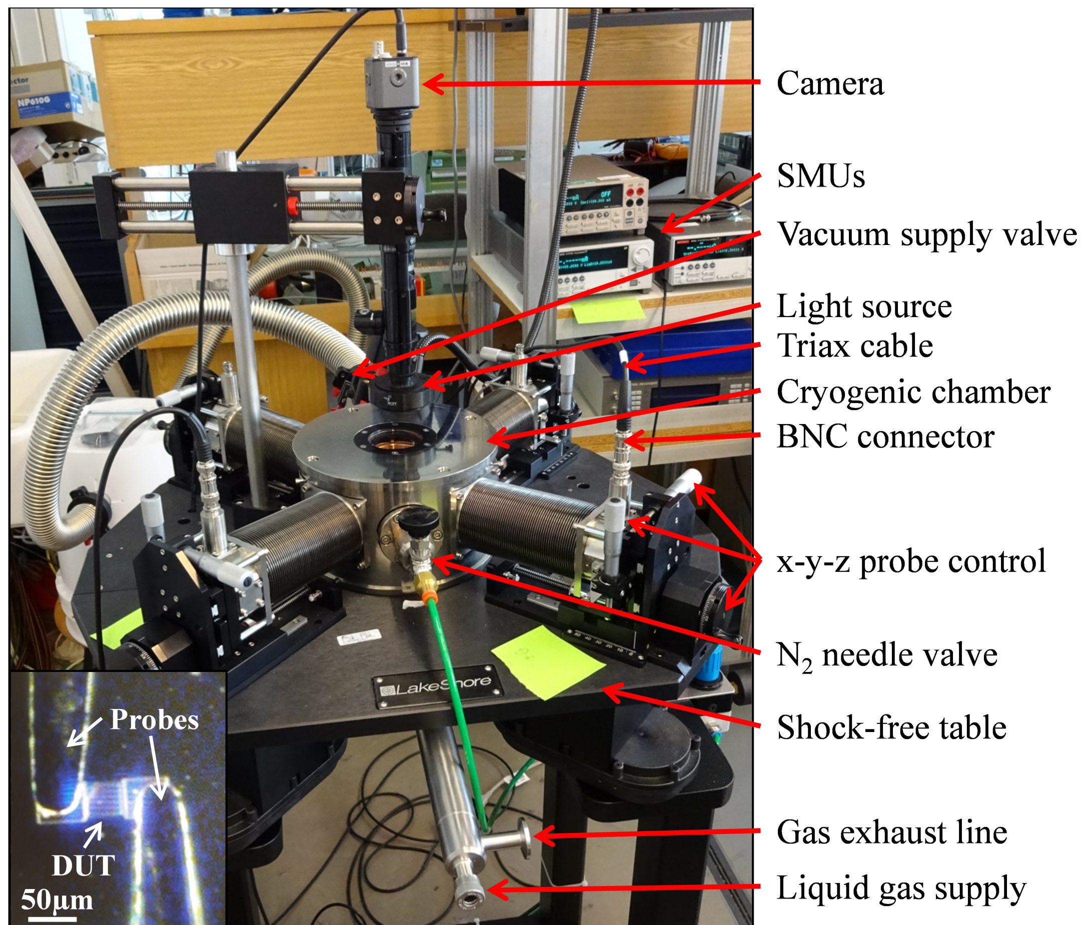

Figure 5.2 Photograph of the probestation setup including labels for all relevant parts. The whole system (*Lakeshore TTPX cryo-probestation*) is placed on a shock-free table to reduce mechanical noise, originating, i.e., from the vacuum pump being connected to the vacuum chamber via the supply valve. For venting the chamber prior to sample transfer, N_2 flow is controlled with a needle valve. Probe arms position is controlled with micrometer screws (x- and z-direction), an additional larger screw (y-direction) and a camera equipped with a light source connected to a separate screen. For electrical measurements, one or more *Keithley 2635B* SMUs in a rack are connected via triax cables and BNC connectors with the probes. In addition, liquid gases for cooling can be inserted into the setup and the gas exhaust is controlled with a separate gas connection. Inset: Typical image of a device under test being connected via two probe tips for two terminal IV-measurements.

chamber surface. In total, four probe arms are available in this setup. At the and of each probe arm, probe tips made of either beryllium-copper or tungsten are located for contacting the sample surface, as illustrated in more detail in Fig. 5.3, showing a cross-sectional view of the main part of the setup. These probe arms are connected to *Keithley* SMUs (source meter units) via BNC connectors (Bayonet Neill Concelman), triax adapters and triax cables, ensuring full shielding of the conductor from sample to SMU. Probe position for sample contacting via probe landing is controlled by micrometer screws and an external camera system equipped with a light source and zoom and focusing unit. The image is acquired through quartz windows in both chambers and monitored on a PC screen. A typical resulting image of a contacted device

under test (DUT) by two probe tips is illustrated in the inset of Fig. 5.2. In the shown inset, the DUT is an interdigitated electrode (IDE) device fabricated by EBL featuring two contact pads on each side for tip landing.

In this work, two terminal IV-measurement were conducted in dark, at room temperature and in vacuum conditions with a pressure of ~5x10^{-6} mbar. Throughout all IV-sweeps, a sweep rate of 10 mV/s and a step size of 0.1 V was used consistently, resulting in a noise level of ~7×10^{-13} A. Measurements were performed controlling SMUs with *Matlab* software and GPIB.

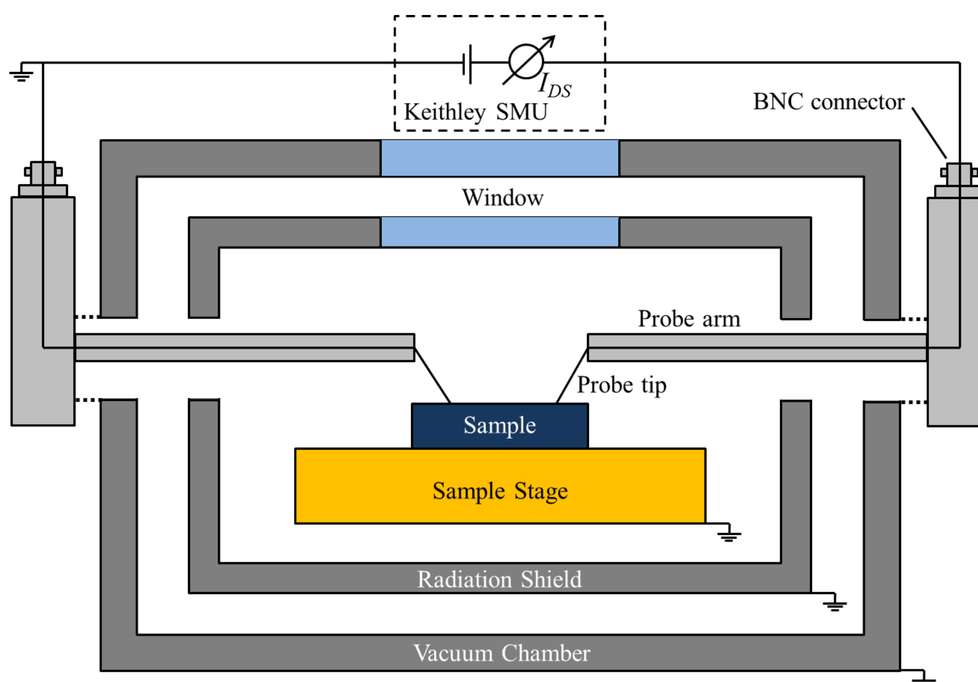

Figure 5.3 Schematic cross-sectional illustration of the probestation setup including used electronic circuitry for two terminal measurements. The sample is placed on a grounded Cu sample stage, which can also be cooled or heated (not shown), whereas the sample surface is contacted with probe tips. These probe tips are connected via probe arms and BNC connectors to the external measurement circuitry via triax cables. The sample stage is enclosed by two grounded chambers, where the outer one is used as vacuum chamber and the inner one as radiation shield. Two quartz windows on top allow for controlling probe arm navigation via an external camera. Measurements were performed with a *Keithley 2635B* SMU connected to a PC via GPIB and controlled with a *Matlab* program.

5.6.3 Hanging mercury droplet electrode

For electrical characterization of planar samples covered by SAMs, such as described in section 4.1.4, sample surfaces were contacted by a hanging mercury (Hg) droplet electrode [77, 78]. Hg is a metal which is liquid at room temperature and features a high surface tension, making it highly suitable for the formation of soft contacts to fragile materials such as SAMs. It is therefore an alternative to solid-state contacts, potentially causing damage to the sample surface. As schematically illustrated in Fig. 5.4 (a), samples were contacted from the backside on a

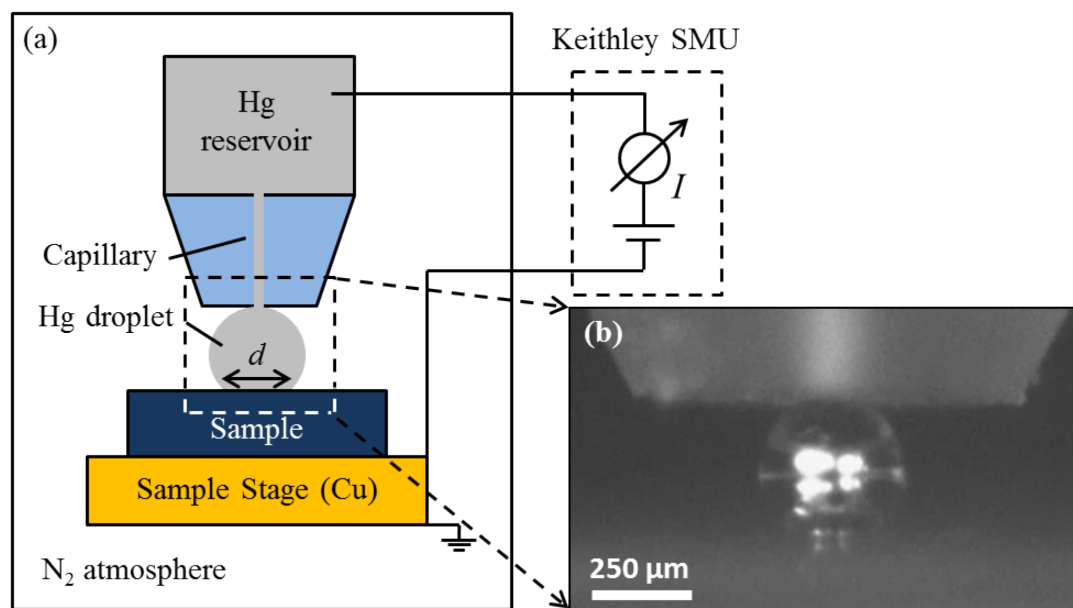

Figure 5.4 (a) Schematic cross-section of the hanging mercury (Hg) droplet setup. Planar samples are mounted and contacted electrically from the backside on a Cu stage, whose lateral and horizontal position is controlled by micrometer screws (not shown). The sample surface is electrically contacted by a soft Hg droplet, which is dispensed by a dispense unit (not shown) through a thin capillary from a reservoir. DC-IV measurements are performed with a *Keithley 2635B* SMU being directly connected to the Hg reservoir and the sample stage. The whole setup is located in a glove box, which is constantly purged by dry N_2 to maintain an inert atmosphere and to protect the environment from poisonous Hg gas. Illumination by an LED panel from the backside and imaging by a camera, which is connected to a PC, allows for precise control of Hg droplet diameter d, as illustrated in image (b), showing the end of the capillary and a typical Hg droplet on a planar substrate.

copper (Cu) stage by metal evaporation (Ti/Au) and silver conductive paste. Prior to sample surface contacting, a Hg droplet of precisely defined volume was dispensed from the reservoir through a capillary (*Bioanalytical Systems, USA*) with an electronically controlled dispense unit (not shown). Due to the high surface tension, the Hg droplet stays hanging at the apex of the capillary. For sample contacting, the stage was slowly moved upwards until the droplet adheres to the surface. It is crucial to not press the sample against the droplet, as this potentially causes the droplet to loose contact to the capillary and therefore also to loose electrical contact to the reservoir. For DC-IV sweeps, the Cu stage and Hg reservoir are both connected to *Keithley* SMUs, which are controlled by a *Matlab* program on a PC via GPIB. The process of contact formation is monitored via a camera connected to a PC, while the droplet is illuminated from behind by a CCD panel. A typical image of a Hg droplet in contact with a surface is shown in Fig. 5.4 (b). For each measurement, such an image was obtained to measure the droplet diameter d to calculate the contact area for conversion of current to current density. Image scale calibration for droplet diameter determination was performed prior to measurements by comparing a structure with known dimensions, fabricated by optical lithography, to the known size of the capillary opening (1050 µm) by *Imagej* program. The whole setup, besides *Keithleys*

and PC, is located in a customized glovebox from *PlasLabs, USA* equipped with a load lock, to protect the environment from poisonous Hg gas and to prevent air moisture to enter the main chamber. In addition, the glovebox is constantly flushed by dry N_2, maintaining a constant N_2 over-pressure and therefore inert atmosphere. This N_2 atmosphere minimizes Hg droplet surface oxidation and also helps to minimize problems arising from air moisture on sample surfaces, potentially causing unstable and non-comparable measurements. Samples featuring metallic surfaces such as thiols on Au are not suitable for this setup, as Hg forms amalgam with most common metals destroying Hg droplet and sample and contaminating the capillary.

6 Directed assembly of silver nanocube threshold selector arrays

6.1 Introduction

In this chapter we demonstrate the formation of regular arrays of functional, nanoscale threshold switching units by the directed assembly of silver nanocubes (AgNCs) onto TiO_2 coated Si substrates. This is in contrast to previous work on metal nanoparticle-based resistive switching units, where the nanoparticles were mostly addressed as layers and, in the case of single particle measurements, not positioned by directed assembly [21–24, 26, 131]. The directionality of our assembly process is based on a specific Cu(I)-catalyzed "click" reaction between the complementary surface functionalization of the AgNCs and the target substrate areas. Electrical characterization of single AgNCs using conductive probe (CP-) AFM techniques shows distinct and reproducible threshold switching with ultra-low OFF currents. The switching mechanism can be assigned to the reversible formation and rupture of Ag filaments in the TiO_2 layer as supported by our detailed kinetic Monte-Carlo (kMC) simulations as well as ex-situ CP-AFM and cross-sectional SEM studies via Focused Ion Beam (FIB) milling. The following chapter is closely related to the work presented in [41] © 2019 WILEY-VCH Verlag GmbH & Co. KGaA, Weinheim.

6.2 Preparation of AgNC arrays

The entire process sequence of molecular functionalization and assembly is schematically depicted in Fig. 6.1. As a first step, the native oxide layer of a highly doped Si chip (c.f. 3.2, p-type Boron, 0.005 Ω cm, 12 mm × 12 mm) was removed by buffered HF solution. Subsequently, a thin layer of Ti (10 nm) was sputter-coated immediately after HF treatment and oxidized in an intense oxygen plasma (600 W, 30 min) to yield a fully oxidized, almost stoichiometric and smooth TiO_2 layer surface.

6.2.1 Substrate oxide coating

The quality of these TiO_2 layers is investigated in close detail by surface-roughness analysis measurements by tapping-mode AFM and XPS, as illustrated in Fig. 6.2. In (a) a typical surface scan of a sputtered and fully oxidized TiO_2 layer of 20 nm thickness by AFM is shown, revealing

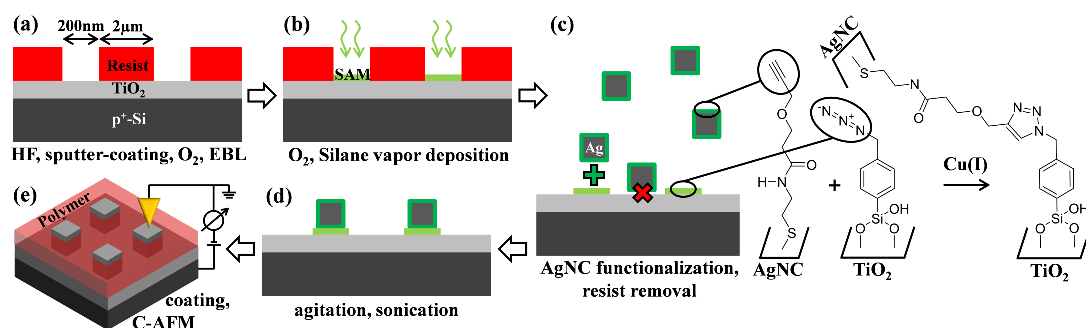

Figure 6.1 Schematic representation of the assembly process. (a) A highly p-type doped Si wafer chip is treated by HF to remove the native oxide layer and then immediately sputter-coated with Ti. The Ti layer is completely oxidized by O_2 plasma and covered with an electron-beam sensitive resist which is subsequently patterned in the form of a square array of square-shaped holes, using electron beam lithography (EBL). (b) The exposed TiO_2 areas are hydroxyl terminated by short O_2 plasma and functionalized by self-assembled monolayers of azido-phenyltrimethoxysilane from the gas phase (light green). (c) Subsequently, the resist template is removed in acetone and the monolayer-patterned surface is exposed to a suspension of silver nanocubes (AgNCs), which are surface-functionalized by thiols featuring alkyne terminal groups (dark green). (d) AgNCs are site-selectively immobilized, with their surface functionalization forming covalent bonds to the complementary functionalized substrate via Cu(I)-catalyzed alkyne-azide cycloaddition. (e) For conductive probe AFM measurements, the space between AgNCs is filled with an UV-curable polymer (planarization) and the surface of the AgNCs exposed again using oxygen plasma in a barrel ashier. Reprinted with permission from [41] © 2019 WILEY-VCH Verlag GmbH & Co. KGaA, Weinheim.

a roughness in the range of the Si substrate (<(0.55 ± 0.13) nm). Additional XPS analysis of the oxide layer shown in (b) reveals several characteristic peaks:

- two major $Ti2p_{1/2}$ and $Ti2p_{3/2}$ peaks at 464 eV and 459 eV, respectively (blue and purple), being assigned to TiO_2, and
- two smaller contributions of $2p_{1/2}$ and $2p_{3/2}$ shells of Ti in TiO at 461 eV and 455 eV (orange and red) [132].

Hence, the estimated stoichiometry of the oxide layer from these XPS data was 92 % TiO_2, 7 % TiO and <1 % metallic Ti. These findings point to the formation of clean, almost stoichiometric TiO_2 after having fully oxidized the whole, deposited Ti film.

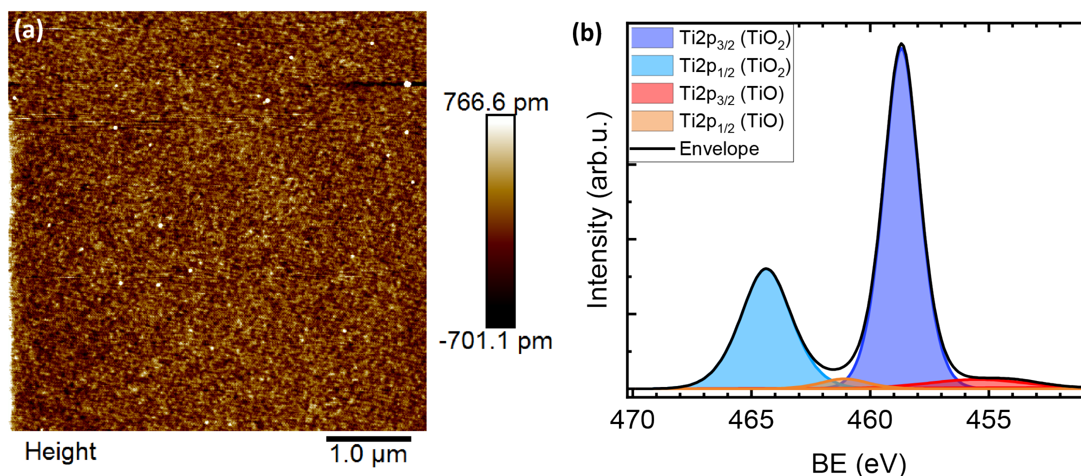

Figure 6.2 (a) Tapping-mode AFM image and (b) XPS spectrum with fits of characteristic Ti 2p peaks of a fully oxidized Ti layer on p-Si. B.E.: Binding Energy. Reprinted with permission from [41] © 2019 WILEY-VCH Verlag GmbH & Co. KGaA, Weinheim.

6.2.2 Patterned self-assembled monolayer growth

To achieve a patterned molecular surface functionalization as target binding sites for the NCs, we employed at first electron-beam lithography (EBL). Specifically, a positive-tone EBL-resist was spin-coated and soft-baked (*Allresist*, AR-P 6200, 4000 rpm/ 60 s, soft-bake: 150 °C/ 60 s, see also sec. 3.6), leading to full coverage of resist of thickness 80 nm. After the sample was patterned by electron beam exposure (*Raith GmbH, eLine*, 30 kV, 90 μC/cm^2, see sec. 4.4) and development (*Allresist*, AR600-546/ 1 min, H_2O/ 30 s, see sec. 3.6), it was cleaved into four equal square areas comprising 200 x 200 square-shaped holes each. Every hole had a size of 200 nm × 200 nm, with a pitch of 2 µm between the holes, cf. Fig. 6.1 (a). As a next step, the exposed TiO_2 surface in the square holes was hydroxyl-activated by short O_2-plasma (100 W, 30 s) and functionalized by self-assembled monolayers of p-azidophenyltrimethoxysilane (APTMS, see sec. 3.6) from the vapor phase. For this purpose, the sample was placed near to a droplet of pure APTMS molecules inside an evacuated desiccator for 30 min. Applying a constant vacuum to the bell jar by continuous pumping, the vapor pressure of APTMS allowed for a continuous transition of molecules from the liquid to the gas phase. Being equally distributed in space, molecules physically adsorb on the available surface, including onto the hydroxyl-terminated TiO_2 surface in the recess holes, see Fig. 6.1 (b) (light green) [40, 60, 110]. Subsequently, chemisorption of APTMS molecules was realized by annealing the sample on a hotplate for 15 min at 130 °C, aiming at the eventual formation of a self-assembled monolayer (SAM) of APTMS. Afterwards, the EBL resist was removed by sonication in acetone for 15 min.

Figure 6.3 (a) displays a tapping-mode AFM image (c.f. Fig. 5.1) of the TiO_2 surface after patterning with a square array of APTMS coated square target sites. Uniform areas of increased

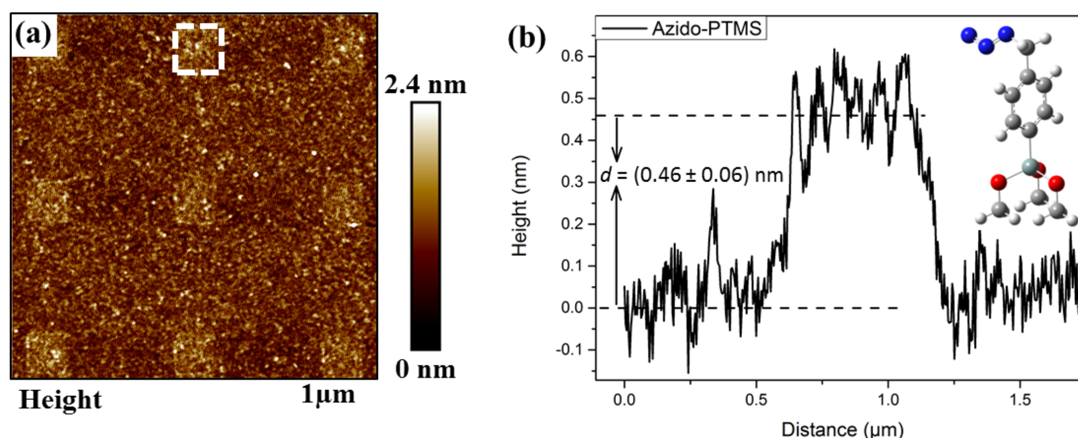

Figure 6.3 (a) Tapping-mode AFM micrograph of a TiO_2 substrate coated with a square array of 500 nm × 500 nm sized azido-phenyltrimethoxysilane SAMs. One square is highlighted with a dashed white line. (b) AFM height profile of a respective SAM area taken from (a). Inset: Molecular structure of an azido-PTMS molecule (white: hydrogen, grey: carbon and silicon, red: oxygen, blue: nitrogen. Reprinted with permission from [41] © 2019 WILEY-VCH Verlag GmbH & Co. KGaA, Weinheim.

height can be recognized, as highlighted by a dashed white line, corresponding to the organic surface functionalization. Typical profile scans, as shown in Fig. 6.3 (b) yield a measured average step height of (0.46 ± 0.06) nm, corresponding to the thickness of a SAM of APTMS molecules tilted by about 60° from the surface normal (for characterization by AFM, SAM areas of 500 nm × 500 nm were patterned instead of 200 nm × 200 nm to achieve better image quality and more reliable measurements of SAM heights). These findings show the successful lithographic patterning of the TiO_2 surface with SAM-coated areas featuring well-defined shape and size.

6.2.3 AgNC ligand exchange

Silver nanocubes (AgNCs) with edge length (98.5 ± 7.0) nm were obtained from *nanoComposix* as described in 3.3. To prepare AgNCs for the selective binding to the APTMS functionalized square areas, their surface was functionalized by a SAM of N-[2-(methylthio)ethyl]-3(2-propyn-1-yloxy) (MTEP), i.e., thiols with alkyne terminal groups, as schematically illustrated in Fig. 6.1 (c) (dark green). In order to achieve that in a step-wise manner, cysteamine (*Sigma-Aldrich*, M9768, purity 95 %) was at first reacted with propagyl-N-hydroxysuccinimidyl ester (*Sigma-Aldrich*, 764221, purity 88 %, concentrations: 5 mM each in EtOH). Next, AgNCs were exposed to the obtained alkyne-thiol product ($5x10^9$ AgNCs, 5 mM MTEP in 1 mL EtOH) by forming a suspension, under constant agitation on an orbital shaker (200 rpm, 24 h) at room temperature. The AgNC polyvinylpyrrolidone (PVP) shell is only physically adsorbed to the cube surface, whereas the thiol terminal group of MTEP forms a covalent bond with the Ag, hence, being stronger and therefore favored. This way, the original PVP shell was substituted by a SAM of MTEP. This was verified by energy dispersive X-ray spectroscopy analysis (EDX) of an

agglomerate of MTEP-functionalized AgNCs, after extensive AgNC washing by centrifugation and re-dispersion in EtOH (>5-times). As can be seen in the respective EDX spectrum in Fig. 6.4, the sulfur peak can be clearly resolved, indicative for successful AgNC ligand exchange [133, 134].

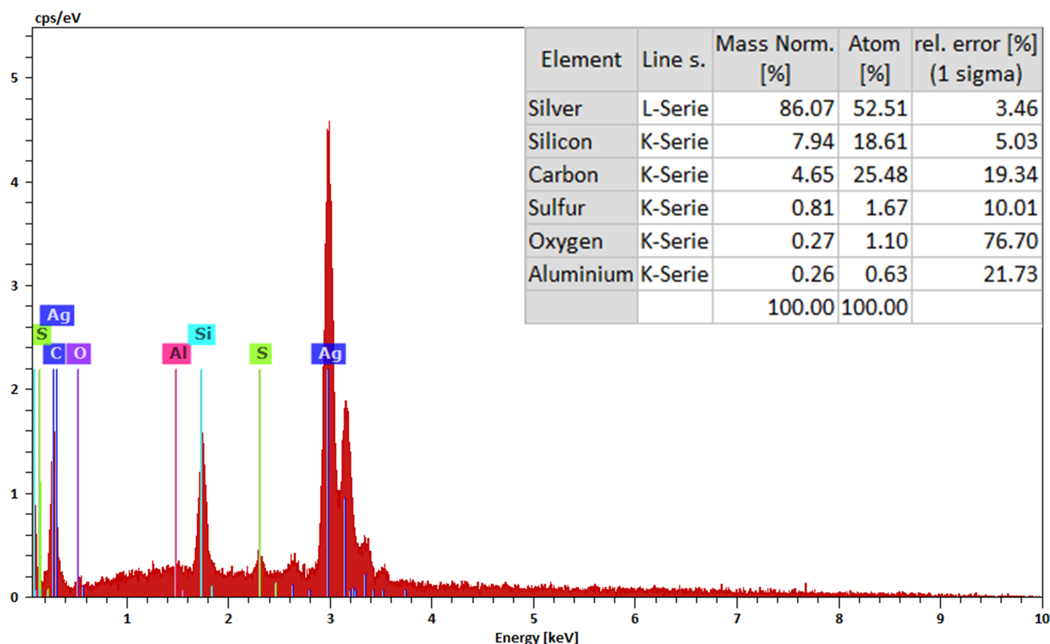

Element	Line s.	Mass Norm. [%]	Atom [%]	rel. error [%] (1 sigma)
Silver	L-Serie	86.07	52.51	3.46
Silicon	K-Serie	7.94	18.61	5.03
Carbon	K-Serie	4.65	25.48	19.34
Sulfur	K-Serie	0.81	1.67	10.01
Oxygen	K-Serie	0.27	1.10	76.70
Aluminium	K-Serie	0.26	0.63	21.73
		100.00	100.00	

Figure 6.4 EDX spectrum of MTEP-functionalized AgNCs, where sulfur is clearly visible, indicative for successful substitution of the as-obtained AgNC PVP shell by MTEP molecules. Inset: relative elemental contents of the sample. Reprinted with permission from [41] © 2019 WILEY-VCH Verlag GmbH & Co. KGaA, Weinheim.

6.2.4 Site-selective immobilization of AgNCs

After MTEP substitution, AgNCs were washed by centrifugation and sonication in ethanol (10.000 rpm, 200 µL, 5 min) three times. Subsequently, the as-prepared AgNCs were assembled on the prepared, SAM-functionalized TiO_2 template areas by placing the sample together with the as-reacted NCs in a vial containing a solution that provided the catalyst to induce the click-reaction using 500 µL of 5 mM Cu(I)-iodide (*Sigma-Aldrich*, 215554, purity: 99.999 %) in pyridine (*Sigma-Aldrich*, 270970, purity: 100 %) [99]. The sample was left in the vial under continuous agitation on an orbital shaker (200 rpm, >72 h). This led to the anticipated, site-selective and thereby directed immobilization of AgNCs at the target square areas on surface, whereby a covalent bond was formed between the particle and the substrate as soon as a particle gets into contact with a respective area. The underlying chemical "click" reaction is shown in more detail in Fig. 6.1 (c), where the azide terminal group of the SAM (light green) forms a triazole linker with the alkyne terminal group on the AgNC surface in the presence of a Cu^{+}-ion via Cu(I)-catalyzed alkyne-azide cycloaddition (CuAAC) [96, 98, 102, 135]. Following

surface assembly of AgNCs, repeated agitation and sonication was employed up to three times for 10 min to remove particles that were only physically adsorbed on the substrate in-between immobilization sites (Fig. 6.1 (d)).

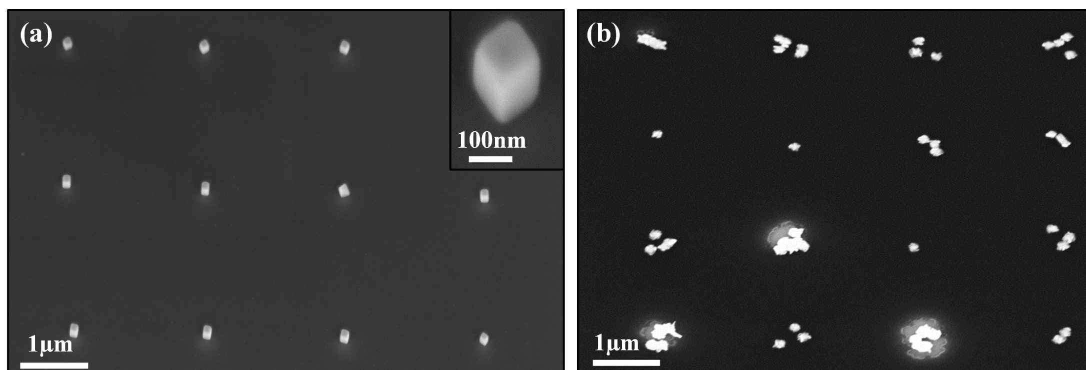

Figure 6.5 (a) SEM image of a representative AgNC-array after directed assembly on 200 nm × 200 nm SAM sites (cf., Fig. 6.1 (d), taken at a tilt angle of 45°. Inset: Close-up view of one NC confirming its cubic shape. (b) SEM image of self-assembled AgNCs on TiO_2 using 500 nm × 500 nm-sized SAM target sites for immobilization. Apparently, typically more than one single AgNC was immobilized per target area. Reprinted with permission from [41] © 2019 WILEY-VCH Verlag GmbH & Co. KGaA, Weinheim.

A typical AgNC-array after assembly but before planarization, i.e., corresponding to Fig. 6.1 (d), is illustrated in the scanning-electron microscopy (SEM) image in Fig. 6.5 (a). Clearly, NCs of side-length 100 nm are located on the surface in a regular manner with inter-particle distance of 2 µm. Hence, they have successfully assembled at their target sites which had been predefined by lithographic pattering of the APTMS SAMs. The inset shows a single AgNC confirming regular cubic shape. A statistical analysis was carried out based on 7 different samples, analyzing one SEM image (index i) per sample, with images capturing different array sizes, ranging from N^i_{SAM} = 14 x 14 to 35 x 35 SAM positions, respectively. In total, $N_{SAM} = \sum_i N^i_{SAM}$ = 3439 targeted SAM-positions were evaluated with respect to their occupation by single AgNCs. We counted a total of N_{NC} = 1365 AgNCs, with N_{NC^+} = 1174 of them positioned at the anticipated position on-SAM, and N_{NC^-} = 191 at a false position (i.e., in-between two SAM areas). We note that SAM fields accommodating more than one NCs were extremely rare (0.1 % range) and have been omitted in our statistical analysis. Averaging the values of all evaluated SEM images translates into a mean yield of $\overline{N^i_{NC^+}/N^i_{SAM}}$ =(36 ± 14) % of all SAM positions being correctly occupied and $\overline{N^i_{NC^-}/N^i_{SAM}}$ =(6.3 ± 4.1) % of all counted particles positioned in-between or near pre-defined SAM areas. Hence remarkably, a clear majority of NCs was site-selectively assembled just by molecular recognition based on the complementary functionalization of the TiO_2 surface and the NCs, respectively, without the need of any physical template such as a supporting array of holes or grooves [136]. Larger target SAM areas (500 nm × 500 nm) led to the assembly of typically more than one nanocube per SAM, as anticipated by upscaling the exposed, chemically active area, as can be seen in Fig. 6.5 (b).

As a control experiment, we have finally carried out the same assembly sequence, however omitting the Cu(I) catalyst, which is needed to trigger the click-reaction: the yield of NCs adsorbed at SAM-functionalized squares was now in the range <1 ‰ only, demonstrating the high chemical selectivity of the assembly process. In detail, Fig. 6.6 shows two typical SEM images of a sample after self-assembly, where the Cu(I) catalyst was omitted. Apparently, in (a), AgNCs are randomly distributed over the surface before sonication. However, after sonication, nearly all AgNCs are removed from the substrate, and no specific binding at respective target SAM-sites is obtained. Hence, AgNCs were only physically adsorpt to the substrate. This finding is a strong indication for the selectivity of the immobilization process, where covalent binding is only achieved in the presence of the catalyst.

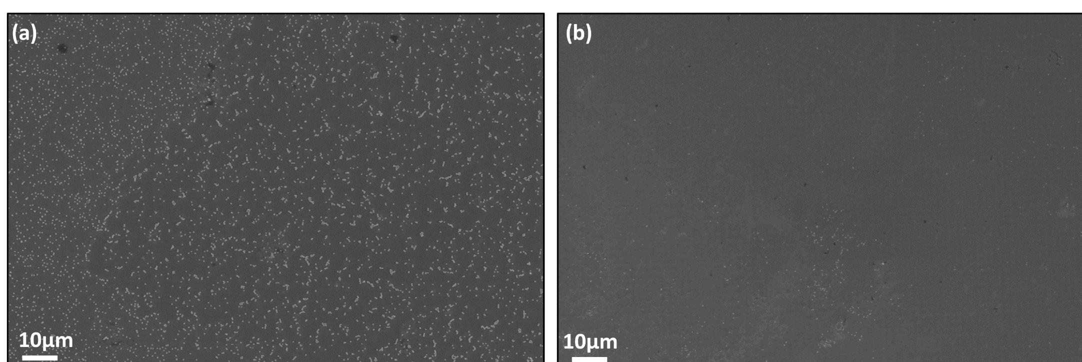

Figure 6.6 SEM images of the result of a self-assembly reference experiment without Cu(I) catalyst: SEM images of the same sample (a) before and (b) after sonication. No site-selective immobilization is observed, indicating selectivity of the process. Reprinted with permission from [41] © 2019 WILEY-VCH Verlag GmbH & Co. KGaA, Weinheim.

6.2.5 Planarization of AgNC arrays for CP-AFM measurements

As depicted in Fig. 6.1 (e), as a last step the space between AgNCs was filled by a ca. 80 nm thick planarization layer of an UV-curable polymer (*Allresist*, AR-N 7520) by spin-coating (6000 rpm, 1 min) and UV-light exposure in a mask-aligner (*Karl Süss, MJB 3*, 250 W, 1 min). Subsequently, a short O_2-plasma is applied in a barrel ashier (*Alpha Plasma*, 200 W, 20 s), in order to expose and clean the top facets of the NCs. This additional planarization step is required to carry out CP-AFM surface scans of the assembled NC arrays, as without planarization layer the tip might also unintentionally measure current through the oxide while raster scanning.

6.3 Electrical characterization of AgNC arrays by CP-AFM

Having successfully surface-assembled the NCs and the space between AgNCs filled with an UV-curable polymer as described in sec. 6.2.5, surface conductance scans were carried out using Conductive-Probe AFM (CP-AFM), as described in sec. 5.6.1 (cf. Fig. 6.1 (e)). Fig. 6.7 (a) and (b) illustrate corresponding height profile and conductance maps of a typical

3 x 4 AgNC-array, respectively. Exposed AgNC top facets protrude from the surrounding polymer by (29.0 ± 2.2) nm (Fig. 6.7 (a)). The inter-particle distance after planarization has not changed with respect to the average value directly after surface assembly, and is measured to be (1.96 ± 0.10) µm. We assign this finding to the apparently strong adhesion of the NCs to the substrate, promoted by the covalent triazole bond, which even withstands polymer spin-coating. The corresponding conductance scan in Fig. 6.7 (b) reveals small, yet distinct currents in the range ~(0.33 ± 0.13) pA (at 5 V sample bias), exactly at the positions of most particles that were localized in the height map.

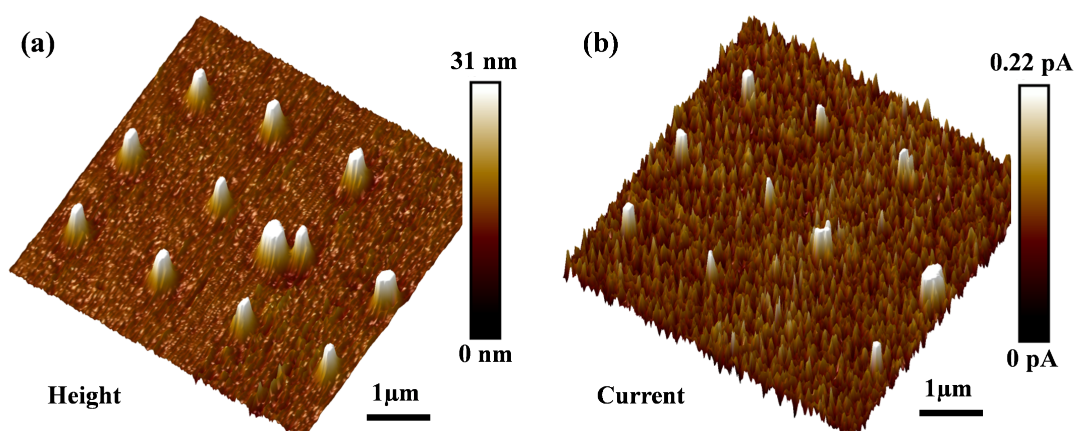

Figure 6.7 (a) and (b) height and current maps of a 4 x 3 NC array after planarization, respectively (cf. Fig. 6.1 (e)), both obtained by CP-AFM at a fixed sample bias of 5 V. Reprinted with permission from [41] © 2019 WILEY-VCH Verlag GmbH & Co. KGaA, Weinheim.

6.4 Electrical characterization of individual AgNCs by CP-AFM

We investigated the electrical properties of single AgNCs using CP-AFM techniques. After localization and pre-characterization by height and current mapping (cf., Fig. 6.7), the AFM tip was positioned at the exact coordinates on one selected NC, contacting it on its top facet. For current-voltage (IV) -measurements, cyclic voltage sweeps with a typical constant sweep rate of 1 V/s were carried out. Fig. 6.8 (a) shows a representative IV measurement of a single AgNC on 10 nm TiO_2/ p^+-Si, where the applied voltage and resulting current are plotted together as a function of time in red and blue, respectively.

Several prominent features can be observed. Initially, for low bias voltage, the conductance is low with currents of the order of 0.1 pA (noise level), corresponding to a high resistance state (HRS). This low conductance is consistent with the one usually measured during the conductance mapping reported in Fig. 6.7 (b). When ramping up the bias however from 0 V to -10 V an abrupt change of resistance from a high resistance state (HRS) to a low resistance state (LRS) is observed at a characteristic threshold voltage -V_{th} (indicated by a black circle in Fig. 6.8 (a)). Here, the current rapidly rises up to the pre-set compliance current I_{CC} =

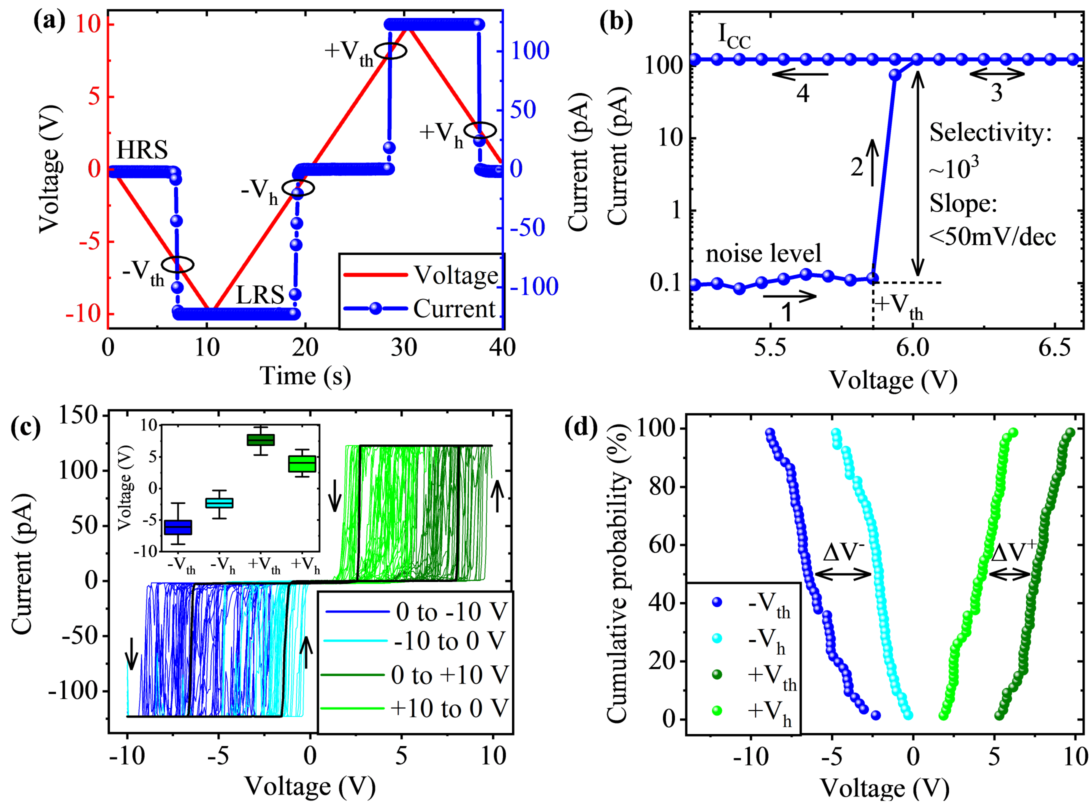

Figure 6.8 (a) DC bias voltage with respect to the AFM tip (red) and measured current (blue) as a function of time for a single AgNC on 10 nm TiO_2/ p^+-Si, obtained with a sweep rate of 1 V/s. Monostable threshold switching is observed at critical threshold ($\pm V_{th}$) and hold voltages ($\pm V_h$). Data show the second measurement cycle. (b) Semi-logarithmic plot of one ON switching process occurring at $+V_{th}$. (c) A total amount of 63 measured DC I-V-sweeps, taken from 27 NCs distributed over 5 different samples was acquired. The maximum number of sweeps per one single NC was 21. One single, example IV-curve is shown in black for clarity. Inset: Box chart of threshold and hold voltages, showing mean values, standard deviations and min/max outliers. Black arrows indicate the measurement direction. (d) Cumulative probabilities of threshold and hold voltages for both positive (green) and negative (blue) voltages. Reprinted with permission from [41] © 2019 WILEY-VCH Verlag GmbH & Co. KGaA, Weinheim.

-125 pA of the amplifier. Having reached the chosen maximum voltage V = -10 V the sweep direction is reverted such that the bias is now ramped from -10 V to +10 V, and finally back to 0 V. As apparent from Fig. 6.8 (a), the LRS is only maintained at large enough negative bias. Having reached a characteristic second threshold (hold) voltage ($\pm V_{th}$) the system switches back to its original HRS. This behavior is observed at both negative and positive voltage polarities and eventually results in characteristics that feature always the HRS around zero bias while for a high enough absolute bias the LRS is maintained, in a hysteretic manner. Such characteristics is commonly referred to as threshold switching (TS) and has been reported for a range of related junctions comprising Ag in different material combinations, including, e.g., Ag/SiO_2/Pt, Ag/TiO_2/Pt, Ag/a-Si/Pt and Ag/HfO_x/Pd [8, 137–142].

Such mechanism is in marked contrast to memristive switching behavior which is investigated

for non-volatile resistance random access memory (RRAM) cell applications and relies on reproducible switching of the low-bias resistance. Memristive switching has been observed for a large variety of material combinations, too, including, e.g., for electrochemical metallization cells based on Ag-electrolyte systems [19, 143]. We assign the mechanism of TS in our system to be based on conductive Ag filament formation, and their reversible rupture in the low bias regime. The abrupt increase of current is investigated to more detail with the help of Fig. 6.8 (b),

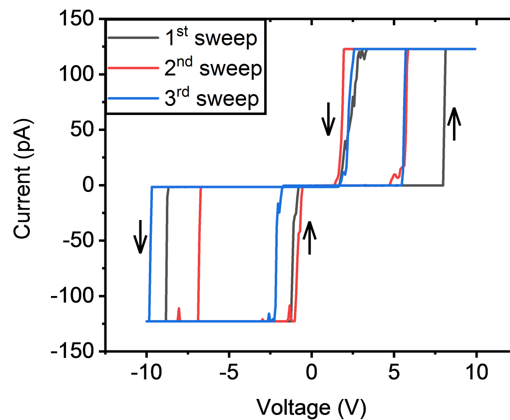

Figure 6.9 The first three DC IV-sweeps of one particular AgNC device. No significant trend in threshold voltages with number of cycles, and no distinct forming curve for cycle #1 can be observed. Reprinted with permission from [41] © 2019 WILEY-VCH Verlag GmbH & Co. KGaA, Weinheim.

displaying an excerpt of a typical IV-curve on a semi-logarithmic scale. The switching event features a steep slope of <50 mV / current decade and a high selectivity (ON-OFF ratio) between the two conductance states of at least ~103, here limited by the value of the compliance current. To investigate device-to-device variations, all measured cyclic IV-traces (63 measurements in total, carried out on 27 different AgNCs located on 5 different samples) of AgNCs on 10 nm TiO_2/ p^+-Si are summarized in Fig. 6.8 (c), where IV-sweeps in the negative and positive voltage bias region are presented in blue and green, respectively. We note that we did not observe any distinct "forming curves" for measured first cycles, which could be distinguished from all subsequent cycle data, for a certain AgNC, as can be seen in Fig. 6.9.

As apparent from Fig. 6.8 (c), we rather observed a certain overlap region where for the whole distribution of threshold and hold voltages absolute values of Vth for a given voltage scan may be smaller than Vh for a different one. Hence, there is a small probability that, in the intermediate voltage regime, either the HRS or LRS may be observed for any given new sample. This is evaluated to more detail in the box chart plot in the inset of Fig. 6.8 (c), showing mean values with standard deviations and outliers as error bars. Still however, the cumulative probability plot in Fig. 6.8 (d) shows sufficiently narrow distributions of critical voltages. Both HRS and LRS of the system can be reliably addressed at both negative and positive voltages with large separation of $\Delta V^- = (-3.8 \pm 1.9)$ V and $\Delta V^+ = (3.6 \pm 1.7)$ V as derived from mean values with standard

deviations at a cumulative probability value of 50 %. We note that the bias scan speed has only minor influence on the distribution of switching voltages and their variance, as tested for rates between 0.1 V/s and 2.0 V/s as shown in Fig. 6.10. In Fig. 6.10 (a), six exemplary IV-sweeps obtained using different sweep rates are shown, with the respective threshold and hold voltages for negative and positive bias marked with blue and green circles, respectively. Apparently, no significant dependency of sweep rate on critical voltages is obtained in the range of uncertainty arising from measurement instabilities. This is further verified in Fig. 6.10 (b), where the mean values with standard deviations of switching voltages as a function of sweep rate obtained from nine different samples are shown. Here, also no significant trend can be seen. The observed

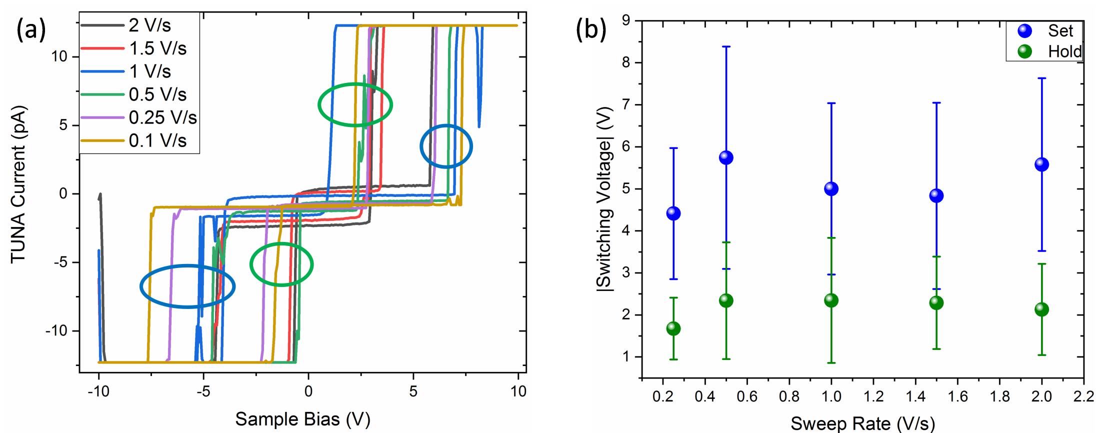

Figure 6.10 (a) Variation of sweep rate for a single AgNC on 10 nm TiO_2/ p^+-Si and (b) average threshold and hold voltages in blue and green, respectively, as a function of sweep rate for 9 measured devices. No significant trend is visible in this range. Reprinted with permission from [41] © 2019 WILEY-VCH Verlag GmbH & Co. KGaA, Weinheim.

distribution with partially overlapping threshold and hold voltage ranges, as observed in Fig. 6.8 (c), may have different origin. On the one hand, a certain contribution could stem from local, slight variations in TiO_2 density and thickness. However, detailed analysis of the oxide showed homogeneous film quality and stoichiometry: AFM tapping mode analysis of the bare TiO_2 surface revealed a small rms-roughness of (0.55 ± 0.13) nm comparable to the roughness of the Si substrate (compare Fig. 6.2 (a)). Additional XPS analysis of a TiO_2 film with a thickness of 20 nm in Fig. 6.2 (b) revealed the formation of almost stoichiometric TiO_2 [132]. More likely on the other hand, is the possibility of a large impact of tip vibration due to thermal and acoustic agitation and of contact tip position due to sample stage drift, all potentially causing variation of the tip-to-NC interfacial resistance. These effects would also limit the maximum number of cycles that could be measured per NC with our setup. Additionally, the tip surface might suffer from accumulation of residues of planarization polymer caused by scanning, potentially leading to increased contact resistance as well. This observation is in line with the relatively large bias in the range of several volts, needed to trigger the switching events as compared to similar systems [140, 141].

6.5 Kinetic Monte-Carlo simulation of ion migration

The phenomenon of threshold switching (TS) has been intensively investigated during the past years [137, 138]. Several studies propose a switching mechanism based on Ag-ion migration, where Ag atoms are oxidized at the positively biased anode (the NC in this case), migrate through the electrolyte (here, the TiO_2 layer) in the direction of the applied electric field and are finally reduced and immobilized as Ag atoms at the cathode (the p^+-Si substrate). With time, a conducting filament (CF) starts to grow from the cathode towards the anode (cf. sec. 2.2). As soon as it reaches the anode, strongly increased current can flow and the system switches abruptly from the HRS to the LRS. However, the stability of the CF is strongly dependent on the value of compliance current I_{CC}. In fact, J. Song et al. have shown a dynamic variation between a non-volatile memory switching for high values of I_{CC}, and a threshold switching for small I_{CC} (<10 µA for a Ag/TiO_2 system) [144]. This can be explained by the fact that for high I_{CC} more material is being deposited and therefore the CF becomes more stable as compared to smaller I_{CC}, where the CF is supposed to be thinner and therefore less stable in the low-voltage regime. As a result, for small voltages the filament would spontaneously decompose into small spherical islands, to minimize the surface free energy. This phenomenon can be described within the framework of Rayleigh instability and has been shown to be a suitable description for filament instability in analogue systems [145]. To closely investigate CF formation in our specific case of Ag-TiO_2-Si junctions, a kinetic Monte-Carlo (kMC) model (cf. sec. 2.6) was developed and applied by the group of Prof. A. Gagliardi (Waldemar Kaiser and Michael Rinderle, simulation of nanosystems for energy conversion, department of electrical and computer engineering, TUM). Based on the results of our theoretical model calculations, we have analyzed under which conditions filaments form, how long the formation takes and how the results compare with our experimental data. Previous studies show that the kMC model is suitable to simulate filament formation in memristive devices [146–149]. In this work, our kMC model describes the migration of Ag^+ ions within TiO_2, the detachment of Ag atoms from the top contact and the reduction at the bottom contact or in proximity to an already reduced Ag atom within the electrolyte (cf. sec. 6.5). These processes are modeled by transition rates ν_{ij} using an Arrhenius law given by

$$\nu_{ij} = \nu_0 \times \exp\left(-\frac{\Delta E_{ij}}{k_B T}\right) \tag{6.1}$$

The transition rate ν_{ij} describes the number of transitions per second from an initial system state i to the final state j. It depends on the energy barrier or activation energy ΔE_{ij} of the process, Boltzmann's constant k_B and the temperature T. We use a constant attempt-to-escape frequency $\nu_0 = 10^{12} s^{-1}$ typical for atomistic processes. The process-depending physical properties enter

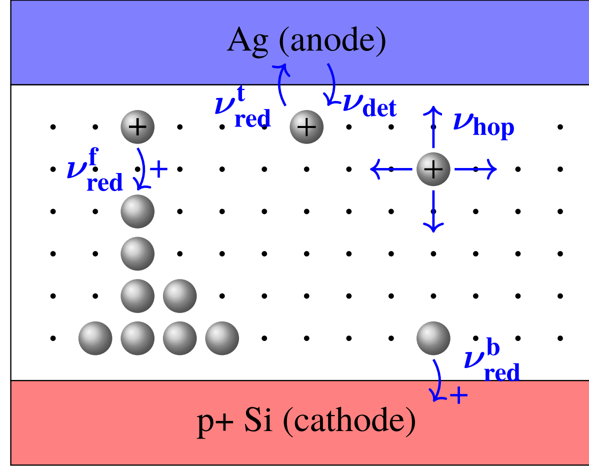

Figure 6.11 Schematic representation of the kinetic Monte Carlo simulation setup including all relevant layers and ion transitions. Transition rates ν_{ij} include the detachment rate ν_{det} of ions from the anode, hopping rate ν_{hop} inside the oxide layer as well as reduction rates ν^t_{red}, ν^b_{red}, ν^f_{red} at anode, cathode and incomplete filament, respectively. Reprinted with permission from [41] © 2019 WILEY-VCH Verlag GmbH & Co. KGaA, Weinheim.

in the activation energy. All physical transitions are schematically represented in Fig. 6.11. For the migration of Ag^+ ions, the energy barrier ΔE_{hop} can be decomposed into

$$\Delta E^{ij}_{hop} = E_a + \Delta E^C_{ij} + \Delta E^F_{ij} + \Delta E^\sigma_{ij} \tag{6.2}$$

In addition to the local potential difference between two neighboring lattice sites the ions must overcome the activation energy E_a to perform a hopping process. This energy is set to $E_a = 0.61$ eV corresponding to experimentally observed diffusion coefficients [150]. The diffusion coefficient in a 3-dimensional structure is defined as

$$D = \frac{\langle x^2 \rangle}{6t} \tag{6.3}$$

with $\langle x^2 \rangle$ being the square of the average hopping distance and t the time elapsed for the transition. The local potential difference ΔE_{ij} can be decomposed into three parts. The impact of the electric field generated by the applied voltage is implemented by

$$\Delta E^F_{ij} = \frac{eV_{bias}}{z_{box}} \cdot \Delta z \tag{6.4}$$

with the electron charge e, the bias voltage V_{bias}, the thickness of the TiO_2 layer z_{box} and the hopping distance in z-direction Δz. The Coulomb interaction between the Ag^+ ions and their image charges is implemented by the term ΔE^C_{ij} and the local potential structure of the TiO_2 layer by ΔE^σ_{ij}. We assigned a potential value to every lattice site following a Gaussian distribution with an energetic disorder σ. In addition to the random energetic potential structure

of TiO_2 we simulate correlated potential structures with a model described elsewhere [151]. A correlated potential structure leads to preferred pathways for ion transport, because of locally reduced energy differences between lattice sites. We justify this assumption by the fact that beginning filament formation leads to an increased electric field along the filament pathway. Additionally, Joule heating along paths of high ion transport helps to activate hopping processes thermally [7].

The oxidation and detachment of Ag atoms at the top contact is incorporated in our model with the detachment rate $\nu_{det,i}$ for each site [147]. The activation energy for the detachment process is chosen as

$$\Delta E_{det} = E_a + \Delta E_{ij}^{\sigma} \tag{6.5}$$

with $E_a = 0.78$ eV to match experimental data for filament formation and it is assumed to be constant, i.e., independent of position at the top contact and of local electric fields. Neglecting the disordered potential at the first TiO_2 layer next to the contact is not sufficient to describe filament formation. Especially for high bias voltages constant detachment rates lead to a uniform distribution of Ag atoms without distinct filament formation. It is more realistic to implement locally preferred detachment centers accounting for the correlated potential structure of the TiO_2 layer, the inhomogeneity of the electric field due to the cubic structure of the AgNC and the forming filament. We account for that by calculating the activation energy at every contact site relative to the potential of the neighboring TiO_2 site incorporating the energetic disorder ΔE_{ij}^{σ}. If a site next to the contact is already occupied by a Ag^+ ion no further detachment is possible, and the rate at this site is zero. The total detachment rate ν_{det} is summed up over all neighboring sites of the anode. After each transition the detachment rate is updated to account for the occupied sites in the TiO_2 layer. The reduction of ions at the bottom contact ν_{red}^b or at previously reduced Ag atoms ν_{red}^f is modeled as an instantaneous process. Therefore, the reduction rates are $\nu_{red}^b = \nu_{red}^f = \nu_0$. The position of the Ag atom is fixed when being neutralized. The third implemented reduction process happens directly at the top contact. For the calculation of ν_{red}^t an energy barrier of $\Delta E_{red} = 0.64$ eV is used according to Dirkmann et al. [146]. Especially for lower external bias voltages this process is of importance. At low fields the hopping of ions through the TiO_2 layer is suppressed such that many ions may accumulate at the top contact and are reduced back to the Ag anode. This leads to a reduction of the detachment rate until detachment and reduction are equally probable. In this case, filament formation is suppressed.

The system under investigation is modeled using a 50 nm × 50 nm × 10 nm simple cubic lattice of TiO_2 with periodic boundary conditions in x- and y-direction, a silver electrode on the top and a p^+-Si electrode at the bottom of the structure. The thin organic monolayer at the interface between TiO_2 and Ag is neglected in the model. The lattice constant of the cubic grid is chosen to be $a = 1$ nm and the temperature is set to 298 K. Simulations on filament formation were performed for bias voltages ranging from 0.1 V to 7 V to account for fluctuations in tip-to-AgNC contact resistance and for energetic disorder ranging from 50 meV to 100 meV. We studied the

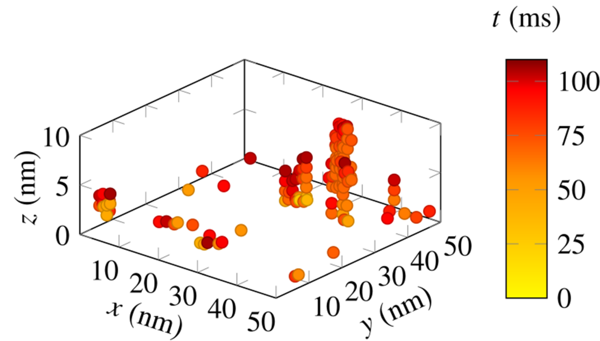

Figure 6.12 Resulting filament structure, with each dot representing one Ag cluster at a simulation lattice site. The color indicates the simulation time, i.e., the elapsed time until formation of the cluster comprising immobilized Ag atoms. Reprinted with permission from [41] © 2019 WILEY-VCH Verlag GmbH & Co. KGaA, Weinheim.

impact of different potential structures without correlation, and with a correlation length of $l_C = 2$ nm and $l_C = 5$ nm. Here, the correlation length l_C nm is a measure of the size of local clusters of low disorder (for further details, refer to Kaiser et al. [151]). The maximum simulation time was set to $t_{max} = 5$ s. Fig. 6.12 depicts a resulting filament structure consisting of small Ag clusters represented by colorized dots immobilized at lattice sites of the simulation grid. The color scale ranging from yellow to red indicates the beginning and the end of the simulation, respectively. Due to correlation, clustering of Ag atoms at only few positions is visible, where the largest agglomerate reaches to the Ag anode. Fig. 6.13 shows the simulated filament formation times t_f as a function of V_{bias} and σ for (a) no correlation, (b) a correlation length of $l_C = 2$ nm and (c) of $l_C = 5$ nm on a semi-logarithmic scale. Apparently, filament formation takes place faster with rising bias voltage and larger disorder. For small bias voltages, the electric field energy difference ΔE_{ij}^F is small compared to the activation barrier E_a. Thus, most ions stay at the top contact and reduction-oxidation cycles are dominant. Ion migration through the TiO_2 film is unfavorable, leading to long filament formation times. For higher bias voltages the migration of ions towards the cathode is enhanced and reduction processes at the top contact are suppressed, which leads to faster filament formation. Like Qin et al. we see that for low voltages the forming time is determined by the migration speed of ions, whereas for higher voltages the oxidation rate at the top contact becomes a limiting factor [148].

In correlated potential structures the energy barriers ΔE_{ij} are lowered along paths with favorable ΔE_{ij}^σ, leading to faster ion migration along such paths. At higher energetic disorder hopping away from energetically preferred paths is suppressed, leading to strongly directed ion migration and faster filament formation. As a second effect, the oxidation rate into preferred paths is energetically more favorable at higher energetic disorder. For lower energetic disorder ions can leave preferred paths more easily and oxidation occurs more evenly across the anode. Hence, ions distribute homogeneously across the medium. Increasing V_{bias} accelerates the ions towards the cathode but because of their homogeneous distribution filament formation is not sped up

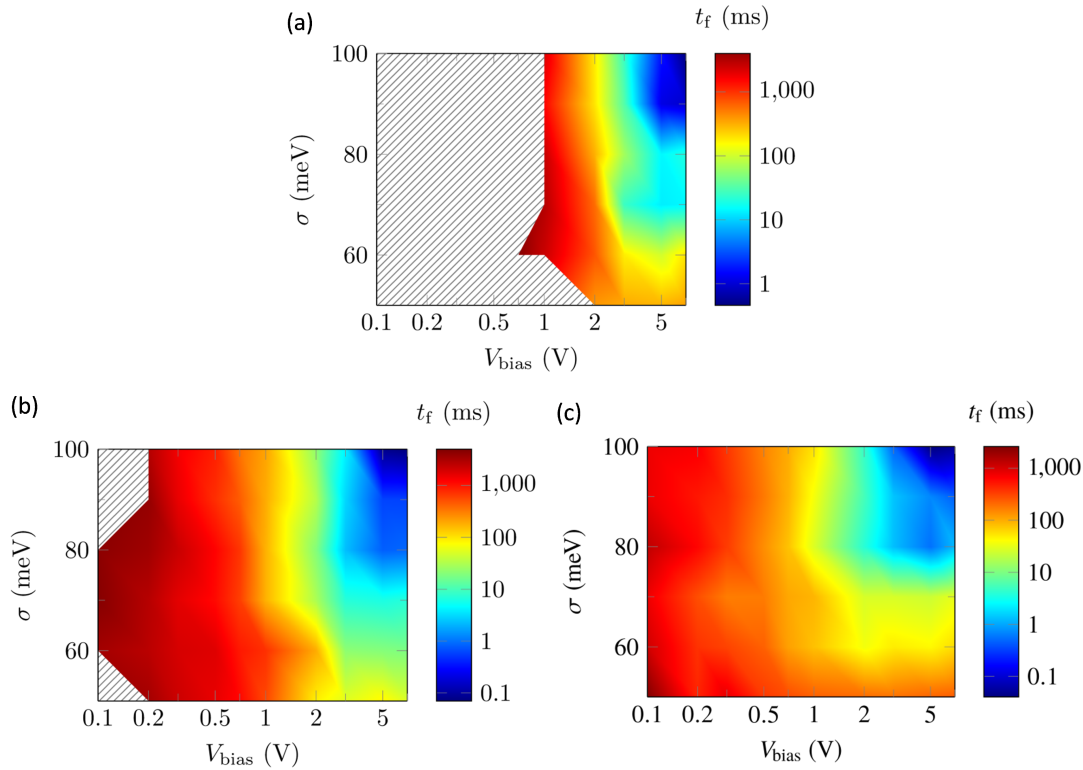

Figure 6.13 Total filament formation time t_f as a function of bias voltage V_{bias} and disorder σ for a correlation length of (a) no correlation, (b) a correlation of l_C =2 nm and (c) a correlation of l_C =5 nm. Reprinted with permission from [41] © 2019 WILEY-VCH Verlag GmbH & Co. KGaA, Weinheim.

as much as for larger energetic disorder. For uncorrelated structures and low bias voltages no filament formation was observed, as can be seen in Fig. 6.13 (a) and (b). Due to the absence of energetically preferred paths no ion migration occurs and an equilibrium of ion oxidation and reduction directly at the top contact is reached. With increasing bias voltages filament formation can occur, but because of missing favorable paths formation times are up to one order of magnitude higher than for correlated structures.

Averaging the duration of on-switching events such as exemplary depicted in Fig. 6.8 (b) of all our experimentally measured IV-ramps, a mean set time of (290 ± 174) ms was obtained. No significant differences in on-switching times between first (forming) and subsequent cycles were observed within this distribution. Still, comparing this average value to the results from our model (which actually describes the process of initial filament growth), formation within such a time span of a few 100 ms is indeed predicted over a wide range of disorders and voltages (Fig. 6.13 (c), orange color). As certain modeling parameters (reduction rates, activation energies etc.) are not precisely known for our actual experiment and could only be based on literature values, a further quantitative analysis remains beyond the scope of this work. Similarly, other conduction mechanisms (e.g., oxygen vacancy filaments in TiO_2) cannot not be fully excluded and may partially contribute, too. Nevertheless, we assign the obtained

good agreement as strong support for our interpretation of the predominant threshold switching mechanism, which is based on the formation and rupture of Ag filaments in TiO_2.

6.6 Characterization of conductive filaments

To further support the hypothesis of threshold switching based on Ag conductive filaments, we have mechanically removed some AgNCs from the surface after measurements and carried out CP-AFM measurements and cross-sectional FIB/SEM studies in the region of previous cube locations. In addition, the kMC model was expanded by a local electric field component.

6.6.1 Structural investigation of conductive filaments by CP-AFM

After single AgNCs were localized and electro-formed by application of a forming voltage of 5 V to 9 V by CP-AFM, AgNC removal was carried out by mechanical delamination, as schematically described in Fig. 6.14 (a). Therefore, the surface of samples was at first coated by acetone for a few minutes by dispersing a few droplets from a pipette, dissolving the planarizing layer. Subsequently, the acetone and dissolved planarizing layer were removed by careful application of a Q-tip, not pressing it onto the surface but by dragging it slowly over the surface. This way, the underlying TiO_2 layer was exposed. Afterwards, to remove residues of acetone, the surface was covered in isopropanol for ~30 s and the sample was blown dry with a N_2 gun. The described delamination process is carried out directly on the AFM stage, with samples still electrically mounted to be able to find the respective area of interest again by engaging the tip after delamination. Hence, during application of acetone, it is crucial to not use to much volume such that only the sample surface and not also the sample backside gets into contact with acetone to avoid Ag glue dissolution and therefore sample displacement or loss of electrical back-contact. In addition, the application of the Q-tip has to be executed without force to minimize risk of TiO_2 layer damage.

A typical current map at a small sample bias of 2 V to 4 V of an electro-formed AgNC on 10 nm TiO_2, i.e. after switching into the ON state for the first time, is illustrated in Fig. 6.14 (b). Clearly, the solid spot of enhanced current (denoted as current AgNC) corresponds to the AgNC, being slightly larger then the actual side-length of 100 nm due to scanning imperfections. However, measuring the same spot with a small bias of 2 V after delamination, as shown in Fig. 6.14 (c), a completely different current image is obtained (denoted as current CFs). In detail, several bright features of enhanced conductivity can be observed, distributed along the sides of a square-shaped area, as depicted by the white dashed line. This square-shaped area has a side-length of ~100 nm, reflecting dimensions of the AgNC, which was located at this position before.

The described procedure was executed for four different TiO_2 layer thicknesses (2 nm to 15 nm). For each thickness, at least five samples were investigated with one or more AgNCs. Resulting exemplary current maps at the position of single, previously electro-formed AgNCs

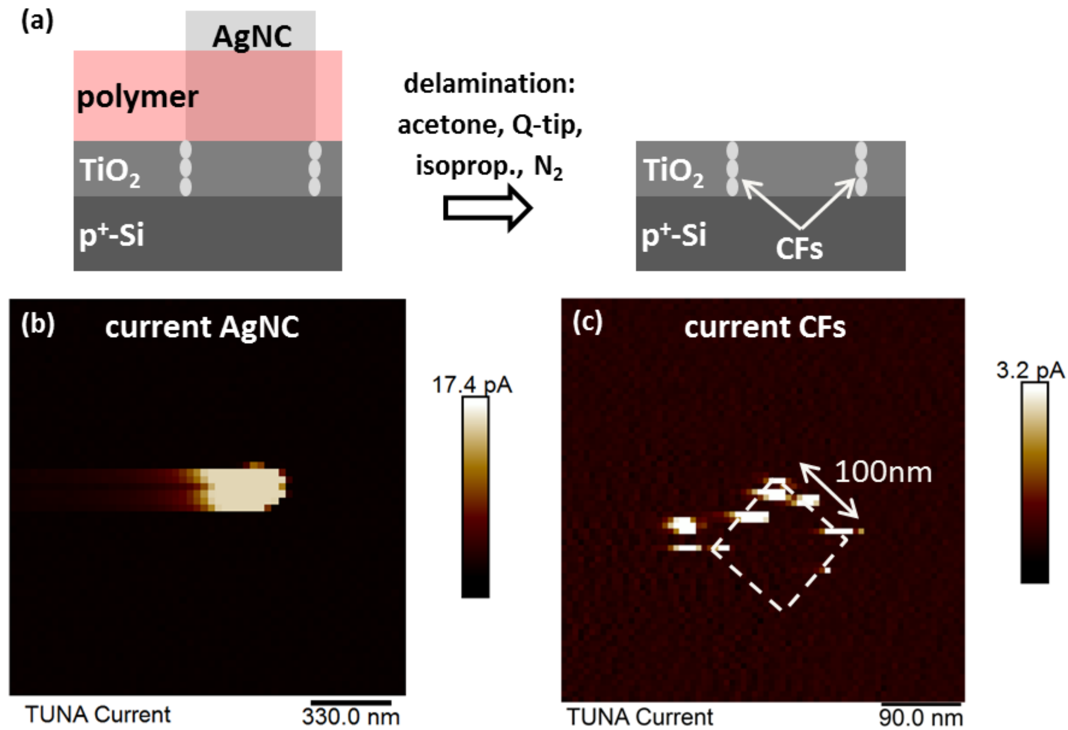

Figure 6.14 Schematic of conductive filament (CF) localization via ex-situ CP-AFM. (a) After localization and electro-forming of single AgNCs, the planarizing layer and AgNC array was removed via mechanical delamination by solvents and Q-tip, exposing the underlying TiO_2 layer. Resulting current maps (b) before and (c) after delamination show different local conductivity. Before AgNC removal, a solid area of large conductivity at AgNC position is observed. After delamination, small, locally defined spots of enhanced conductivity distributed below previous AgNC edge position (dashed white box) are obtained, being assigned to Ag CFs.

after delamination at a small positive sample bias of 2 V to 4 V are shown in Fig. 6.15 (a). For a small oxide thickness of 2 nm, only a single defined current spot is observed featuring a size of ~25 nm. This current spot might originate from a single Ag-CF. Increasing the oxide thickness to values of 5 nm and 10 nm, a distinct increase of total area of conductive features is measured, potentially originating from more conductive material being deposited below the AgNC during electro-forming. These areas of enhanced conductivity are preferentially located at previous AgNC edge locations. Further increase of TiO_2 layer thickness to 15 nm results in large, solid areas of enhanced conductivity with no fine-structure observed anymore. This evolution of total conductive areas is investigated in more detail in Fig. 6.15 (b), where the integrated areas of current per particle are plotted as a function of oxide thickness. Apparently, an approximately linear correlation is obtained. This linear correlation might originate from more time needed for a complete CF to form for larger oxide thickness. When the oxide is thicker, ions have to travel a larger distance until they arrive at the oxide/p-Si interface, where they are reduced. For equal bias, this takes more time, where meanwhile, ions are also injected at other positions leading to additional Ag agglomeration.

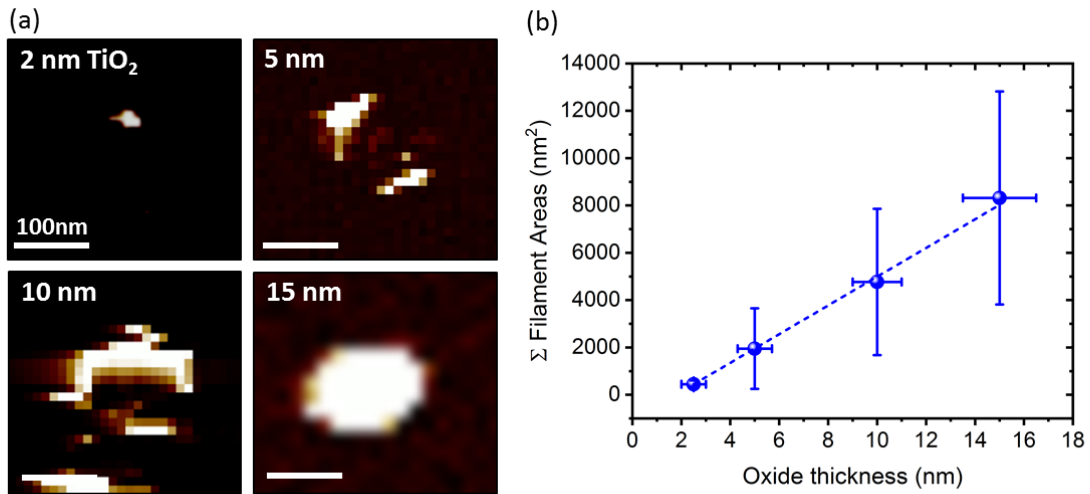

Figure 6.15 Evolution of local conductivity with increasing TiO_2 layer thickness. Current maps in (a) show areas below electro-formed AgNCs after delamination for oxide thicknesses of 2 nm, 5 nm, 10 nm and 15 nm. Apparently, with increasing oxide thickness, the total area of conductive features increases, until no fine-structure can be observed anymore in the case of 15 nm. This behavior is further investigated in (b), where integrated areas of local current per particle (obtained by particle analysis tool in *NanoScope Analysis* software) are plotted against oxide thickness. An approximately linear correlation is obtained, most likely resulting from more time needed for Ag-CFs to form in thicker oxide layers. When more time is needed, in total also more Ag is deposited below AgNCs, resulting in larger conductive areas.

Hence, due to preferential position of current spots at previous AgNC edge positions, we assign these spots to partly formed or complete conductive filaments (CFs). As the oxide thickness is slightly larger but still in a range of tunneling current potentially being measured between oxide surface and TiO_2/p-Si interface by CP-AFM ($\lesssim$5 nm), also only partly formed CFs may significantly enhance local conductivity. In detail, at positions where a significant amount of Ag-atoms is immobilized, but not completely bridging the gap between probe tip and p-Si, the tunneling barrier is thinner and therefore more current might flow. Therefore, also these spots might contribute to overall size of current areas.

6.6.2 Cross-sectional SEM studies

Ag-ion flow might preferentially happen at AgNC edges, as local electric field enhancement due to AgNC geometry leads to lowering of Ag-ion injection barrier and therefore enhanced probability of ion injection. This assumption is further verified by cross-sectional SEM studies. For this purpose, a larger TiO_2 layer thicknesses of 20 nm is used, making imaging in SEM more reliable. AgNCs on p-Si/20 nm TiO_2 are electro-formed and mechanically removed as described before. These AgNCs were assembled in array geometry (cf. sec. 6.2) to facilitate cube localization in SEM. Once these electro-formed particles are localized, they are cut into half by focused ion-beam milling (cf. sec. 4.5).

An SEM micrograph of a typical area including a few AgNCs cut by FIB under a stage tilt-

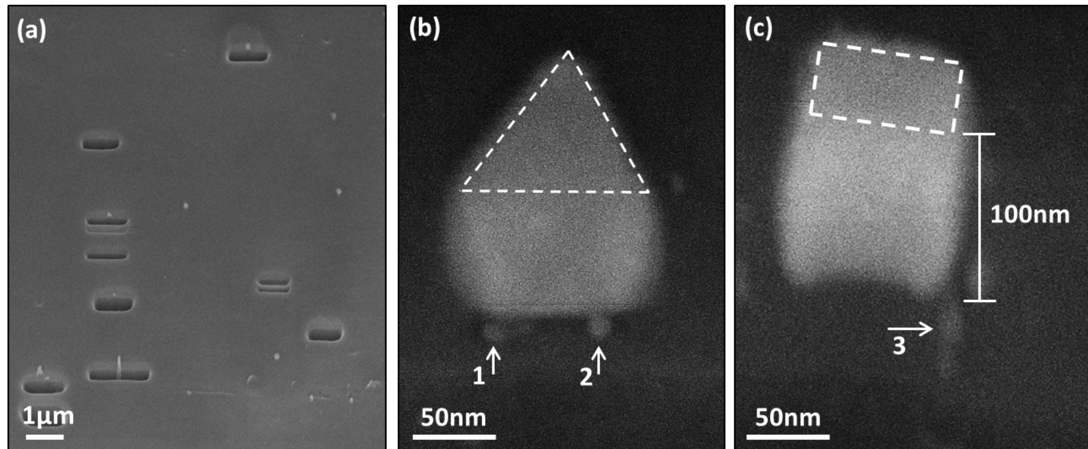

Figure 6.16 Cross-sectional SEM studies of Ag-CFs below AgNCs on p-Si/20 nmTiO_2 after electro-forming by CP-AFM. (a) Exemplary SEM image of an area containing AgNCs after FIB-cutting (stage tilt-angle 36°). (b) and (c) illustrate zoom-in images of respective AgNC cross-sections with white dashed lines indicating remaining AgNC top facets. White arrows indicate conductive material agglomeration below AgNC edges. These round bright features 1, 2 and 3 are assigned to contracted Ag-CFs characteristic for threshold switching.

angle of 36° is shown in Fig. 6.16 (a). As can be seen in more detail, precise cutting of such small particles is challenging, as some might be cut too much and some not enough. In total, 23 electro-formed AgNCs were investigated with three of them showing signs of material agglomeration below their edges. This might be due to random position of Ag agglomerates with respect to the bottom of AgNCs, making precise hitting of a respective position necessary for observation. Two exemplary AgNC cross-sections are shown Fig 6.16 (b) and (c), with white dashed lines indicating the remaining rest of AgNC top-facets. Distinct spherical featured below the edges and below the corner of particles are observed in (b) and (c), respectively, marked with white arrows 1, 2 and 3. Features 1 and 2 below left and right AgNC edges in (b) exhibit a diameter of ~12 nm, with feature no. 2 being in contact with the AgNC and no. 1 being slightly separated from the particle by a small gap of ~4 nm. Hence, these features might correspond to CFs with one of them having been complete for high bias and contracted for small bias to spherical islands due to Rayleigh instability [145, 152]. Feature no. 3 in (c) contains two round agglomerates in lateral direction, with the top one being slightly larger and also not in contact with the AgNC. These observations might constitute an additional proof for unstable Ag-CFs being the main mechanism behind threshold switching as described before in sec. 6.4.

6.6.3 Finite element simulations of the electric field distribution in TiO_2

For further investigation of inhomogeneity of the electric field inside the TiO_2 layer below AgNCs under the application of an external bias, finite element simulations using the static electric field solver in *Comsol* software were executed. The simulation setup includes the AgNC (100 nm × 100 nm) on top of the oxide layer (thickness: 20 nm, relative permittivity:

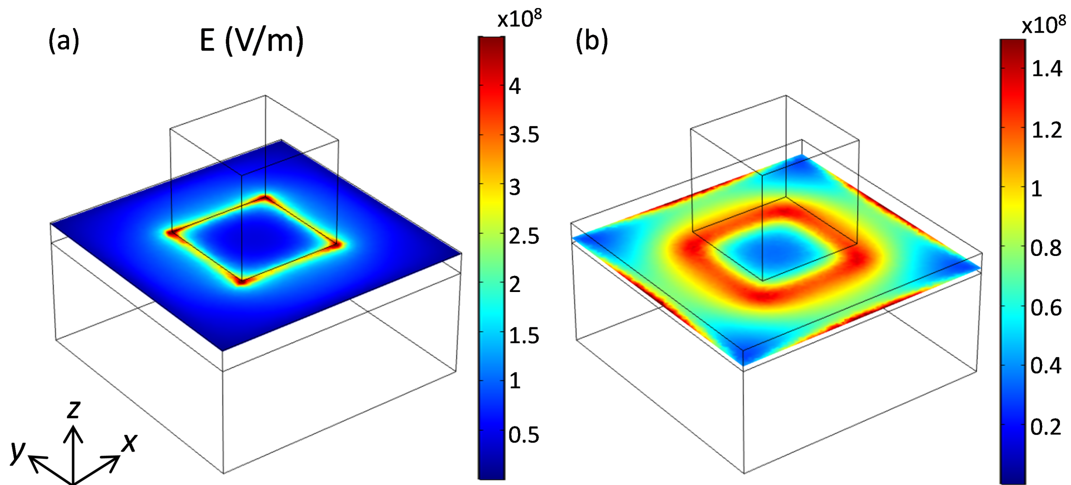

Figure 6.17 Finite elements simulation (*Comsol* software) of electric field distribution (a) at the AgNC/TiO_2 layer interface and (b) at the p-Si/oxide interface. At both interfaces, significant field enhancement at particle edges is obtained, with the inhomogeneity gradually decreasing towards the p-Si/oxide interface. As in CP-AFM experiments, the bias is applied to the Si-substrate (10 V), whereas the AgNC is at a fixed potential of 0 V.

ϵ_r(TiO_2)=80 [153–155]) and the p-Si substrate on the bottom (modeled as degenerately p-type Si). Similar to CP-AFM measurements, the potential was applied to the bottom of the Si layer (10 V), whereas the AgNC was kept at a fixed potential of 0 V. In addition, periodic boundary conditions were used. Resulting cross-sections in z-direction of the electric field distribution in units of V/m are shown in Fig. 6.17. Fig. 6.17 (a) illustrates the distribution at the AgNC/TiO_2 interface on the x-y-plane, revealing strong field enhancement at particle sides and edges (red to green colors on the color scale), whereas the surrounding oxide remains nearly field-free (blue color). At the oxide/Si interface, this local field-enhancement slightly decreases, but is still pronounced, as can be clearly seen in Fig. 6.17 (b). Hence, we conclude the volume of enhanced electric field below AgNC edges to potentially act as preferred ion channels, being in line with results obtained in current maps and cross-sectional SEM micrographs shown previously in Fig. 6.15 and 6.16.

6.6.4 Comparison with aluminum oxide layers

For deeper understanding of CF formation mechanism below AgNCs during electro-forming, additional experiments were executed replacing TiO_2 layers by aluminum oxide (Al_2O_3) thin films grown by ALD (cf. sec. 4.1.1) on highly p-type Si wafer pieces. Similar to experiments described previously, AgNCs on Al_2O_3 layers featuring a thickness of 2 nm to 10 nm were electro-formed by application of a forming voltage of up to 10 V. Subsequently, AgNCs were also removed by mechanical delamination and underlying oxide areas evaluated by CP-AFM applying a small read voltage of 2 V to 4 V. The resulting integrated conductive areas are plotted

as a function of oxide thickness together with values obtained for TiO_2 in Fig. 6.18 (a) as green and blue data points with error bars, respectively. Apparently, also an approximately linear correlation is obtained, featuring a nearly similar slope of linear fits shifted towards larger areas. This linear correlation is attributed to also more time needed for larger oxide thicknesses to form complete CFs in the case of Al_2O_3 and therefore more material being deposited in the oxide layer.

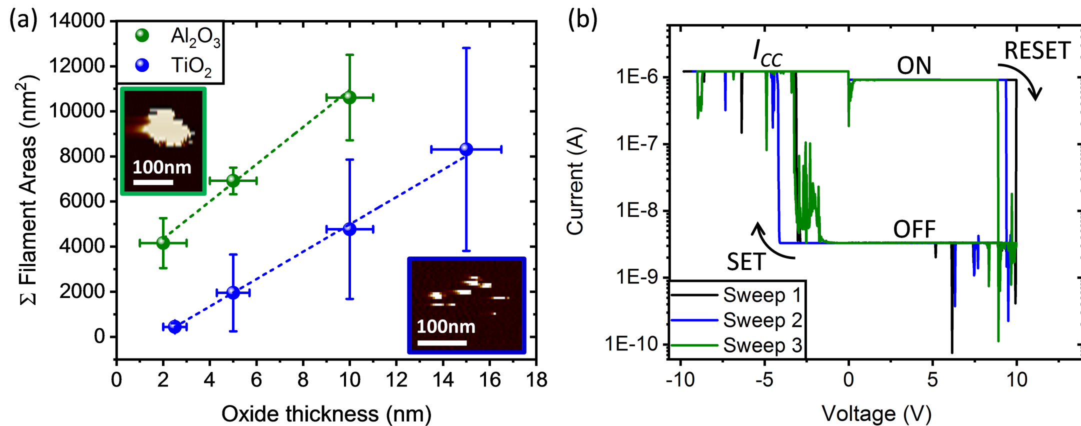

Figure 6.18 Evolution of integrated local conductivity areas per particle as a function of increasing oxide layer thickness. In both cases of TiO_2 (blue color) and ALD-grown Al_2O_3 (green color) layers, a linear correlation is obtained. However, current maps below previously electro-formed AgNCs on both oxides exhibit distinct differences. In the case of TiO_2, current spots are preferentially distributed at previous AgNC edge positions as shown in the current map in the inset with blue frame. By contrast, current maps below AgNCs on Al_2O_3 reveal solid spots of enhanced conductivity, also for small oxide thicknesses, as exemplary illustrated by the current map in the inset with green frame. This is a strong indication for stable CFs resulting in stable, non-volatile resistance switching as shown in (b), where the first three DC IV-sweeps of a AgNC on 3 nm are shown (I_{CC}: compliance current).

However, two main differences were observed:

- In contrast to AgNCs on TiO_2, where threshold switching was observed (cf. Fig. 6.8), AgNCs on Al_2O_3 featured non-volatile memory switching performing DC IV-sweeps via CP-AFM. In Fig. 6.18 (b), the first three DC IV-sweeps of a AgNC on 3 nm Al_2O_3 are exemplarily shown. Clearly, the resistance can be reliably switched between ON- and OFF states performing a SET step at negative voltage ($V_{SET}\approx-3.5$ V) and a RESET step at positive sample bias ($V_{RESET}\approx 9$ V). ON- and OFF-state currents are restricted by values of the compliance current $I_{CC} = 1\times10^{-6}$ A and the value of the noise level of the amplifier (3×10^{-9} A) of the CP-AFM setup, resulting in an ON/OFF-state ratio of ~330.

- In line with the different electrical behavior, also current maps of areas below AgNCs on Al_2O_3 show different geometry. In detail, CFs appear not to be distributed along particle edges, but reveal solid and dense geometry, as shown in the current map with green frame in Fig. 6.18 (a). This observation might originate from two possible reasons: i) better quality of ALD-grown Al_2O_3 layer being denser and exhibiting less defects in the oxide

that can act as ion channels, and ii) the electric field distribution inside the oxide is less inhomogeneous as compared to TiO_2 due to the smaller value of relative permittivity.

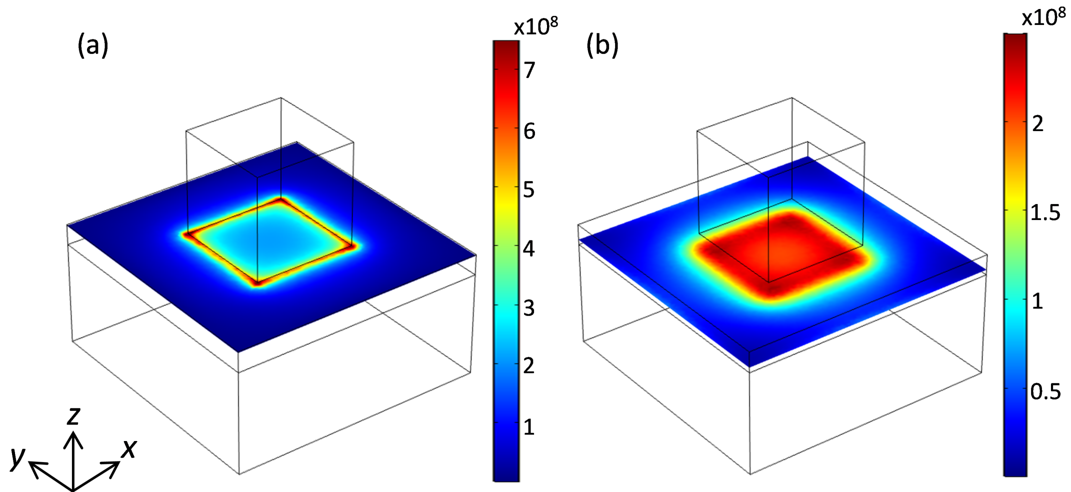

Figure 6.19 Finite elements simulation (*Comsol* software) of electric field distribution (a) at the AgNC/Al_2O_3 layer interface and (b) at the oxide/p-Si interface. Clearly, the inhomogeneity of the electric field at the AgNC/Al_2O_3 layer interface, i.e. the field enhancement at the AgNC edges, is smaller compared to TiO_2 (cf. fig. 6.17 (a)) and vanishes nearly completely at the oxide/p-Si interface.

However, these findings indicate stable Ag-CFs in Al_2O_3 resulting in non-volatile resistive switching in contrast to the behavior observed for TiO_2 layer. To further verify this assumption, additional finite element simulations were performed using the same simulation setup as described in sec. 6.6.3, but replacing the value of the relative permittivity by $\epsilon_r(Al_2O_3)=11$ [154]. Apparently, as can be seen in Fig. 6.19 (a), at the AgNC/Al_2O_3 interface, also pronounced inhomogeneity of electric field at particle edges is obtained. However, the field enhancement relative to the AgNC center is less pronounced as compared to the case of TiO_2 in Fig. 6.17 (a). In addition, as shown in Fig. 6.19 (b), at the AgNC/Si interface, the field distribution below the particle is nearly homogeneous, which is in marked contrast to simulation results obtained for TiO_2 as shwon in Fig. 6.17 (b). Clearly, this different field distribution originates from the relative permittivity of Al_2O_3 ($\approx$11) being much smaller than the value of TiO_2 ($\approx$80) and therefore the field drops much faster in Al_2O_3. This in turn might lead to different CF geometry, as the field distribution critically influences ion injection position at the AgNC/oxide interface and ion transport direction inside the oxide layer, potentially leading to more solid and dense, and therefore more stable CFs in Al_2O_3. Another contribution of CF instability and shape in TiO_2 might originate from mobile oxygen ions, known to potentially causing reduction of Ag-ions during CF formation.

6.6.5 Kinetic Monte-Carlo simulations with electric field distribution

In order to further investigate the influence of local electric field inhomogeneity on CF growth, the kMC model described in section 2.6 was expanded by implementing a spatially dependent electric field component. This was realized by implementing a Poisson-solver into the kMC model and by updating the electric field at each lattice point after each simulation step. This way, the local electric field distribution inside the oxide layer below the AgNC was modulated, leading to modulation of the injection barrier height for ions at the Ag/TiO_2 interface. In addition, locally enhanced field at positions where Ag-ions have already been reduced and immobilized again at the p-Si/TiO_2 interface influence ion migration as well now, leading to preferred ion trajectories towards these positions and therefore more guided CF growth. This can be observed in more detail in Fig. 6.20 (a) and (b), where a resulting CF structure is shown in side- and top-view, respectively, with the scale bar ranging from yellow to red indicating CF formation time, i.e., the time from the first injection event until a single CF was grown from the PE (p-Si on the bottom) to the AE (AgNC on the top). Each dot shown in the simulation area therefore represents an immobilized Ag-cluster. Please note that for simulation time reasons, only an area of $20\,\text{nm} \times 20\,\text{nm}$ was simulated (as indicated by the black box), as the electric field had to be updated for each simulation step. The simulation was executed for three different TiO_2 layer thicknesses of 5 nm, 10 nm and 15 nm. The results shown here were obtained by simulating a volume of $20\,\text{nm} \times 20\,\text{nm} \times 10\,\text{nm}$. Apparently, taking the locally enhanced electric field at AgNC edges into account results in a clear preference of ion injection at these positions, with ion clusters preferentially occurring at AgNC sides (marked by blue colored circles). Moreover, formation times are also in a range of a few 100 ms. These simulation results are in good agreement comparing current maps obtained by ex-situ AFM for 10 nm TiO_2 layers, such as shown in Fig. 6.14 (c), where also preferred material deposition at AgNC sides was observed. To directly compare results obtained by ex-situ CP-AFM and kMC, i.e., to compare the amount of Ag deposited in the oxide as a function of oxide thickness until CF completion, two-dimensional cross-sections such as in Fig. 6.20 (b) were evaluated for TiO_2 layer thicknesses of 5 nm, 10 nm and 15 nm. In detail, areas of clusters larger than $2\,\text{nm} \times 2\,\text{nm}$, such as indicated by features highlighted by blue circles, were summed up and than scaled up to the full $100\,\text{nm} \times 100\,\text{nm}$-sized AgNC/oxide interface for comparison with CP-AFM results. Fig. 6.20 (c) shows the resulting integrated CF area per AgNC as a function of oxide thickness for Al_2O_3 obtained by CP-AFM (green dots), for TiO_2 obtained by CP-AFM (blue dots) and for TiO_2 obtained by kMC simulations (black dots), with dashed lines in according colors showing linear fits to the data. Obviously, integrated kMC areas appear to be smaller compared to areas obtained by CP-AFM. However, the data is still in a range of error bars and two major trends are confirmed: i) with increasing oxide thickness, integrated CF areas also increase in kMC simulations and ii) this increase appears to be linear. We assign the offset of kMC data to imperfections of simulations and to the fact that three-dimensional results of kMC simulations are hard to compare to 2D data obtained by CP-AFM. Moreover, experimental areas might

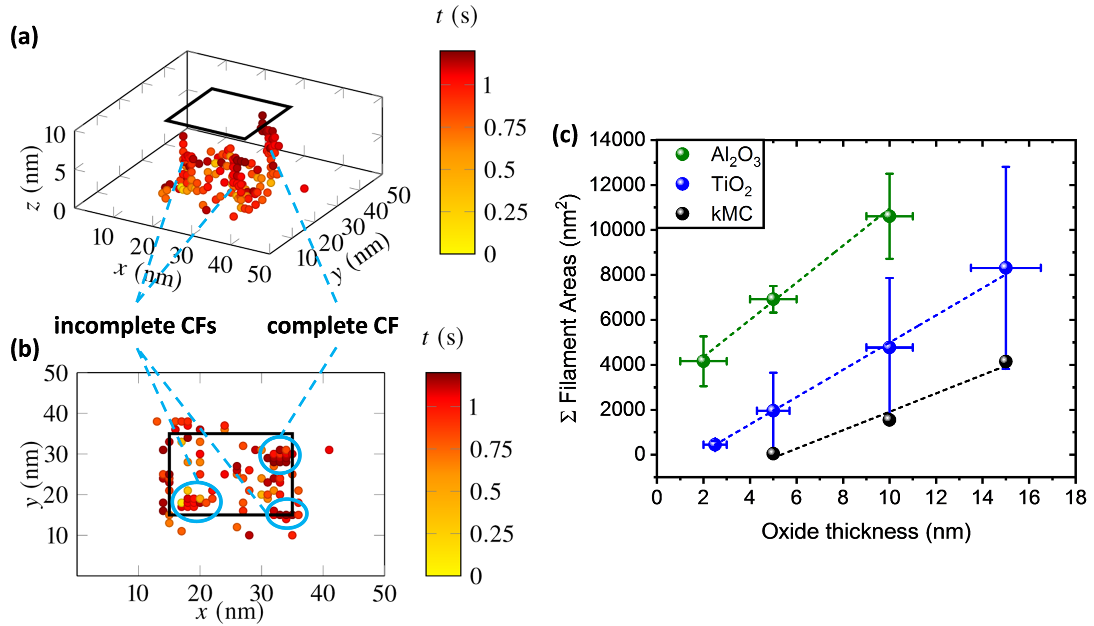

Figure 6.20 Kinetic Monte-Carlo simulations of conductive filament growth including local electric field distribution. (a) and (b) show a resulting filament structure in side- and top-view, respectively. Each dot represents a Ag cluster with the color scale ranging from yellow to red indicating filament formation time. A simulation volume of 20 nm × 20 nm × 10 nm was used. Apparently, Ag-cluster formation preferentially at AgNC edges is obtained. (c) compares integrated filament areas per AgNC as a function of oxide layer thickness obtained by ex-situ CP-AFM (Al_2O_3 and TiO_2 in green and blue color) and kMC simulations (black), with dashed lines representing linear fits to the data. Simulated values are smaller compared to experimental data, however, they are within error bars and a linear increase of CF area with increasing oxide thickness is obtained as well.

appear to be slightly larger due to restrictions in spatial resolution. Especially in the direction of trace and re-trace, current spots commonly appear to be larger already for moderate scan-rates and biases.

Hence, these findings highlight the importance of AE geometry and oxide thickness and composition for small devices in the range of <100 nm, as these quantities might have a major influence on filament growth dynamics and stability and therefore ECM device behavior. In particular, these ex-situ studies showed that for rectangular AEs and oxides with a high value of the dielectric permittivity ϵ_r, CF growth tends to occur at several positions at AE edges and CFs tend to be rather unstable. By contrary, oxides with low ϵ_r yield a more homogeneous electric field distribution below the AE and therefore less influence of AE geometry on CF growth position and stability. These findings need to be taken into account for possible future down-scaling of NP-based memristive devices.

6.7 Summary

In summary, we have demonstrated the directed, high-yield assembly of functionalized AgNCs on target sites on a planar TiO_2 layer which was pre-patterned with a complementary SAM only. The formed, regular array of nanocubes showed pronounced threshold-switching characteristics for the individual junctions which can be assigned to Ag ion migration and conductive filament formation and rupture processes. This assumption was supported by kinetic Monte-Carlo simulations, finite element simulations and ex-situ CP-AFM and cross-sectional SEM studies. In particular, these studied indicated pronounced metal deposition in TiO_2 layers at AgNC edges due to electric field enhancement at these positions. Moreover, replacing the TiO_2 electrolyte by Al_2O_3 layers grown by atomic layer deposition yielded non-volatile memristive switching along with different CF geometries.
Our approach of self-arranging TS junctions is exclusively based on the chemical reaction between two complementary surfaces and may be extended to the combination of more and different material species, including, e.g., semiconductors and into the third dimension [33, 116]. Further down-scaling of the system towards the sub-10 nm regime may well be possible, and more efficient reaction schemes for self-assembly, eventually involving only two molecular species, can be envisaged. For practical device applications, further studies will be directed towards fixed solid-state top contact schemes to replace the current AFM tip contact. This way, we anticipate both, device performance in terms of threshold voltage distribution and device stability, to improve significantly.

7 Memristive switching in self-assembled AgNC-SiNP dimers

7.1 Introduction

In this chapter, the selective formation of heterogeneous nanoparticle (NP) agglomerates and their memristive switching properties is reported. Following surfactant-mediated self-assembly in suspension, agglomerates from silver nanocubes (AgNCs) and spherical silicon nanoparticles (SiNPs) are prepared in a bottom-up approach. Dimers comprising one AgNC and one SiNP are electrically contacted and pronounced bi-polar memristive switching is demonstrated. The formed nanoscale memristor junctions feature narrow distributions in particular of the SET voltage, ON/OFF-resistance ratios in excess of three orders of magnitude and good retention properties. Ex-situ scanning electron microscopy studies directly support a switching model based on Ag conductive filament formation in the poly-crystalline SiNP. We propose our self-assembled NP-memristors as building-blocks for the bottom-up construction of future 3D memristive networks. The following chapter is closely related to the work presented in [156] © 2020 American Chemical Society.

7.2 Self-assembly of AgNC-SiNP agglomerates

Suspensions comprising Ag nanocubes (of side length ~100 nm) and spherical, polycrystalline Si nanoparticles (diameter ~60 nm) were investigated first with respect to their ability to form heterogeneous NP-agglomerates, i.e., those comprising both nanoparticle types. Nanoparticle colloidal self-assembly depends largely on a variety of experimental factors, including NP size, concentration, temperature, and in particular, the surface properties or coatings of the NPs, governing their mutual interaction forces [15, 16]. In this context, adding specific surfactants to the suspension may strongly determine the outcome of the assembly experiment, regarding size, shape and number of formed aggregates. Our starting NPs featured different surface termination, as indicated in Fig. 7.1 (a): Ag nanocubes were coated by a polyvinylpyrrolidone shell owing to the preparation process (cf. sec. 3.3), and the SiNPs were chemically synthesized and decyl-terminated (cf. sec. 3.4), following a dedicated surface functionalization procedure [64]. Such alkyl-surface termination is a mandatory requirement for dispersing the NPs in

liquid suspension; uncoated NPs are prone to large-scale agglomeration, which would conflict the targeted, controlled heterogeneous self-assembly.

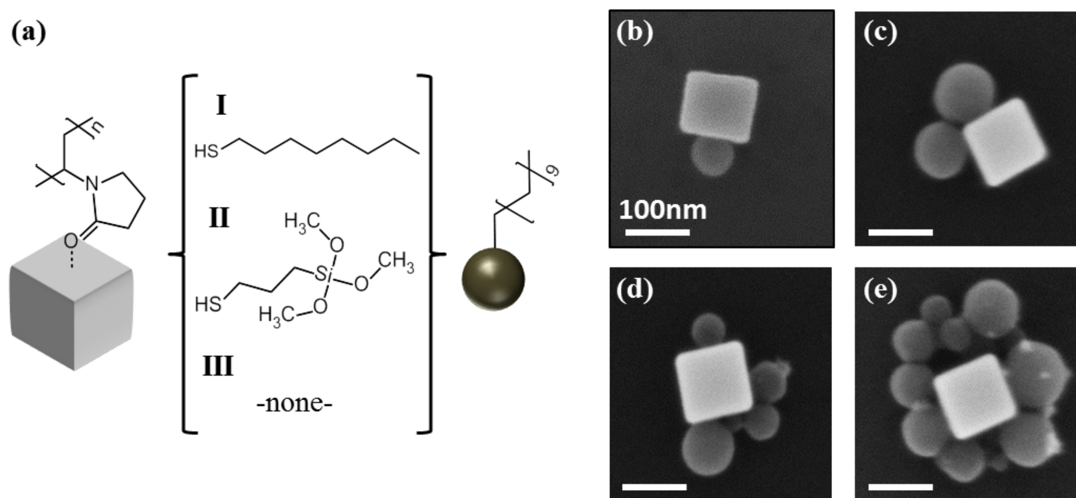

Figure 7.1 (a) Schematic representation of nanoparticles and surfactants (I, II, III) used for self-assembly experiments. (b) to (e) Exemplary SEM images of typical nanoparticle agglomerates involving one AgNC, such as dimers (b), trimers (c) and higher order oligomers (d, e). Reprinted with permission from [156] © 2020 American Chemical Society.

To initiate and control the aggregation process we tested three different reaction schemes involving alternative surfactants. Ag-nanocube (AgNC)/ Si-nanoparticle (SiNP) agglomerates were assembled in solution following respective reaction schemes as illustrated in Fig. 7.1 (a). In the first assembly process (I), 1 mL of dimethylformamide (DMF), 10 µL of as-obtained, polyvinylpyrrolidone (PVP)-functionalized AgNCs (1 mg/mL in EtOH), 10 µL of decyl-functionalized SiNPs (1 mg/mL in toluene), 10 µL of 1-octanethiol were added into a centrifugation vial. After sonication for 15 min, the vial was mounted onto a vortex shaker and agitated at 2000 rpm for 1 h. Subsequently, the dispersion was allowed to react for another 4 h at room temperature and then stored in a refrigerator at a constant temperature of 8 °C. The second self-assembly process is executed following the same procedure, but replacing the 1-octanethiol surfactant by mercaptopropyltrimethoxysilane (MPTMS), as shown in Fig. 7.1 (a) II and adding 10 µL of DI water. Additionally, as a reference experiment, the same sequence is executed, omitting any additional surfactant, as can be seen in Fig. 7.1 (a) III. Samples for aggregate counting in SEM were prepared by drop-casting an amount of 50 µL of the NP-dispersion after self-assembly on a clean, 5 mm × 5 mm sized Si substrate and allowing it to dry on a hotplate at a moderate temperature of 60 °C.

Following self-assembly, the efficiency of aggregate formation depending on surfactant was then determined by drop-casting the NP-agglomerates on a planar silicon substrate and counting the formed assemblies of various size, composition and complexity using SEM. While a large variety of (also macroscopic) aggregates generally formed, as can be seen in the overview-SEM image in Fig. 7.2, we here focused on those consisting of single AgNCs whose side-facets were

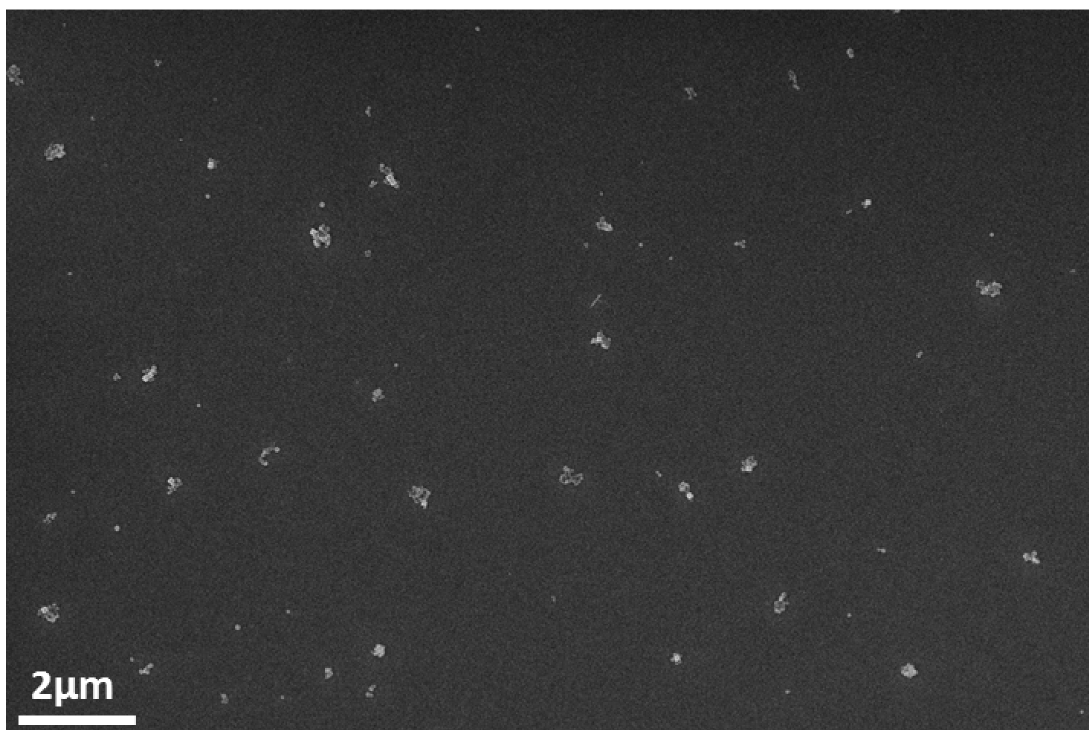

Figure 7.2 SEM overview image used to count nanoparticle agglomerate sizes for statistical analysis of self-assembly processes. Targeted, single AgNCs whose side-facets are being covered by either none or by SiNPs of various quantity have been taken into account, whereas larger agglomerates including more than one AgNC have been excluded. Reprinted with permission from [156] © 2020 American Chemical Society.

specifically covered by one or more SiNPs. These included dimers (one AgNC side covered by one SiNP, cf. Fig. 7.1 (b)), trimers and higher order oligomers, respectively, as illustrated in Fig. 7.1 (c) to (e). Overall, a total amount of 2068 NP-structures on at least three different samples for each self-assembly process was counted by SEM. The fraction of agglomerates not covered by the types shown in Fig. 7.1 (b) to (d), i.e., those comprising more than one AgNC or larger numbers of linked SiNPs, was estimated to be ~25 %. We observed significant differences in the yield and distribution of heterogeneous NP aggregate formation, depending on the actual surfactant (I, II, III) used during the assembly process. The results are compared with the help of histograms counting the number of Ag nanocube facets covered by Si NPs. By adding 1-octanethiol (c.f. Fig. 7.1 (a) I) to the suspension of NPs, a pronounced majority of agglomerates formed with three AgNC facets being covered by SiNPs (see Fig. 7.3 (a)). On average, 2.9±0.04 AgNC sides are covered by a SiNP, so the preferred agglomerate geometry was quadromers. Adding instead mercaptopropyltrimethoxysilane (MPTMS, c.f. Fig. 7.1 (a) II), the distribution has a larger weight at a somewhat lower value of 2.2±0.1 covered sides, as can be seen in the histogram of Fig. 7.3 (b). Hence, in this case, the preferred agglomerate geometry is trimers. By contrast, reference experiments with no additional surfactant, i.e., using only the as-obtained AgNCs, which are covered by polyvinylpyrrolidone (PVP, c.f. Fig.

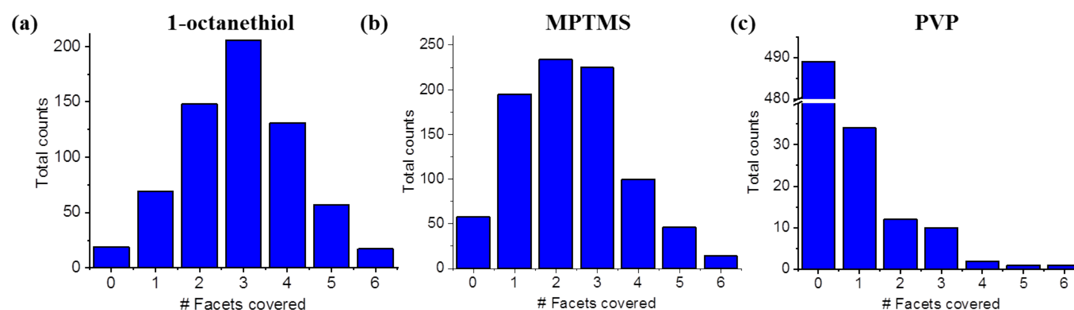

Figure 7.3 Distribution (counts) of the self-assembly yield for different surfactants showing the number of AgNC-side facets being covered by a SiNP (cf. Fig. 7.1 (a)). (a) Reactions with 1-octanethiol and (b) MPTMS clearly lead to selective self-assembly, whereas experiments with as-obtained, PVP-covered AgNCs (c) do not feature significant agglomerate formation. Note the ordinate axis break in (c). Reprinted with permission from [156] © 2020 American Chemical Society.

7.1 (a) III), did not yield significant NP-agglomerate formation as shown in the histogram in Fig. 7.3 (c). A clear majority of AgNCs was found, which had not accumulated any SiNPs on their surface during the process, and therefore mainly single AgNCs were counted. The remaining smaller total number of agglomerates can be attributed to mostly unspecific physisorption (van der Waals forces). This finding points towards different self-assembly mechanisms using 1-octanethiol or MPTMS: Specifically, by adding 1-octanethiol, the weak Ag-O bound of PVP molecules in the unordered PVP shell close to the AgNC surface is replaced by the stronger Ag-S bond [134]. Hence, the AgNC surface is rendered to be strongly hydrophobic due to ordered, non-polar alkyl chains covering the surface. Given the fact that SiNPs are dodecyl-terminated and that the reaction takes place in the highly polar solvent dimethylformamide (DMF), hydrophobic interactions are supposed to strongly favor (heterogeneous) agglomerate formation due to surface free energy minimization of NP surfaces [157].
This is supposed to result in a self-assembly process with no covalent bond formation between two adjacent NPs. However, using MPTMS, both terminal groups of the molecule can efficiently bind to either one of the NP species, i.e., the thiol to the surface of the AgNC and the trimethoxysilane to the SiNP provided that latter comprises surface oxides [45, 158]. Typically indeed, the dodecyl functionalization on SiNPs may not perfectly seal the silicon surface but rather comprise locally exposed sites prone to oxidation [105]. Indeed, TEM analysis shown in Fig. 7.4 and in Fig. 3.3 may support an existing, though very thin (<1 nm) surface oxide layer on the outer rim of the SiNPs. These locally oxidized surface spots would then serve as tethering points for the silanes. Therefore, covalent binding between adjacent NPs is possibly leading to a self-assembly process with higher binding energy. Comparing respective agglomerate size distributions, the self-assembly process based on hydrophobic interaction only appears to be slightly more efficient in terms of finding local energy minima of agglomerate formation [157].

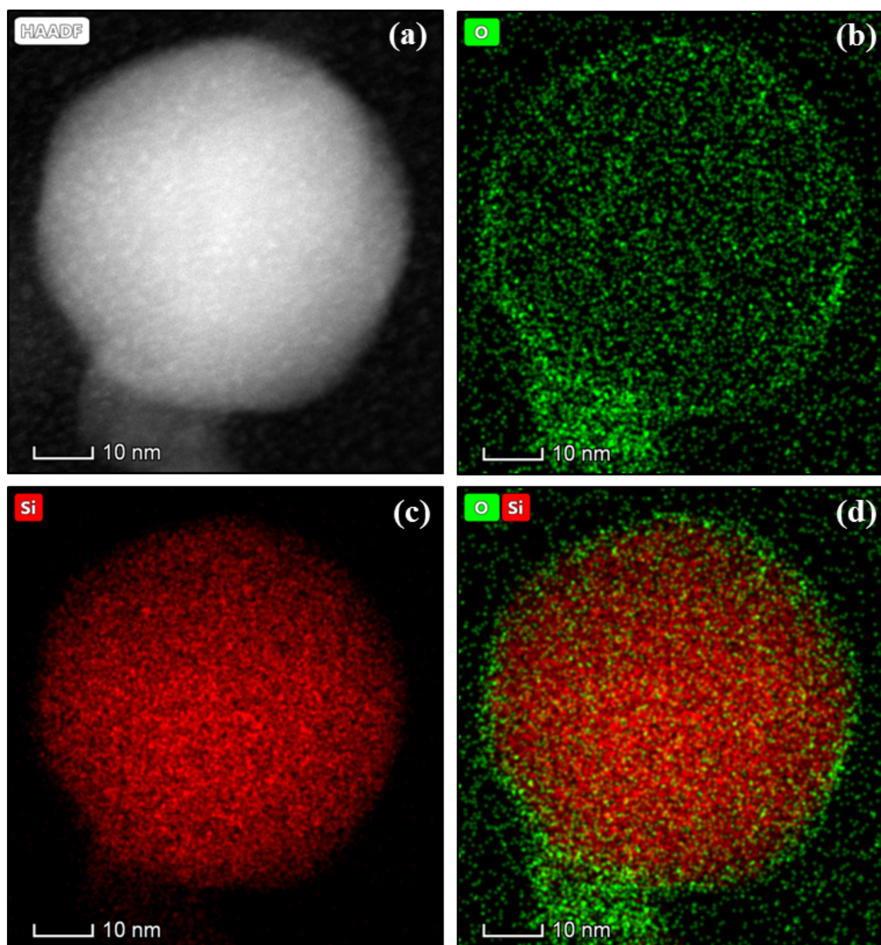

Figure 7.4 (a) HAADF-STEM image of a typical SiNP and the respective EDX maps of (b) the oxygen Kα intensity distribution in green, (c) the Si Kα intensity distribution in red and (d) an overlay of both contributions. Apparently, the O-signal is larger on the SiNP surface, indicative for a thin oxide layer. Reprinted with permission from [156] © 2020 American Chemical Society.

7.3 Electrical characterization of AgNC-SiNP dimers on interdigitated electrodes

To form electrical contacts to NP-dimers, such as illustrated in Fig. 7.5 (a), an interdigitated electrode (IDE) platform was used [116]. These IDEs were fabricated on highly p-type Si wafer pieces covered by a thermal oxide layer of 50 nm thickness by electron beam lithography, metal evaporation and lift-off. An IDE structure consists of two rows of 30 opposing Ti/Au strip lines (5 nm/ 30 nm) of 40 µm length and 200 nm width, both separately connected to contact pads of 50 µm × 50 µm size for probe station measurements, as schematically illustrated in Fig. 7.5 (b). The separation between two strip lines is chosen to be 150 nm to account for targeted NP-agglomerate size, such that a single AgNC cannot bridge the gap and therefore shortcut the device. To realize solid-state contacts to NP-agglomerates, an amount of 50 µL of NP suspension after self-assembly was drop-casted onto IDEs and the sample was subsequently

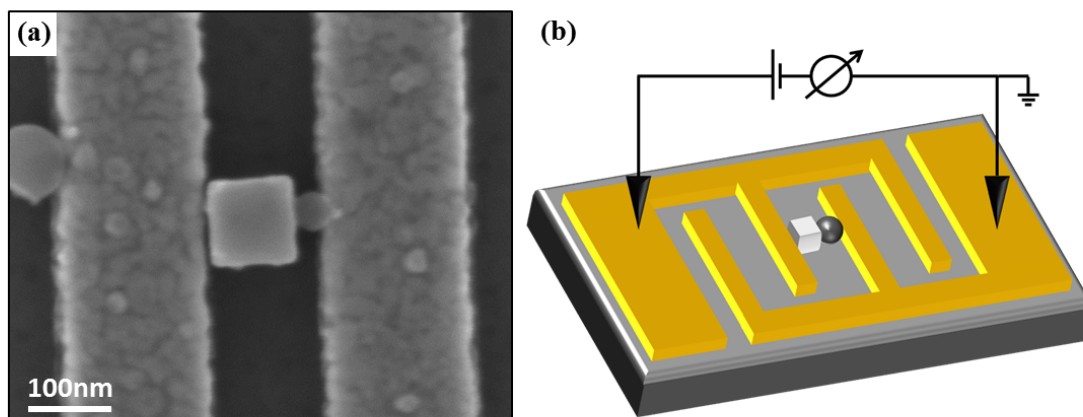

Figure 7.5 (a) SEM image of a typical AgNC-SiNP-dimer being successfully contacted by two opposing Au strip lines of an IDE device. This way, a MIM-structure is assembled, which can be operated as an electrochemical metallization cell. (b) Schematic illustration of an IDE device with embedded single AgNC-SiNP-dimer, contacted by two probes for IV measurements in a probe station. Reprinted with permission from [156] © 2020 American Chemical Society.

investigated by SEM. This process was repeated until a single NP-dimer was bridging two Au lines. In the ideal case, two interdigitated Au lines would contact the AgNC on the one side and the SiNP on the other side. In this configuration, we anticipate the AgNC to act as active electrode (AE), the poly-crystalline SiNP as solid electrolyte and the Au line connecting the SiNP as passive electrode (PE). This way, a heterogeneous NP-memristor can be successfully fabricated, similar to electrochemical metallization cells.

Fig. 7.6 (a)shows typical DC current-voltage (IV) curves of such a formed NP-memristor device on a semi-logarithmic scale. At first, the device is initialized by carrying out a forming step, as shown by the black curve. When initially a small positive bias is applied to the AgNC, the system does practically not conduct any current: only signals in the range of the resolution limit of the setup are detected (~0.7 pA). At a characteristic forming voltage of $V_{FORM.}$ ~4 V (arrow labeled 'FORM.'), the current rapidly increases until the pre-set compliance current I_{CC} of 1×10^{-6} A is reached. This compliance current is set to prevent the device from irreversible hard breakdown damage. Sweeping back to small positive and then negative voltages, the system features nearly linear (Ohmic) conduction, until a second transition of resistance occurs at high enough negative bias of V_{RESET} ~−1 V (arrow 'RESET'). At this point, the system is reset again. Hence, executing a second sweep (green curve), the device starts in its initial high resistance state (HRS) for small positive bias. Sweeping to higher positive voltages, the current now exponentially increases until a characteristic SET voltage V_{SET} ~3 V is reached (arrow 'SET'); this is a lower value compared to $V_{FORM.}$. At this value, the system undergoes a transition to a low resistance state (LRS) with the current again abruptly increasing to the value of I_{CC}. Subsequently, sweeping back again to small positive and then negative voltages, the system again shows nearly Ohmic conduction until V_{RESET} is reached, where the device undergoes a transition to the HRS and is therefore reset again. Hence, the resistance of the NP-memristor

can be efficiently switched between the two disparate conductance states in a hysteretic manner, by applying certain positive and negative programming voltages. Subsequently performing multiple IV sweeps, as indicated by the blue and red curves showing exemplarily the 10th and 25th sweep, respectively, the NP-memristor only shows small relative variations in HRS and LRS conductance. This specific IV characteristic featuring sharp transitions between two distinct resistance states is commonly observed in valence change memories (VCMs) and electrochemical metallization cells (EMCs). Fig. 7.6 (b) shows the IV data of all measured

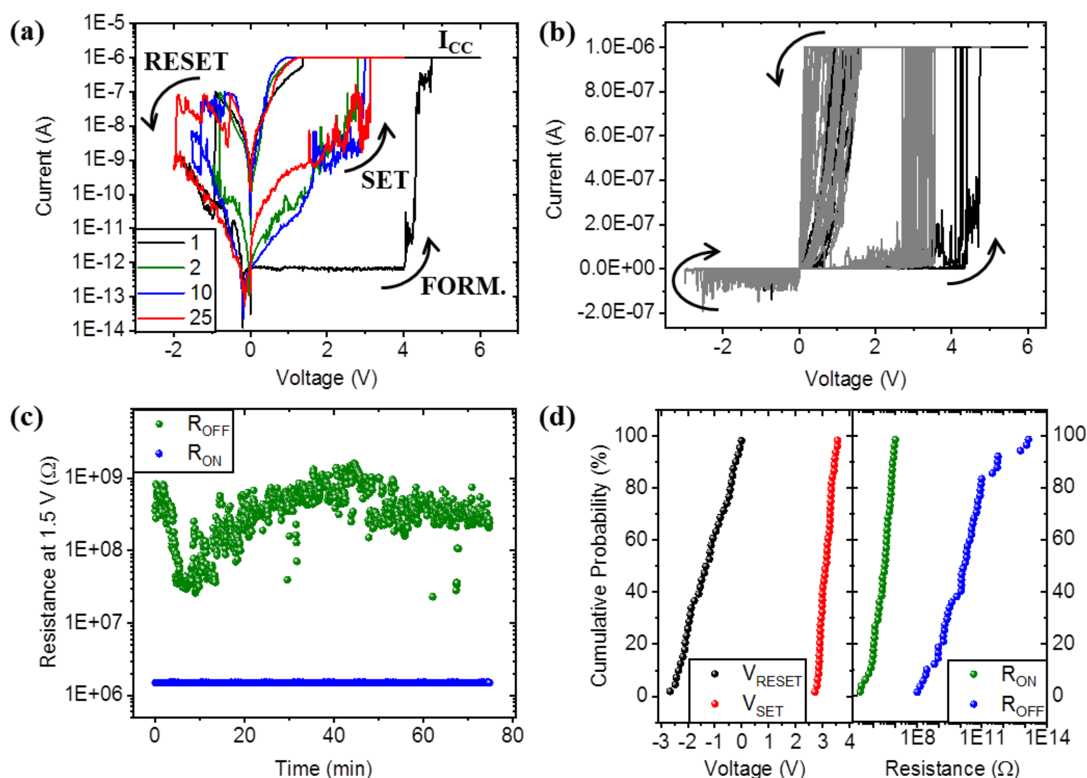

Figure 7.6 (a) DC IV-sweeps of a typical NP-dimer device on a semi-log scale featuring bipolar memristive switching. The first (forming) step in black, as well as the following second, 10th and 25th sweeps are shown in green, blue and red color, respectively. Black curved arrows indicate the sweep direction. I_{CC}: compliance current. (b) Summary of 113 IV-traces from all six measured devices in grey and forming curves in black on a linear scale showing small device-to-device variations. (c) Resistance of ON and OFF states of a typical device at a read voltage of $V_{SET}/2$ = 1.5 V as a function of time, revealing stable retention. Note that R_{ON} remains stable, as limited by I_{CC}. (d) Cumulative probabilities of V_{SET} and V_{RESET} in red and black color and of zero bias resistances of ON and OFF states in green and blue color, respectively, of all measured devices. Reprinted with permission from [156] © 2020 American Chemical Society.

devices on a linear scale with forming steps in black and all following measurements in gray. Black arrows indicate the sweep direction. In total, six different samples were characterized and an overall amount of 113 IV sweeps was recorded. The system shows good retention properties, as can be seen in Fig. 7.6 (c), showing ON and OFF state resistances in green and blue, respectively, measured for over 1 h at a read voltage of $V_{SET}/2$. Apparently, during

the first ten minutes, the OFF-state resistance R_{OFF} (green dots) is slightly dropping until a minimum is reached. Subsequently, roughly between ten and 40 min, R_{OFF} reaches its initial value again and stays stable for longer times, except for a view outliers. The ON-state resistance R_{ON} (blue dots) has a stable value of 1.5 MΩ, as the current is limited by the value of the compliance current at a read voltage V_{READ} of 1.5 V, as can be seen in Fig. 7.6 (a). Nevertheless, it is important to note that the current in ON-state did never drop below I_{CC}. Hence, a stable OFF/ON-state ratio of at least $\sim 10^3$ can be extracted. Fig. 7.6 (d) depicts the cumulative probability functions of V_{SET} and V_{RESET} in red and black color as well as zero bias resistances R_{ON} and R_{OFF} in green and blue color, respectively. Voltages are directly extracted from the data shown in Fig. 7.6 (b), whereas resistances are obtained taking the inverse values of slopes of linear fits of the IV data in the low-voltage regime between 0 and 0.1 V. Apparently, a remarkably narrow distribution of V_{SET} with mean value and standard deviation of $\overline{V_{SET}}$ =(3.10 ± 0.23) V is observed. Corresponding values for R_{ON}, V_{RESET} and R_{OFF} are $\overline{R_{ON}}$ =(3.7 ± 2.7) MΩ, $\overline{V_{RESET}}$ =(−1.30 ± 0.79) V and $\overline{R_{OFF}}$ =(0.78 ± 2.90) TΩ, respectively. The forming voltage has a mean value of $\overline{V_{FORM.}}$ =(4.3 ± 0.2) V>$\overline{V_{SET}}$. Our extracted values are in line with comparable studies on junctions comprising, i.e., Ag/aSi/p-Si, Ag/a-Si/poly-Si, Cu/a-Si/n$^+$Si, Cu/p-Si/n$^+$Si and Cu/aSi/Pt [159–162].

7.4 Model for resistance switching

After electrical characterization, samples exhibiting memristive switching were investigated again in close detail by SEM to gain more information about the switching mechanism, i.e., to eventually discriminate between VCM- or EMC-type origin. In particular, SiNPs after operation were investigated to look for possible structural changes such as deformation or additional material deposition. Indeed, cone-shaped, bright features were observed inside SiNPs, as highlighted by white arrows in Figs. 7.7 (a) and (b). These elongated, bright structures have the length of the respective SiNP (~54 nm) and a thickness of ~7 nm to 10 nm. Moreover, these features extend in the direction of the previously applied electric field, bridging the shortest distance between the AgNC and the opposing Au contact. This is a strong indication for metallic material being deposited inside the SiNP, as these structures appear to be brighter (emit more secondary electrons) compared to the rest of the poly-crystalline SiNP. Hence, Ag ion migration from the AgNC through the SiNP towards the Au contact is likely the most probable origin for the formation of these features, which eventually form conductive filaments (CF) connecting both metal electrodes [145, 152]. CF formation at the outer surface of the SiNP, i.e., in its oxide shell can likely be discarded, as confirmed by high-resolution transmission electron microscopy (HR-TEM and HAADF-TEM) which showed only very little oxidation (cf. Figs. 3.3 and 7.4). Further, we conducted reference experiments with AgNCs being connected to both Au electrodes and with AgNCs connected to only one Au electrode, without any SiNP, as can be seen in Figs. 7.8 (b) and (d), respectively. No stable memristive switching could be

observed in both cases, as apparent from the respective IV-curves in Figs. 7.8 (a) and (c). In the case of a AgNC being connected to both electrodes, random switching was observed for the first few cycles (black and red colors) for small voltages until irreversible breakdown occurred (blue color). In the case of a AgNC being connected to only one of the Au contacts, current in the range of the noise level was detected up to a voltage of 15 V. Hence CF formation through the supporting silicon oxide could be excluded.

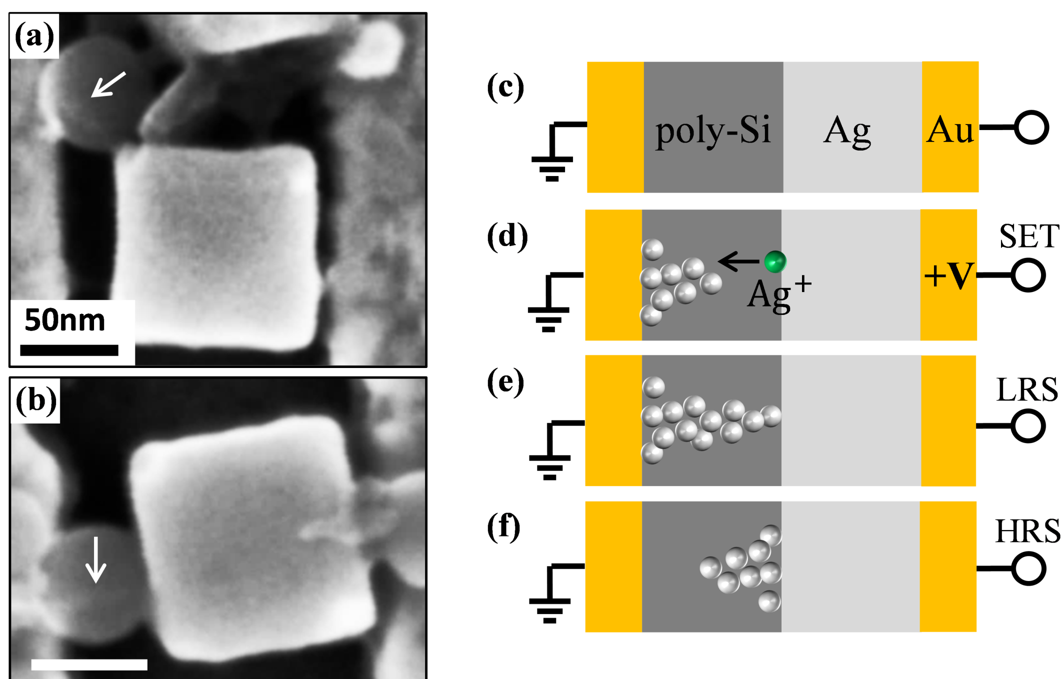

Figure 7.7 (a) SEM images of NP-dimers after electrical operation. Bright, cone-shaped features inside the SiNP can be identified (white arrows) pointing from the AgNCs towards the Au lines, being attributed to a Ag conductive filaments. (c)-(f) Model of Ag-ion migration in the SiNP, showing a schematic cross-section of the device before operation (c), during the SET process (d), in the LRS (e) and in the HRS (f). Adapted with permission from [156] © 2020 American Chemical Society.

A schematic illustration of the proposed switching mechanism is shown in Fig. 7.7 (c) to (f), with Fig. 7.7 (c) depicting a cross-section of the NP-memristor device before electrical operation with the two Au lines contacting the AgNC and the poly-crystalline SiNP from both sides. When a positive potential is applied to the AgNC (active electrode AE), Ag atoms are oxidized at the NP interface (green dot) and migrate as cations in the direction of the electric field through the poly-Si electrolyte towards the Au contact (passive electrode PE). As soon as a Ag ion reaches the PE, it is reduced and therefore immobilized again (silver dots). This accumulation of material leads to spatially enhanced electric field and therefore, further ion migration towards this region is preferred. As a consequence, Ag clusters accumulate at the position of previously immobilized Ag atoms, and a CF grows from the PE towards the AE. As soon as the CF reaches the AE, both contacts are connected, and the device is SET to the LRS (cf. Fig. 7.7 (d)). As illustrated in Fig. 7.7 (e), current can flow through the SiNP and

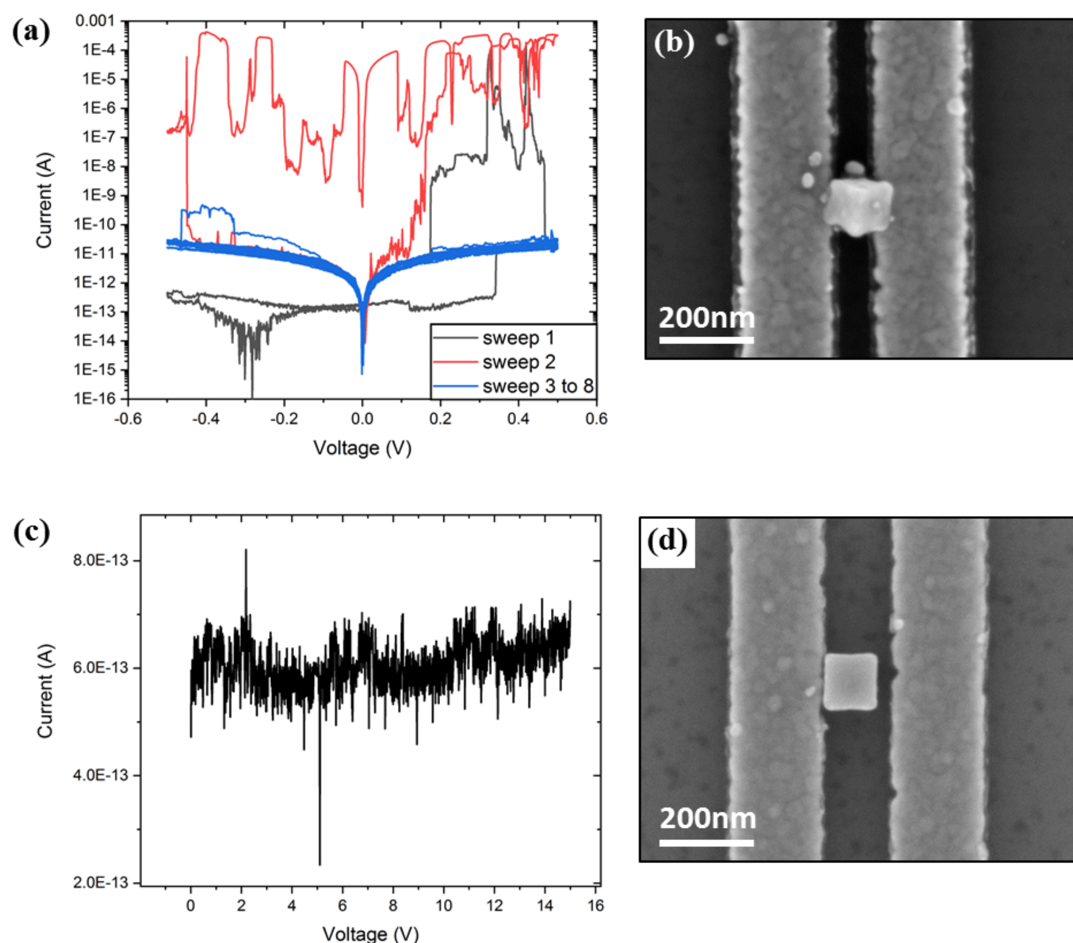

Figure 7.8 (a) IV-sweeps of the AgNC shown in the SEM image in (b) being directly contacted by both Au lines (distance 80 nm), showing random and unstable switching behavior and irreversible breakdown. (c) Represents the IV data of the AgNC shown in (d) (line distance 150 nm), which is just in contact with the high contact, exhibiting no current at all. Hence, resistance switching due to Ag-migration through the SiO_2-layer of the substrate instead of the SiNP can be excluded. Reprinted with permission from [156] © 2020 American Chemical Society.

the thickness of the CF is controlled by the value of the compliance current. To perform the RESET operation a negative bias is applied to the AE leading to Ag ion migration from the PE towards the AgNC leading to rupture of the CF, which results in the HRS (cf. 7.7 (f)).

In about 9 out of 11 cases, no CF could be identified in SEM after electrical operation. This may be due to a CF formation further away from observation, towards the center of the SiNP. However, predominantly in these samples, deformation of the AgNC and of the SiNP was typically observed. In particular, the edges of AgNCs close to SiNPs were found to be rounded, being an indication for material being removed due to migration into the SiNP, as can be seen in Fig. 7.9 (a). Moreover, the adjacent SiNP was also found to be deformed, i.e., its spherical shape was significantly distorted towards the AgNC. This change of SiNP shape can

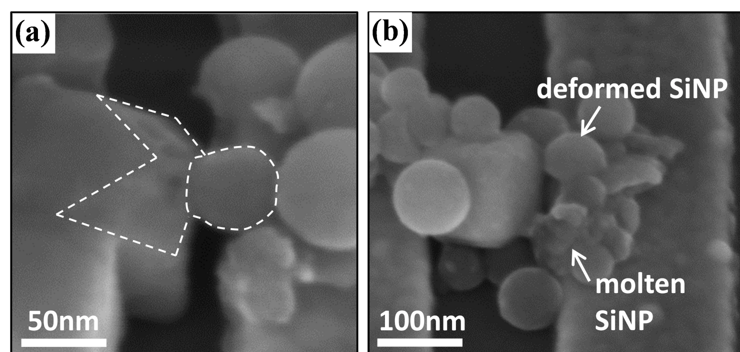

Figure 7.9 (a) Additional SEM image of a NP-dimer after electrical operation. Some material on the edge of the AgNC is being removed and the adjacent SiNP is slightly deformed and distorted towards the AgNC. These observations additionally support the assumption of Ag migration from the AgNC through the SiNP towards the Au contact. (b) NP-agglomerate after destructive electrical operation with irreversible shortcut. Molten and deformed SiNPs can be observed, being also indicative for material flow and Joule heating in SiNPs. Reprinted with permission from [156] © 2020 American Chemical Society.

be attributed to local Joule heating and material flow. In the case of irreversible break-through of NP-memristor devices, SiNPs were destroyed with their initial shape not identifiable anymore as exemplary shown in Fig. 7.9 (b).

7.5 Summary

In summary, the directed self-assembly of nano-scale metal-semiconductor composites and their memristive switching characteristics were demonstrated. By choice of surfactant and solvent, the size distribution of resulting Ag-nanocube/ Si-nanoparticle agglomerates could be controlled, ranging from NP-dimers, trimers up to higher order oligomers. Electrical characterization of individual, composite NP-dimers on an interdigitated electrode platform yielded stable and reproducible memristive switching with excellent device performance. The origin of memristive switching is attributed to Ag-ion migration in the poly-crystalline SiNP core and therefore conductive filament formation and rupture according to the application of voltage biases of opposing polarity. This model explanation is strongly supported by in-depth scanning electron microscopy studies following electrical operation, where conductive material in the shape of a current carrying filament in the SiNP could be identified. Future studies shall be directed towards the controlled build-up and electrical investigation of larger aggregates, eventually comprising nanoparticles of more than two different materials. Once aggregates forming networks of several, interconnected memristive junctions can be realized, their potential use as basic neuromorphic network shall be further explored.

8 Fabrication and directed self-assembly of silicon nanocubes

8.1 Introduction

In this chapter, the fabrication, electrical characterization and self-assembly of silicon nanocubes (SiNCs) is reported. Arrays of highly doped SiNCs featuring edge lengths of 110 nm are fabricated in large yields on silicon-on-insulator substrates using nano imprint-lithography as well as wet chemical and dry etching techniques. Interdigitated electrode arrays serve as a platform for the electrical characterization of single SiNCs. Self-assembly of SiNC agglomerates in solution is realized by cube surface functionalization with self-assembled monolayers of trimethoxysilane molecules. Complementary terminal groups form covalent bonds between adjacent particles via Cu(I)-catalyzed alkyne-azide cycloaddition towards bottom-up, directed assembly of functional electrical building blocks. This chapter closely relates to the work presented in [116] © 2018 IEEE.

8.2 SiNC fabrication by electron-beam lithography

There have been various studies on the fabrication of spherical silicon nanoparticles (SiNPs), mostly relying on chemical synthesis involving sintering hydrogen silsesquioxane (HSQ) at high temperatures under inert atmosphere [64]. These chemical approaches have the advantage to yield high quantities in the range of several milligrams and good control over particle size distribution, as long as the size does not exceed a few nm up to 10 nm. However, the size regime beyond this value is hard to excess with chemical approaches. Especially for sizes exceeding 5 nm, no reliable chemical approach for the synthesis of non-spherical SiNPs exists. This is an issue when contact formation for electrical characterization is desired. In addition, the shape of these SiNPs is mainly spherical, which limits the amount of facets being available for functionalitation. This in turn limits the complexity of possible agglomerates in self-assembly processes. Moreover, in chemical synthesis, doping of NPs is hard to achieve, which is important for tuning important parameters such as conductivity and electron mobility for possible applications of NPs in novel energy or information storage devices.

To circumvent the above mentioned restrictions arising from chemical bottom-up synthesis of SiNPs, a novel top-down approach is implemented. In the following, the fabrication of Si-

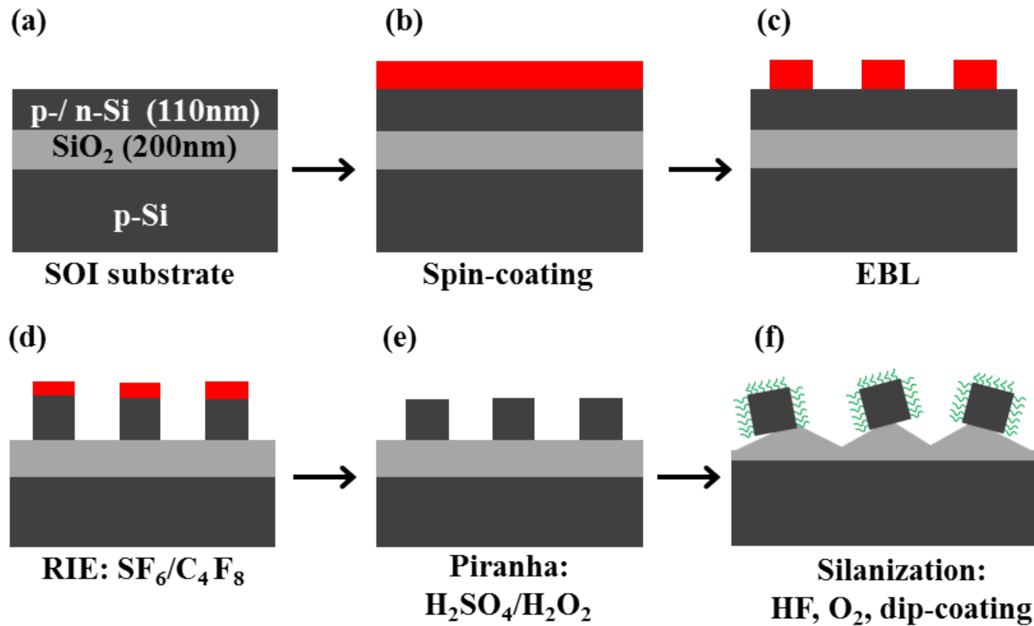

Figure 8.1 Schematic representation of Si-nanoparticle fabrication by electron-beam lithography. (a) The SOI substrate consist of a p-type handle wafer, a 200 nm thick thermal oxide layer and a device layer of 110 nm thickness. (b) At first, the wafer is covered by a negative-tone electron-beam resist (red color) by spin-coating. (c) Subsequently, the structures are written by EBL exposure and development, before (d) these resist structures are used as etch-mask for reactive ion etching, transferring the pattern into the device layer of the SOI substrate. (e) Residues of resist are removed by cleaning in Piranha solution, before (f) under-etching of particles by buffered HF and functionalization (green layer) for self-assembly is executed.

nanocubes (SiNCs) and Si-nanocylinders is described, using electron-beam lithography (EBL) and reactive-ion etching (RIE) on silicon-on-insulator (SOI) wafers. The respective work-flow of SiNC fabrication by EBL is depicted in Fig. 8.1. SOI wafer pieces (8 mm × 8 mm) consist of a p-type handle wafer (725 µm), a 200 nm thick buried oxide layer and a device layer of 110 nm thickness, as shown in Fig. 8.1 (a) and described in section 3.1. This device layer was either intrinsic or highly doped to yield p- or n-type properties. As described in Fig. 8.1 (b), the SOI wafer was at first coated by a negative-tone electron beam resist of 80 nm thickness (red color, AR-N 7520.07, 4000 rpm, 60 sec). After electron-beam exposure, as described in sec. 4.4 (Raith eLine, dose: 30 µC, 20 kV, 7.5 µm aperture), the structures were developed (AR 300-47 : H_2O = 4:1, 110 sec) as indicated in Fig. 8.1 (c). Subsequent EBL pattern transfer into the device layer of the SOI wafer is realized via reactive ion etching (RIE) using optimized parameters as described in sec. 4.3. The etch rate of this RIE process is highly selective, with the Si-etch rate being approximately 3.5 nm/sec and nearly zero in the buried oxide layer. Hence, the etch process stops as soon as the oxide is reached, as indicated in Fig. 8.1 (d). Residual contamination of SiNCs by EBL resist is removed by 'piranha' solution, where sulfuric acid (H_2SO_4) and hydrogen peroxide (H_2O_2) are mixed in a ratio of 2:1. It is crucial to firstly put the

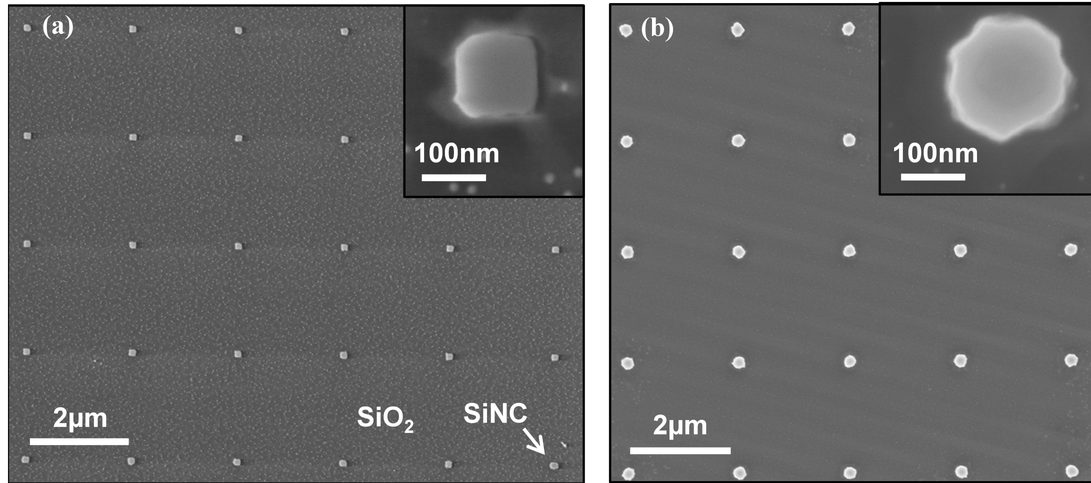

Figure 8.2 Scanning electron micrographs of (a) a typical array of Si-nanocubes and (b) Si-nanocylinders revealing high uniformity of particle size and high NP quality. Insets: close-up views of an individual SiNC and a Si-nanocylinder, showing larger sizes and enhanced edge roughness of nanocylinders.

H_2SO_4 into a clean glass beaker, and subsequently very slowly add the proper amount of H_2O_2, as the reaction is highly exothermic and any contamination with organic solvents of the beaker can cause severe reactions. The solution was then stirred together with the RIE-etched SOI samples for 15 min at a temperature of 150 °C on a hotplate. After cleaning, the SOI samples were carefully put out of the Piranha solution and rinsed in at least two separate beakers with DI H_2O and blown dry with dry N_2 (cf. Fig. 8.1 (e)). After reaction, the piranha solution was allowed to cool down and then diluted with DI H_2O and finally disposed in the acidic Piranha solution waste.

Fig. 8.2 (a) displays a typical excerpt of a SiNC array fabricated by EBL and RIE after piranha cleaning (cf. Fig. 8.1 (e)) confirming high uniformity of particles with sizes of (109.6 ± 3.5) nm and an inter-particle distance of 2 μm. A typical sample consists of up to $8 \text{x} 10^5$ particles, with the EBL exposure time being the major limiting factor to produce more particles per sample. A close-up view of a single SiNC in the inset shows low side-edge roughness and slightly rounded edges, arising from resolution losses in EBL and RIE processes. Additionally, as proof-of-principle, a typical array of p-Si-nanocylinders is shown in Fig. 8.2 (b). These cylinders were fabricated analogue to SiNCs, however using dot-exposure during EBL. Apparently, these strucutres are larger in size with a diameter of (206.5 ± 19.2) nm and their sides are not as smooth as compared to SiNCs, as apparent also from the SEM image in the inset. This could be due to overexposure during EBL which would make further optimization necessary, being beyond the scope of this work. However, the ability to access different Si-nanoparticle geometries by top-down fabrication from SOI is successfully demonstrated.

For self-assembly experiments in solution, SiNCs have to be removed from the buried oxide of the SOI substrate and dispersed in the respective reaction medium. To achieve weak attachment of SiNCs to the underlying SiO_2, under-etching by hydrofluoric acid (HF) is used, as indicated in Fig. 8.1 (f) by triangularly shaped oxide pillars below SiNCs. SOI samples after Piranha cleaning were immersed in 2 % buffered HF solution. While carefully agitating the sample in HF, the optical interference in the area of SiNC arrays arising from light scattering is monitored by eye. As soon as these scattering features in different colors disappear, SiNCs are displaced from their initial position, being indicative for complete detachment of SiNCs from the SiO_2. In this state, SiNCs are only physiosorbed to the substrate, which is enough not to loose them in the HF solution. Subsequently, samples are neutralized in two separate beakers of DI H_2O and carefully blown dry with a weak stream of dry N_2. Now, SiNCs are prepared for further use in self-assembly experiments.

8.3 SiNC fabrication by nano-imprint lithography

Si-nanocubes (SiNCs) with dimensions in the range of 100 nm serve as a promising platform to study SAM-mediated self-assembly of nanostructures. To produce these structures, also nano imprint-lithography (NIL) was used. This technique is widely used for patterning on the nano-scale and has the main advantage to be much faster (200-times) as our available electron-beam lithography (EBL) system, without any loss of NC quality concerning edge resolution and dimensions. In particular, the NC quantity is the most crucial parameter as it limits the NC concentration in the respective solvent during the self-assembly process. Sufficient concentrations of SiNCs fabricated by EBL could not be obtained in a reasonable amount of time, making the NIL process inevitable.
Fig. 8.3 shows the work-flow of SiNC fabrication via NIL. As shown in Fig. 8.3 (a) and described in section 3.1, highly doped SOI wafer serve as platform for SiNC fabrication. As a first step, an adhesion promoter and an UV-curable imprint polymer (mr-APS1 and mr-UVCur21, *micro resist technology GmbH*) are spin-coated onto the substrate as depicted in Fig. 8.3 (b). A polymeric working stamp (*OrmoStamp*) featuring recessed square holes of side length 110 nm × 110 nm and depth 110 nm was prepared according to the procedure described in sec. 4.6. These stamps were coated by an anti-sticking layer of perfluorooctyltrichlorosilane and subsequently pressed into the NIL polymer on the chip surface with a pressure of 5 bar, followed by cross-linking of the polymer by 3 min exposure to UV light (365 nm). As indicated in Fig. 8.3 (c) and (d), the stamp was subsequently removed and the obtained pattern etched into the Si device layer by a highly selective reactive ion etching process (gases: SF_6/C_4F_8, ratio 2:3), as described in 4.3. As a next step, 'piranha' solution (2:1 H_2SO_4:H_2O_2, 15 min, 150 °C on a hotplate) was used to remove residual polymer covering the top facets of SiNCs as shown in Fig. 8.3 (e). Finally, as illustrated in Fig. 8.3 (f), SiNCs were under-etched for later removal from the substrate, using 2% buffered HF and finally surface functionalized by silanization following an

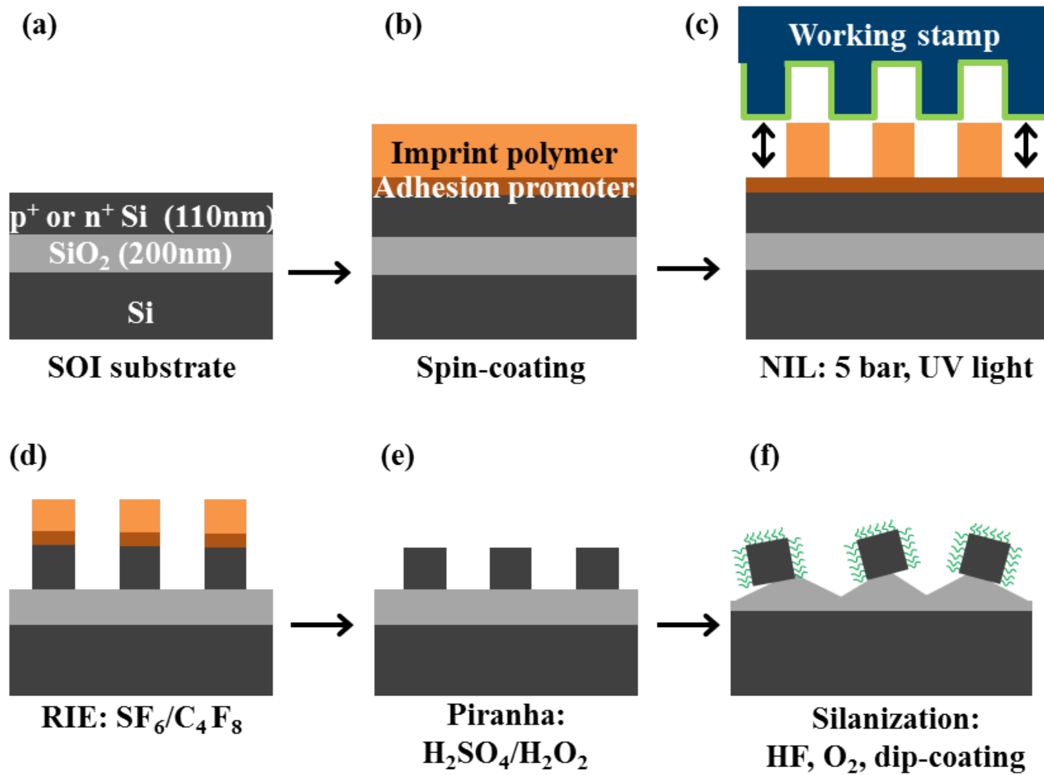

Figure 8.3 Schematic of the NIL-based fabrication process. A SOI wafer shown in (a) is coated with an adhesion promoter (dark green) and UV-curable polymer (red) as depicted in (b). In (c) the pattern of a prior fabricated working stamp, which is coated ny an anti-sticking layer (light green) is transferred into the polymer under high pressure followed by crosslinking of the polymer by exposure to UV-light. The obtained polymer pattern is transferred into the Si device layer by reactive ion etching shown in (d). Finally, SiNCs are cleaned by 'piranha' solution, under-etched by HF and functionalized by monolayers of respective silane molecules as depicted in (e) and (f). Reprinted with permission from [116] © 2018 IEEE.

O_2-plasma activation step.

Figs. 8.3 (a) and (b) show scanning-electron micrographs of a representative SiNC-array on SiO_2 after RIE-etching and removal of imprint polymer residuals with O_2-plasma and Piranha solution. Notably, the NIL process features a yield of 80% being equal to a NC-quantity of $2x10^7$ particles in an imprint area of 3 mm × 3 mm on a typical sample. In addition, homogeneous heights and side-lengths are observed as derived by SEM in top-view and tilted geometry and atomic force microscopy (not shown here). As can be seen in Fig. 8.3 (c), where a SEM image was taken under a tilt-angle of 45°, the SiNCs have slightly rounded edges and their side-walls are not perfectly smooth. These resolution limits mainly arise from the NIL process, as the structure which is transferred into the Si-layer is already the third replicate of the original structure on the Si-master stamp. Both the EBL and RIE processes additionally contribute to a slight loss of resolution. Additional to the fabrication speed, another major advantage of this

approach is the variability in nanostructure size, geometry and doping concentration, as e.g. also triangular or circular shapes are feasible by structuring the Si-master stamp as desired.

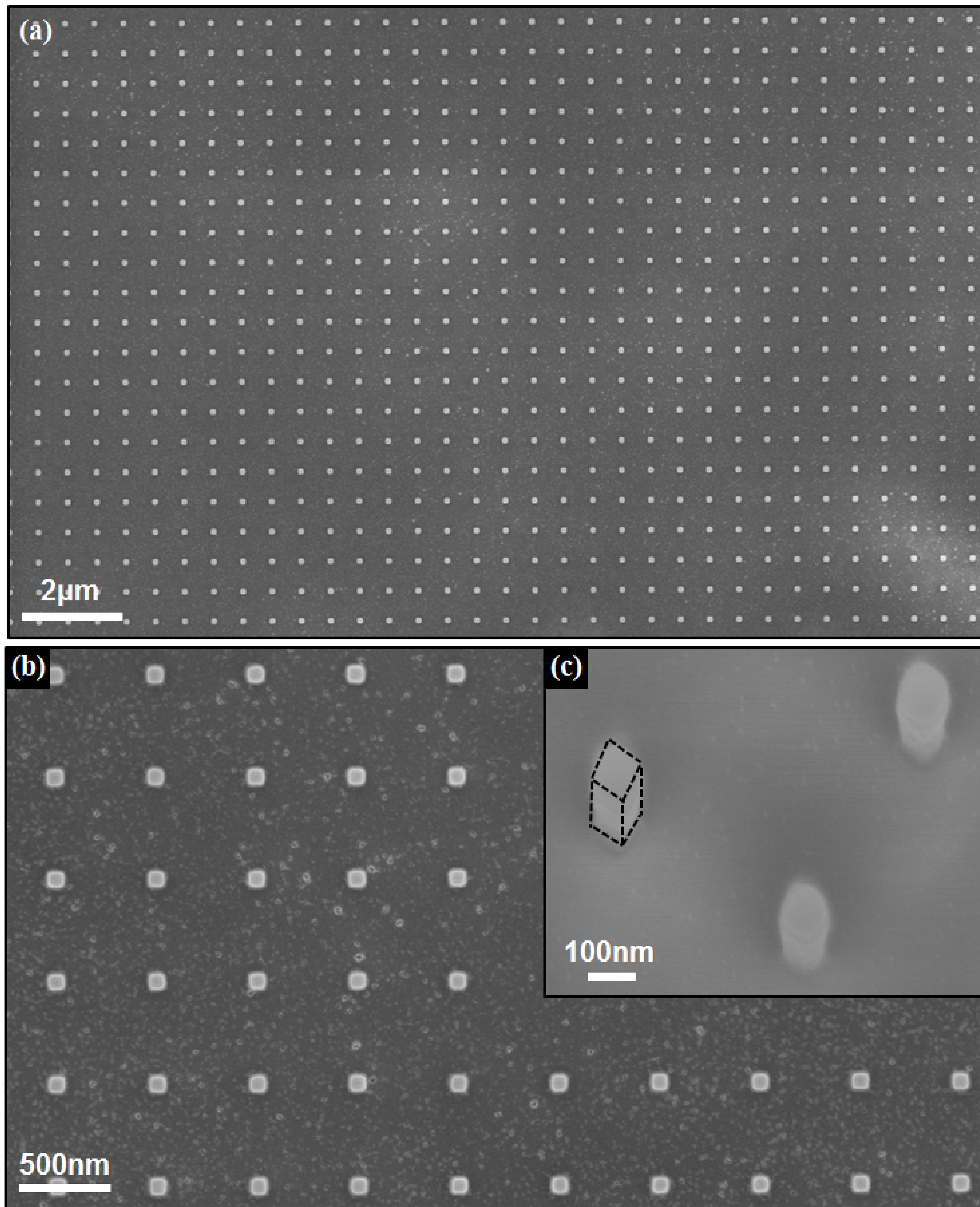

Figure 8.4 Strucural investigation of SiNC arrays by scanning electron microscopy. (a) and (b) Highly ordered arrays of SiNCs were formed on SOI wafers, featuring uniform size distribution and inter-particle distance. (c) Close-view SEM image of typical SiNCs obtained at a stage tilt angle of 45°, revealing slightly rounded edges and smooth side-facets. Reprinted with permission from [116] © 2018 IEEE.

8.4 Electrical characterization of single SiNCs on interdigitated electrodes

As a first proof of principle, two terminal electrical measurements were performed on both p- and n-type SiNCs. As top-down fabrication of electrical contacts to single particles with sizes of 100 nm by EBL is hard to achieve, SiNCs were drop-casted onto interdigitated electrode (IDE) arrays from solution, providing contact to single NCs on a coincidental basis, as shown in the SEM image of Fig. 8.5 (a) and (b). IDEs were fabricated on top of a thermal SiO_2 layer (50 nm) of Si wafer pieces (12×12 mm^2) by EBL, metal deposition and lift-off, and consisted of two rows of 30 opposing Ti/Au strip lines (5/30 nm thickness) with a width of 200 nm, a length of 40 µm and a spacing of 80 nm. Two rows of strip lines were each separately connected to large contact pads (50 µm × 50 µm) for probe-station measurements. Fig. 8.5 (c) displays the successful electrical characterization of a single p-SiNC captured in-between two adjacent IDE strip lines by drop-casting from NC suspension (I-V traces taken with a *Keithley 2635B* SMU within a *LakeShore TTPX* cryo-probestation at 5x10^{-6} mbar, room temperature, as described in sec. 5.6.2). Prior to I-V measurements, single SiNC contact formation was confirmed by SEM. Clearly, bridging the gap between two metal contact lines by a single NC resulted in a significant increase in conductance, as apparent from the I-V data in Fig. 8.5 (c). Still, the measured total current is small (sub-nA regime), which can be assigned to the charge injection barriers at the small-area SiNC/Au Schottky contact interfaces. We regard this first electrical test as successful demonstration of our IDE platform for future electrical characterization of functional SiNC agglomerates.

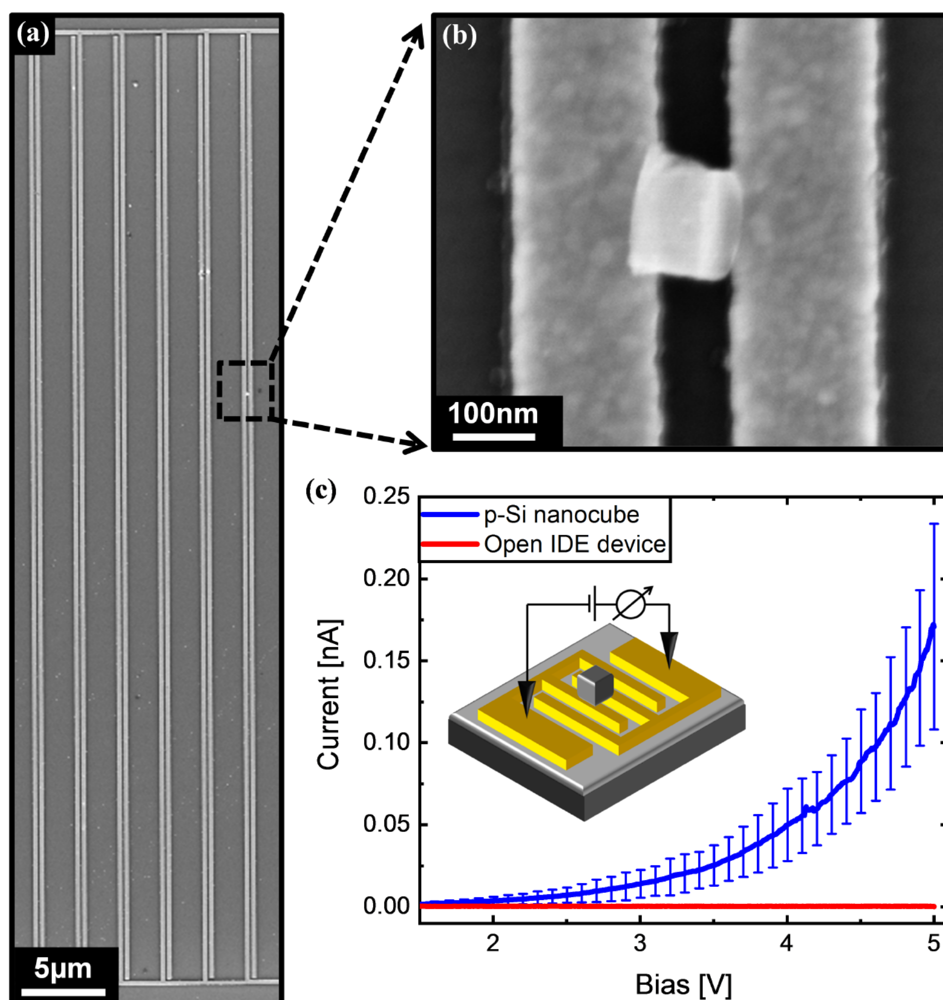

Figure 8.5 2 (a) Scanning electron micrograph of an excerpt of a typical IDE array fabricated by EBL. In total, two rows of 30 opposing Ti/Au strip lines with a thickness of 5 nm/30 nm, a width of 200 nm, a length of 40 µm and a distance of 80 nm are each separately connected to large contact pads for probe-station measurements (not shown). (b) Close-up view of a single SiNC contacted by two Ti/Au lines. (c) Current as a function of applied bias of the single p-SiNC shown in (b). The absolute value of the current obtained for 10 current-voltage sweeps for both positive and negative voltage is shown as average, together with error bars (standard deviation), in blue; the leakage current of the same device prior to SiNC deposition (open electrode gap) is shown in red. Inset: Schematic of the measurement setup. Reprinted with permission from [116] © 2018 IEEE.

8.5 Silane-based Cu(I)-catalyzed azide-alkyne cycloaddition on planar substrates

For self-assembly of SiNC agglomerates in solution, Cu-catalyzed alkye-azide cycloaddtion reaction was used (CuAAC, cf. sec. 2.5). To investigate chemical reaction yield, the whole procedure was at first executed on the native oxide surface of planar p-Si and SOI samples and resulting SAMs characterized using AFM, ellipsometry, XPS and hanging Hg droplet electrode.

8.5.1 Structural characterization of self-assembled monolayers

SAM thickness determination

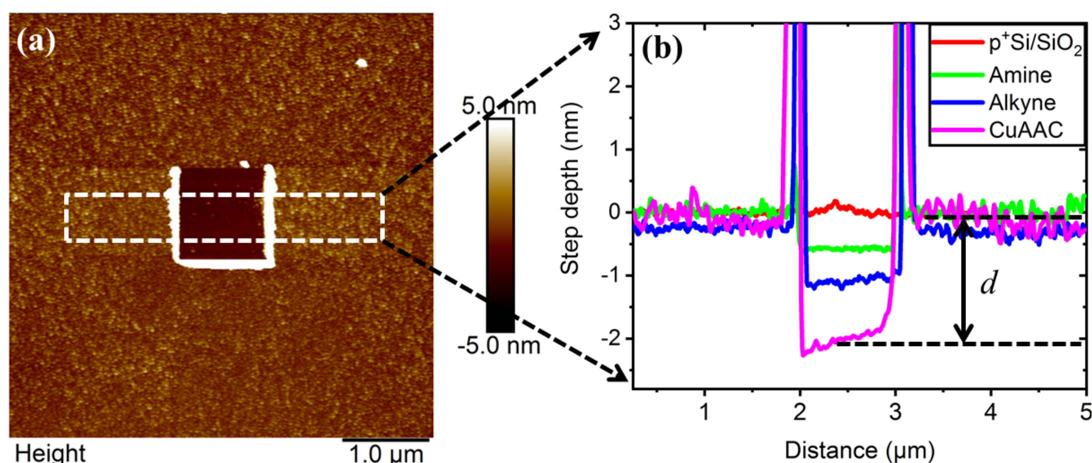

Figure 8.6 (a) Exemplary tapping mode AFM micrograph of a CuAAC-reacted silane SAM on p-Si/SiO_2 (cf. sec. 2.5) after AFM nanolithography scratching (cf. sec. 5.3). In the middle of the 5 μm × 5 μm-sized scan-field, the SAM was removed in contact mode (dark area) in a 1 μm × 1 μm-sized area. Bright areas of increased height on both sides and on the bottom of the scratched area correspond to removed surfactant material by the tip. The resulting height profile is detected in subsequent tapping-mode imaging, and the step depth measured in *NanoScope Analysis* software. This was done for all types of SAMs and the bare substrate, as shown in (b). Following chemical reaction steps described in Fig. 2.7, molecule length and therefore also SAM thickness d increases (cf. sec. 2.3), resulting in deeper depth profiles (red to magenta). This is an indirect proof of successful cycloaddition reaction.

To determine the thickness of SAMs grown corresponding to the reaction scheme shown in fig. 2.7, AFM nanolithography scratching was used on at least five different samples at three different spots each. As described in sec. 5.3, at first, an area of 5 μm × 5 μm was raster-scanned in tapping mode AFM to verify suitability of the area, i.e., to exclude contamination. Afterwards, in an area of 1 μm × 1 μm, the SAM was removed by contact mode AFM, which corresponds to the dark area in Fig. 8.6 (a). As a last step, the whole area was investigated again in tapping mode to measure the step depth. Ideally, in the scratched area, the underlying substrate is exposed, and the step depth is directly correlated with the SAM thickness d. Apparently, bright areas of enhanced height on the left and right and on the bottom of the exposed area are present after scratching, corresponding to removed surfactant material, as the tip moved from top to bottom and scanned the surface from left to right. Fig. 8.6 (b) exemplary shows various steps of SAMs featuring different thicknesses due to increasing molecule length with the number of chemical reactions taking place on the surface. The reference experiment on bare Si oxide (red color) features no change in height inside the scratched area, indicating proper set point calibration (0.5 V). However, depth of amino-SAMs ((0.59 ± 0.04) nm, green color), alkyne-terminated SAMs ((0.86 ± 0.13) nm, blue color) and click-reacted SAMs ((1.89 ± 0.22) nm, magenta color) show expected trend towards deeper steps, indicative for successful chemical

reactions.

Values of SAM thickness d obtained by AFM are compared with values obtained by ellip-

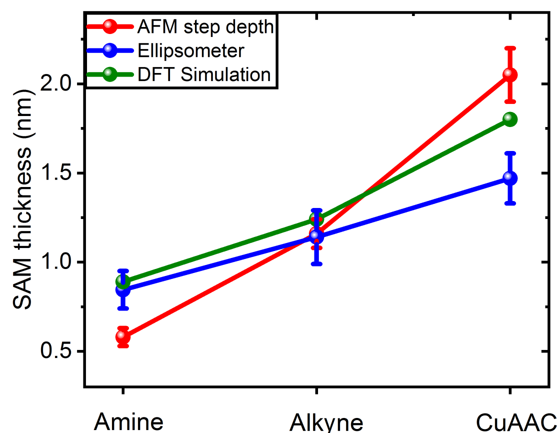

Figure 8.7 Silane-SAM thickness d on p-Si/SiO_2 for different types of SAMs following the click reaction described in sec. 2.5. In red and blue color, d is determined by AFM nanolithography scratching, as shown in Fig. 8.6 and by ellipsometer measurements. In both methods, an increase of d is observed. However, this increase is measured to be less pronounced by ellipsometry. For comparison, the theoretical molecule length is simulated by density functional theory (DFT) in *Gaussain* software.

sometry using a two-layer model and a value of 1.46 for the refractive index of SAMs (cf. sec. 5.5). As shown in fig. 8.7, deviation occurs for smaller and larger silane molecules (amine and CuAAC). In addition, both experimentally obtained values are compared with the theoretical molecule length simulated by density functional theory (DFT) in *Gaussain* software (green color). Taking into account that d cannot by larger than the molecule length, values of ellipsometry measurements appear to be slightly more reliable, as these values are always below DFT values and also exhibit less deviation for all three lengths. However, values of both experimental methods have to be considered as approximations to the real value of d. Firstly, in AFM experiments, interaction forces between SAM terminal groups and AFM tip can vary, as amine, azide and silane terminal groups exhibit different polarities and therefore interact more or less attractive with the tip. Also, during scratching, surfactant material is supposed to agglomerate at the tip surface, potentially influencing subsequent tapping mode measurement. For ellipsometry, an approximate value of 1.46 for the refractive index of SAMs is used. This value is an empiric one, and based on the assumption of mainly carbon atoms being present in the SAM [62]. However, SAM composition varies for different types of SAMs. In addition, a SAM of molecules is modeled as a perfect crystalline thin film, not taking into account defects like pinholes and multilayers as well as molecule distortions.

Using values of d acquired by ellipsometry and making use of equation 2.4, molecule tilt angles Θ_t of $(18 \pm 4)°$, $(23 \pm 3)°$ and $(45 \pm 1)°$ for amine- and alkyne-terminated SAMs and click-reacted SAMs are obtained, respectively. Hence, larger molecule length apparently results

in larger tilt angles. For AFM data of d, this trend is also visible comparing red and blue lines in Fig. 8.7.

XPS analysis of SAMs

Additional XPS measurements were carried out by technicians in the 'Nanofab' laboratories at the department of chemistry at the University of Alberta providing detailed information on chemical composition of SAMs on SOI wafers, which were used later for SiNC fabrication (cf. sec. 5.4 and sec. 8.3). In total, four samples, two samples each with n- and p-type device layer doping with amine-SAMs were investigated. Two of them, one with n- and one with p-type device layer doping were further reacted until the end of the click-reaction and measured again for consistency. In addition, two samples with n- and p-type doping with azide-SAMs were studied, to proof the successful formation of amine- and azide SAMs on the one hand, and successful cycloaddition reaction on the other hand. Fig. 8.8 shows exemplary spectra

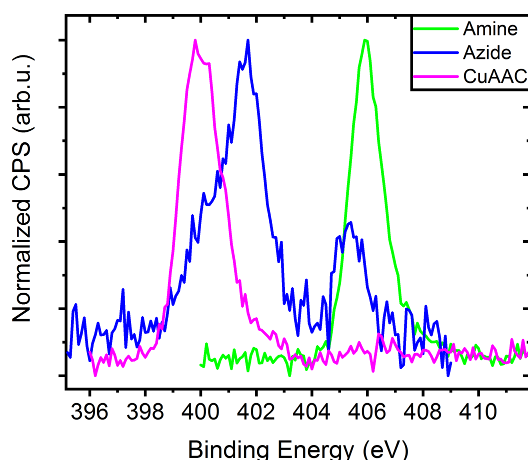

Figure 8.8 High resolution XPS spectra of N1s peaks of amine (green), azide (blue) and cycloaddtion-reacted silane SAMs (denoted with CuAAC, magenta) on SOI samples showing a characteristic chemical shift towards lower binding energy for the triazole moiety. This is an indirect proof of amine-to-triazole transformation and therefore successful cycloaddition reaction. In addition, a characteristic double peak for the azide terminal group corresponding to N^+ and two N^- oxidation states is observed.

of N1s peaks of amine-, azide- and click-reacted SAMs (denoted as CuAAC) in green, blue and magenta color, respectively. Several features can be observed: i) for the click-reacted compound, the N-containing triazole linker gives rise to a chemical shift of the N1s peak towards lower binding energies from amine at 406 eV to triazole at 400 eV (peaks of green and magenta spectra). This is due to lower positive oxidation state of N in the triazole as compared to in amine, hence being an indirect proof of amine-to-triazole conversion via CuAAC reaction. In addition, ii) for SAMs with azide-terminal group, two characteristic peaks at 401 eV and

405 eV area detected, corresponding to N^- and N^+ oxidation states, respectively. All these values are in good agreement with literature [102, 128].

8.5.2 Electrical characterization of SAMs by Hg droplet electrode

Electrical characterization of silane-SAMs on p-Si/SiO_2 following the chemical reaction scheme as described in Fig. 2.7, was executed using hanging Hg droplet electrodes (cf. sec. 5.6.3). In total, 8 samples were characterized for each type of surface, with at least three droplets at different positions on a sample. For each droplet, a photograph was taken for subsequent contact area calibration and at least three IV-sweeps (from 0 V to +1 V to -1 V and back to 0 V with a sweep rate of 0.1 V/s) were conducted at each spot. Hence, in total at least 72 IV-traces were recorded for each surface. Fig. 8.9 (a) shows resulting mean IV traces with error bars for standard deviations on a semi-logarithmic scale of all surfaces characterized and an image of a typical Hg droplet in the inset. From red to magenta color, SAM thickness d increases, apparently resulting in decrease of current density J. This might be due to the tunnel barrier thickness for charge injection increasing with increasing molecule length. Hence, this decrease of current density with number of chemical reactions might as well be an additional indirect proof for successful SAM formation and cycloaddition-reaction.

To gain further insight into charge transfer through SAMs, the logarithm of the absolute value

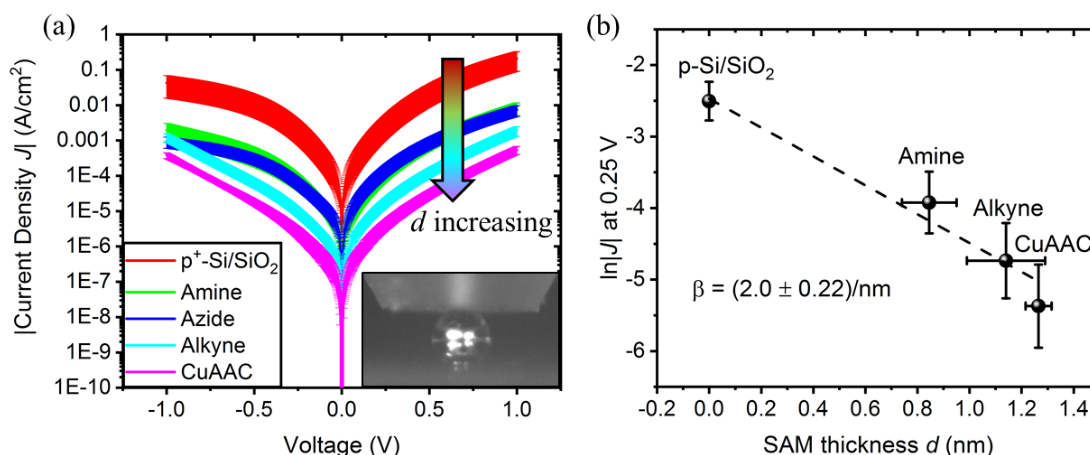

Figure 8.9 (a) Current density J as a function of applied bias voltage with error bars of various silane SAMs on p-Si/SiO_2 (cf. sec. 2.5) and reference substrate measured by hanging Hg droplet electrode, as shown in the inset (cf. sec. 5.6.3). For small biases, the current density monotonously decreases for increasing molecule length, following a Simmons-type model fit of tunneling current. As shown in (b), this model is verified plotting the logarithm of the absolute value of J at a fixed bias voltage of 0.25 V as a function of tunnel barrier thickness. This barrier thickness is the thickness of the native oxide plus SAM thickness d. A characteristic approximately linear correlation is obtained, with a linear fit resulting in a large tunnel decay constant β of 2.0 /nm.

of J at a small bias of 0.25 V, was plotted as a function of SAM thickness d, measured by ellipsometry. For small values of the applied bias, near-equilibrium conditions can be assumed

and contributions from Fowler-Nordheim tunneling neglected (cf. section 2.4). Apparently, an approximately linear correlation is obtained. Applying a linear fit to the data, and making use of eqn. 2.6, a characteristic tunnel decay value β of $(2.00 \pm 0.22)/\mathrm{nm}$ is obtained, indicative for trap-assisted tunneling charge transfer mechanism [78, 80]. In fact, this large value might originate from conformational differences of present silane-SAMs, as many different chemical moieties are located in the backbone, as compared to values for common SAMs such as alkyl SAMs in a range of 0.5 to 1.15 per carbon atom [69].

8.6 Functionalization and self-assembly of SiNCs

In order to assemble Si-based functional electrical building blocks, bottom-up self-assembly of SiNCs based on cross-reactive self-assembled monolayers was investigated. For this purpose, after being under-etched by HF (see Fig. 8.3 (f)), the surface of SiNCs of two different samples was first enhanced with hydroxyl groups by O_2-plasma (200 W, 5 min) and subsequently functionalized by grafting self-assembled monolayers of phenyltrimethoxysilane (PTMS) molecules (*Gelest Inc.*) containing different groups for further functionalization to the cube native oxide surface [102]. As shown in Fig. 8.10, SiNCs of type 1 were functionalized with azidoPTMS

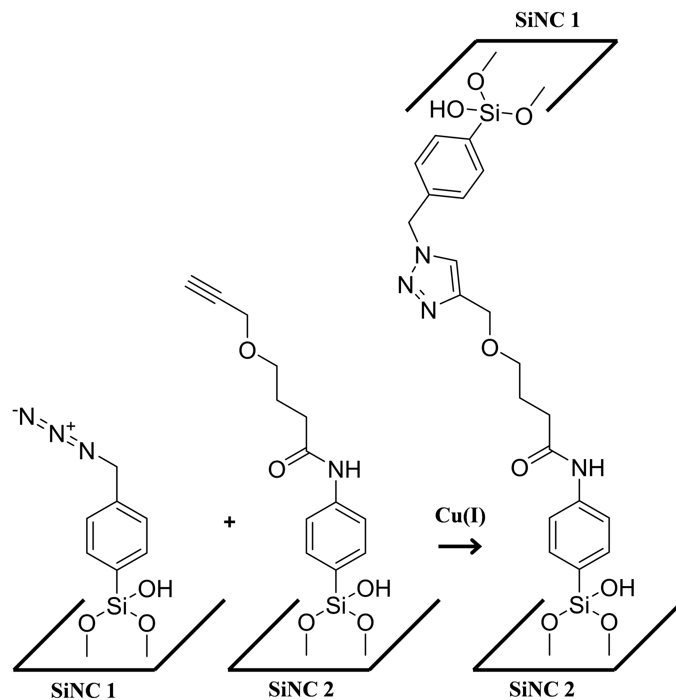

Figure 8.10 Schematic representation of the self-assembly process between two SiNCs. SiNC 1 and SiNC 2 are functionalized with monolayers of phenyl-silane molecules featuring complementary azide and alkyne terminal groups forming a triazole linker via CuAAC. Reprinted with permission from [116] © 2018 IEEE.

while SiNCs of type 2 with aminoPTMS, respectively (each 3 mM, 0.1% DI-H_2O in toluene,

24 h). After careful rinsing in toluene and methanol, SiNCs of type 2 were further reacted with propargyl-N-hydroxysuccinimidyl ester (3 mM, toluene, 24 h) to realize alkyne terminal groups, which are reactive with the azido groups in the presence of a catalyst. Subsequently, both types of SiNCs were removed from their respective substrates by sonication for 15 min and followed by dispersion in the same O_2-plasma cleaned glass vial containing 200 µl of catalyst solution (5 ml DMF, 8.8 mg sodium L-ascorbate, 6.2 mg copper(II) sulfate pentahydrate). Subsequent SEM imaging was employed to ensure complete SiNC removal from the chip's exposed, previously buried SiO_2 layer. The self-assembly process of the two types of cubes by Cu(I)-catalyzed alkyne-azide cycloaddition (CuAAC) was carried out on an orbital shaker for 3 days at 200 rpm. After self-assembly, SiNCs were washed 3-times in ethanol by centrifugation (5000 rpm, 5 min) to remove residual catalyst contamination.

Cube aggregates of different sizes (monomers, dimers and higher order oligomers) were classified and counted by SEM imaging after drop-casting on a clean Si substrate. As a control to verify the impact of forming covalent bonds between cubes we compared the self-assembly process with a reference process omitting the catalyst containing Cu(I) ions which is required to ensure covalent triazole bond formation between complementary SiNCs via CuAAC [95, 97]. Significant enhancement of SiNC agglomerate formation was obtained for the full bond-forming process that included the Cu(I) catalyst as clearly visible in the comparative histograms of Fig. 8.11. The inset highlights a typical SEM image of a SiNC dimer featuring large overlap of adjacent side-facets being indicative of a successful, directed self-assembly process.

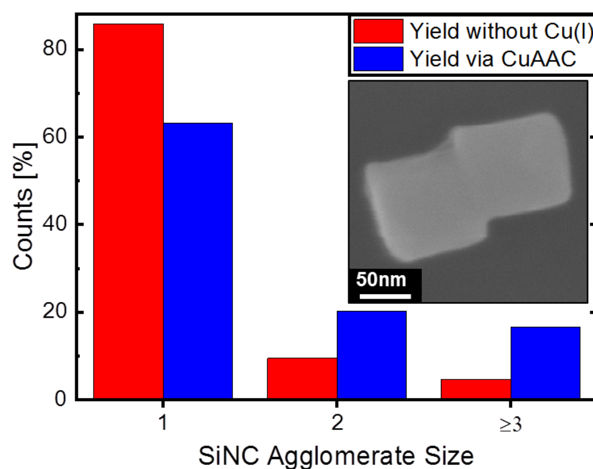

Figure 8.11 Histogram of self-assembly yield. A significant enhancement of SiNC dimer and oligomer formation is obtained by adding the Cu(I) catalyst (blue bars) compared to the control experiment without catalyst (red bars). Inset: scanning electron micrograph of a typical SiNC dimer revealing large overlap between two adjacent side-facets. Reprinted with permission from [116] © 2018 IEEE.

8.7 Summary

In summary, top-down fabrication, electrical characterization and bottom-up self-assembly of SiNCs was demonstrated. Reproducible fabrication by NIL and dry etching of highly doped SiNCs on SOI wafers with edge lengths of 110 nm in large yields was shown. Dispersion in polar solvents and electrical characterization of single SiNCs, contacted on IDEs featured currents in the nA-regime, which is an important step towards contacting larger functional agglomerates in this size regime in the future. In addition, SiNC surface functionalization and agglomerate formation via directed self-assembly using 'click'-reaction was demonstrated. The respective 'click'-reaction was also executed on planar substrates as reference and resulting SAMs featuring different thicknesses and chemical compositions characterized by AFM nanolithography scratching, ellipsometry, XPS and hanging Hg droplet electrode. Comparing the results of all these surface characterization techniques indicated successful silane SAM formation and 'click'-reaction. Electrically functional agglomerates of SiNCs may well become promising building blocks towards the bottom-up assembly of novel 3D device architectures and circuits.

9 Conclusion and Outlook

In the course of this work, functional nanoparticle-based materials were fabricated and characterized using different self-assembly approaches on-chip and in dispersion towards self-organized electrical systems. In particular, the goal was to develop efficient and reliable self-assembly techniques to

- assemble electrically functional nanoparticle-colloids in a directed manner and
- to form regular pattern of building blocks on surface via site-selective immobilization towards device integration.
- In addition, these building blocks shall deliver a certain electrical function reproducibly.

In the following, strategies on how these points were addressed are summed up and possible ways to improve the latter proposed.

Self-assembled silver-nanocube threshold selector arrays

Towards self-organized formation of regular pattern of functional building blocks on-chip, the site-selective immobilization of silver-nanocubes (AgNCs, edge-length 100 nm) on p-type Si/titanium-dioxide (TiO_2, sputter-coated, 2 nm to 20 nm thickness) substrates into highly ordered arrays was demonstrated. Arrays of AgNC threshold-selectors were assembled in suspension using complementary surface-functionalization of particles and substrate. Prior to self-assembly, the surface of AgNCs was functionalized by SAMs of thiols featuring alkyne terminal groups, whereas the surface of TiO_2 layers was patterned by square-shaped silane SAM areas, which had sizes of 200 nm × 200 nm and a pitch of 2 µm. These SAM areas featured azide terminal groups and were formed by evaporation of molecules into square shaped recess holes of electron-beam resist, pre-defined by electron-beam lithography (EBL). After removal of the resist, SAM areas served as immobilization sites for AgNCs during the subsequent self-assembly process. Exposing SAM-structured TiO_2 surfaces to functionalized AgNCs in solution providing Cu(I)-ions, covalent triazole bonds were formed between particles and substrate via Cu-catalyzed azide-alkyne cycloaddition reaction, also referred to as 'click'-reaction. This way, regular arrays of AgNCs were formed with a yield of ~36 % of particles positioned at anticipated SAM target sites. Subsequent electrical characterization of individual AgNCs by conductive-probe atomic force microscopy (CP-AFM) revealed threshold switching (TS) behavior with ultra-low off currents in the sub-pA range, steep turn-on slopes <50 mV/decade

and a selectivity of ~10^3. TS is a special type of memristive switching phenomenon, where the low-resistance-state (LRS) is not retained in the low-voltage regime. TS devices can be used as selectors in cross-point arrays for the suppression of sneak-path currents. To investigate the origin of resistance switching mechanism, detailed ex-situ studies after electro-forming of AgNC devices were performed, including CP-AFM and cross-sectional scanning electron microscopy (SEM) after focused-ion beam milling (FIB). Additional kinetic Monte-Carlo simulations of Ag-ion migration in oxide layers supported the assumption of unstable Ag-conductive filaments preferentially growing below AgNC edges.

To improve self-assembly yield, template-assisted self-assembly could by used, where capillary forces in a modified Langmuir-Blodgett process are used to form 2D colloidal crystals on surfaces. However, this technique requires a physical template consisting of pre-defined holes and has therefore no significant advantages compared to conventional top-down fabrication techniques such as evaporation and lift-off. For improvement of self-assembly omitting physical templates, e.g. via molecular recognition such as shown in this work, improving the efficiency of the underlying chemical reaction between NP and substrate is required. One possible way to do so would be to choose a reaction involving a smaller number of reaction species. A step towards minimizing reaction complexity would be to replace azido-silane SAMs by SAMs of molecules featuring silane headgroups and thiol endgroups, or by using complementary DNA. This way, (nobel-metal) NPs could directly bind to anticipated sites without the need of a catalyst. In addition, reaction parameters such as concentration of NPs, time and intensity of agitation and temperature could be further optimized.
To improve threshold switching characteristics such as absolute values and standard deviations of set and hold voltages, solid-state contacts to individual AgNCs for electrical measurements are indispensable. This would also circumvent measurement instabilities arising from CP-AFM. Also, electrical characterization in a probestation setup would be possible, enabling more advanced studies such as temperature dependent measurements and pulsed excitation. For top-town fabrication of AgNC top-contacts, a lift-off process would need to be developed. Such a process would include definition of alignment markers on oxide substrates prior to self-assembly as a first step. Secondly, after AgNC-array formation, a dense insulator would need to be deposited between AgNCs not covering AgNC top-facets (e.g. via atomic layer deposition and reactive-ion etching). At the end, EBL, metal deposition and lift-off could be used to define top-contacts. For measurements of individual AgNCs, the p-Si substrate could be used as bottom contact. However, it is crucial that the insulator separating top-contacts and oxide surface has no pin-holes, which would result in short circuits. This is hard to achieve, as AgNCs only have a height of 100 nm. Hence, as a first step, micrometer-sized particles could be used enabling usage of planarizing dense organic polymers such as benzocyclobuten (BCB). Moreover, to gain further information on filament geometry and material composition, cross-sectional transmission electron microscopy (TEM) studies in combination with energy-dispersive

X-ray diffraction (EDX) for elemental analysis should be in the focus of future studies. For this purpose, TEM lamellas would need to be cut out of electroformed particles and subsequently transferred onto a TEM grid via a micro-manipulator, which is a challenging task on this length scale.

Bipolar memristive switching in self-assembled silver-nanocube/silicon-nanoparticle dimers

Towards the directed self-assembly of fully electrical functional buidling blocks, binary NP-aggregates were formed in suspension consisting of single AgNCs covered by one or more spherical Si-nanoparticles (SiNPs, chemically synthesized, ~60 nm diameter), aiming at the formation of AgNC/SiNP-dimers. By careful tuning of surfactant and polarity of solvent during self-assembly, the size of resulting aggregates was controlled. In detail, by using 1-octanethiol in dimethylformamide (DMF), three sides of AgNCs were preferentially covered by a SiNP. By contrast, using (3-mercaptopropyl)trimethoxysilane (MPTMS), the assembly process mainly yielded trimers, where only two side facets of AgNCs were preferentially covered by a SiNP. By contrast, omitting surfactants, i.e., using as-obtained AgNCs covered by polyvinylpyrrolidone (PVP), no specific aggregate formation was obtained yielding mainly single AgNCs. For electrical characterization of AgNC/SiNP-dimers, single aggregates were contacted on interdigitated nanogap electrodes (IDEs, gap between Ti/Au fingers: 150 nm) via drop-casting, eventually contacting the AgNC on the one side and the SiNP on the other side. In this configuration, the AgNC acts as active electrode, the poly-crystalline SiNP as solid electrolyte and the Ti/Au finger contacting the SiNP as passive electrode in an electrochemical metallization cell (EMC) configuration. Electrical characterization of individual dimers yielded non-volatile bipolar memristive switching with narrow distributions of set voltages of $\overline{V_{SET}}$ =(3.1 ± 0.2) V, presumably owing to a small interparticle interface confining metal-ion injection. In addition, the system showed stable resistance state retention, making it well suitable for application in future self-organized resistive random access memory (ReRAM) circuitry. Detailed SEM studies after electrical operation revealed cone-shaped conductive filaments in some SiNPs, supporting the assumption of filamentary-type memristive switching.

Future studies should focus on the more controlled fabrication of contacts to single NP-dimers, e.g. via top-down methods to enhance contact areas improving device performance and therefore enabling more in-depth physical studies. For this purpose, a lift-off process involving EBL and metal evaporation after aggregate drop-casting onto substrates with alignment markers would need to be implemented and optimized. However, the available EBL system is not well suitable for the fabrication of contacts on this length scale. Therefore, direct-write techniques of contacts, i.e. by helium ion microscopy (HIM) might be a possible way to gain enough resolution.

In addition, the next step towards fully operational, self-assembled NP-based cross-point arrays

would be the directed assembly not only of single AgNCs as described before, but the assembly of arrays consisting of AgNC/SiNP-dimers on TiO_2. This way, a NP-based one selector-one resistor configuration (1S1R) would be formed, a big step towards true expansion of circuitry into the third dimension. For realizing such structures, the self-assembly of NP-dimers would need to be highly selective and the yield of immobilized NPs on surfaces increased.

Fabrication and self-assembly of Si-nanocubes

Towards the development of functional NP-based building blocks based on Si, cubic, highly p- and n-type doped Si-nanocubes (SiNCs) with edge-length of 110 nm were fabricated by nano-imprint lithography (NIL) and reactive-ion etching (RIE) in high yields on silicon-on-insulator (SOI) wafers. On a typical sample, $\sim 2\text{x}10^7$ particles in an area of $\sim 3\,\text{mm} \times 3\,\text{mm}$ were obtained with excellent structural uniformity. Subsequent surface-functionalization by SAMs of trimethoxysilanes, dispersion and directed self-assembly of SiNC-colloids was demonstrated using copper-catalyzed azide-alkyne cycloaddtion reaction, also referred to as 'click'-reaction.

Major advantages of this physical approach of fabricating doped SiNPs compared to chemical synthesis are the large freedom concerning size and shape, which only depend on SOI device layer thickness and NIL stamp shape, and doping concentration, which in turn only depends on doping of SOI device layer. However, for more efficient self-assembly of NP-colloids in suspension, the NP concentration needs to be further enhanced as less SiNPs are obtained by NIL compared to chemical approaches, where NPs are usually given as powders or dense dispersions. Hence, future studies should focus on increasing SiNP concentration potentially increasing self-assembly yield significantly. Possible ways to fabricate more SiNPs per SOI sample might be the fabrication of larger stamps containing more structures per area, or using multi-beam EBL setups for fast direct and dense patterning of SOI wafers. A more easy approach might be the fabrication of slightly larger SiNPs, i.e. by using thicker SOI device layers with a thickness of ~500 nm to 1 µm and using larger feature sizes on stamps. This would allow for more easy handling of NPs and more reliable fabrication of contacts to future SiNP-based devices by top-down lithography.

A Resistive switching in single core-shell nanoparticles

Nanoparticle-based memristive switching devices are promising candidates for future low-cost memory applications since metal, oxide and semiconductor nanoparticles (NPs) can be reliably synthesized in high yields and processed in solution for, e.g., flexible electronics. However, so far mostly non-volatile resistance switching in NP-based layer- or ensemble structures has been demonstrated [23, 26, 163–165]. For down-scaling purposes and better control over device performance, it would be highly desirable to incorporate different resistive switching functions in single heterogeneous NPs. In addition, such NPs can effectively be self-assembled in a directed manner on chip, potentially overcoming restrictions arising from lithography-based fabrication, and paving the way towards novel high-density 3D memory and neuromorphic computing architectures [116, 166, 167]. In this chapter, resistive switching in single spherical core-shell Ag/SiOx-nanoparticles (CSNP) of diameter 150 nm is reported. These nanoparticles were contacted by interdigitated electrodes (IDE) and exhibit either bipolar memristive or threshold switching with OFF/ON resistance ratios in excess of three orders of magnitude. A switching mechanism based on silver ion migration in the silica shell is proposed, which leads to reversible conductive filament formation and rupture. Application of CSNP as functional building blocks in future self-assembled 3D memory architectures or neuromorphic networks is proposed. This chapter closely relates to the work presented in [167] and most of the experiments and measurements were executed by Xinrui Xi in the framework of her Master's thesis [168].

A.1 Fabrication of core-shell nanoparticle devices

In order to fabricate electrical contacts to single CSNPs, an interdigitated electrode (IDE) platform was used, as lithography-based top-down fabrication of contacts to NPs this size (~150 nm) is hard to achieve. These IDEs were fabricated on top of a thermal SiO_2 layer (50 nm) of Si wafer pieces (12 nm × 12 nm) by electron beam lithography (EBL), metal evaporation and lift-off (cf. section 4.4). As can be seen in Fig. A.1 (a), an IDE consists of two rows of 30 opposing Ti/Au strip lines (5/30 nm thickness) with a length of 40 µm, a width of 200 nm and a spacing of 80 nm. For probe-station measurements, each of the two rows of strip lines was separately connected to square shaped contact pads (50 µm × 50 µm). The specific spacing of

strip lines measuring 80 nm was used to account for the size and geometry of the NPs being contacted later, whereas a metal thickness of 5/30 nm (Ti/Au) was chosen to obtain optimal lift-off results after metal evaporation. For electrical contact formation, at first the as-obtained CSNP

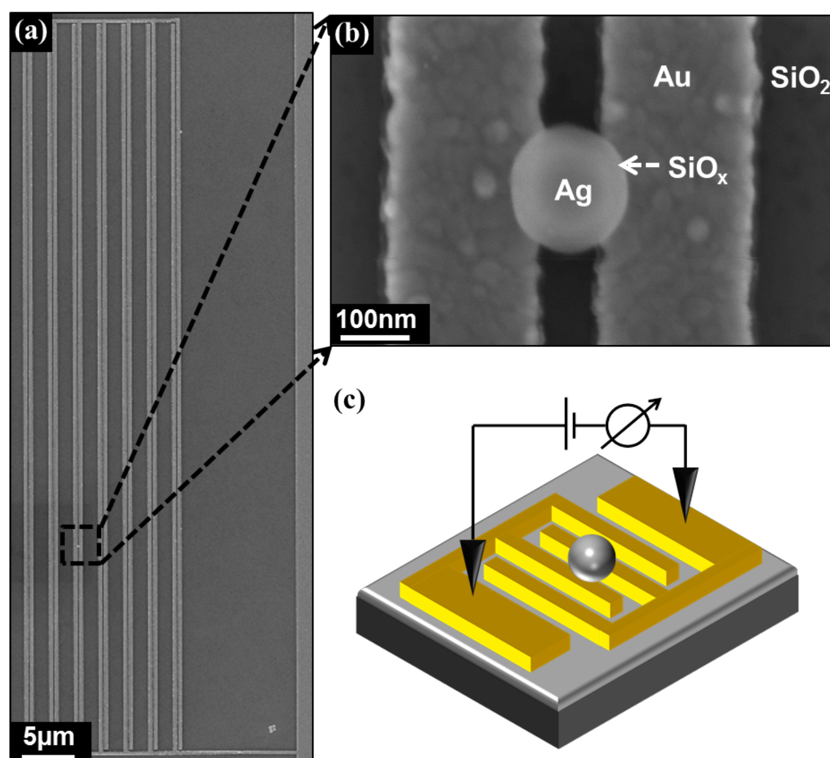

Figure A.1 (a) SEM image of an excerpt of a typical IDE structure fabricated by EBL, evaporation and lift-off, which consists of two rows of 30 opposing Ti/Au strip lines on Si/SiO_2 with contact pads on each side for probe-station measurements. One of the pairs of strip lines is bridged by a single CSNP, highlighted by the dashed black box. (b) Close-up view of this nanoparticle, where its Ag-core and SiO_x-shell can be identified. (c) Schematic illustration of the measurement setup. Reprinted with permission from [167] © 2020 IEEE.

suspension (cf. section 3.5) was diluted down to a concentration of 15 ng/mL ($2.4 \cdot 10^6$ NP/ml) in ethanol. These NPs consist of a (107 ± 11) nm- diameter Ag core and a surrounding 22 nm thick SiO_x shell, resulting in an overall NP diameter of (152 ± 11) nm. The NP shell is an amorphous network of silicon and oxygen and was added to the previously synthesized Ag particle surface via the base catalyzed condensation of various silanes such as tetraethylorthosilicate in a Stöber growth based procedure. Amounts of 50 µL of the diluted suspension were dispensed onto previously cleaned IDEs and allowed to dry in ambient. After the solvent had evaporated, the sample was examined by optical and scanning electron microscopy. This process was repeated until a single CSNP was eventually located in-between two strip lines as illustrated in Fig. A.1 (b) and (c), showing a SEM) image of a CSNP device after measurement and a schematic of the measurement setup, respectively. In such functional device, a single CSNP is bridging the nano-gap between two Au leads and is therefore contacted successfully.

A.2 Bipolar and unipolar resistive switching

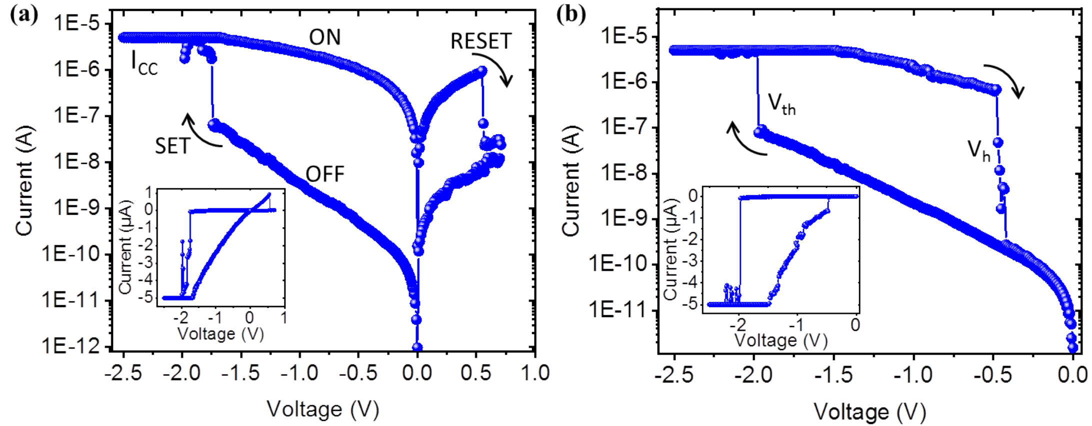

Figure A.2 (a) DC IV-sweep for a single CSNP featuring bipolar resistance switching behavior. The system switches from a high resistance state (OFF-state) to a low resistance state (ON-state) and vice versa at characteristic SET and RESET voltages, respectively. Inset: Same graph on a linear scale. (b) Unipolar threshold switching observed for a different CSNP device, where the ON-state is not maintained for small bias. The system switches from OFF to ON-states at critical threshold and hold voltages, V_{th} and V_h, respectively. Inset: Same data on a linear scale. Reprinted with permission from [167] © 2020 IEEE.

For electrical characterization, IDE samples were transferred to a vacuumed cryo probe-station setup (cf. section 5.6.2), equipped with a *Keithley 2635B* SMU. A typical two terminal current voltage measurement of a CSNP device showing bipolar memristive switching at room temperature is shown in Fig. A.2 (a). Performing a DC IV-sweep starting from 0 V to small negative bias, the system is initially in its high resistance state (OFF-state), only featuring a small, roughly exponentially increasing current. Going to higher negative voltages, an abrupt transition to a low resistance state (ON-state) is observed at -1.75 V. A compliance current I_{CC} of 5×10^{-6} A was set to protect the device from hard breakdown. This event corresponds to the SET process, indicated by a curved black arrow. Being in the ON-state, the system shows ohmic conduction when sweeping back to 0 V as can be seen by the nearly linear slope of the IV-curve in the inset. To reset the system, a small positive bias is applied subsequently with the RESET event occurring at 0.6 V as indicated by the other curved arrow. This way, the resistance of the device can be repeatedly switched between the ON and OFF-state. In total, six out of 15 investigated device structures featured such pronounced bipolar memristive switching behavior. Surprisingly in contrast, for four other devices unipolar threshold switching (TS) was observed, where the ON-state was not maintained for small bias as shown exemplarily in Fig. A.2 (b). The remaining five devices either showed irreversible breakthrough or only small currents in the pA range. IV characteristics featuring sharp transitions between ON and OFF-states, and either bipolar or threshold switching behavior, are indicative for electrochemical metallization cells (EMC) or valence change memories (VCM). They are in marked contrast

to the IV-characteristics usually observed in complementary resistance switches (CRS), which also feature a metal-oxide-metal-oxide-metal double layer structure as our CSNPs do [169, 170]. In such CRS devices, the OFF-state is always present for both, small and large bias. The ON-state however, is usually only observed in an intermediate voltage regime.

A.3 Stability of bipolar resistive switching

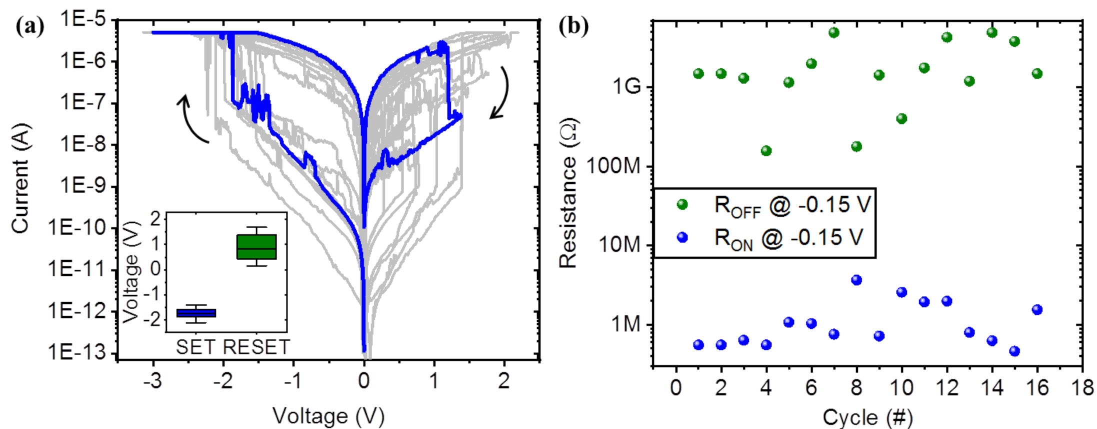

Figure A.3 (a) 20 DC IV-sweeps of a typical sample showing bipolar resistive switching in gray and a single sweep in blue color for clarity. A variation in OFF and ON-state conductance as well as in SET and RESET voltages can be observed as illustrated in more detail in the box chart in the inset showing mean values with standard deviations and outliers. (b) Zero bias resistance for OFF and ON-states (R_{OFF} and R_{ON}) vs. cycle number, of a single sample obtained by taking inverse values of slopes of linear fits of the IV-data for small voltages (0 V to −0.15 V). An OFF/ON-ratio of ~ 10^3 can be extracted. Reprinted with permission from [167] © 2020 IEEE.

In order to test for the stability and switching characteristics distribution of the observed bipolar memristive behavior, all corresponding devices were characterized systematically. Fig. A.3 (a) shows the measured data of a typical device featuring bipolar switching in gray and a single IV-sweep in blue color for clarity, with curved black arrows indicating the sweep direction. For all measurements, a sweep rate of 0.1 V/s and a step size of 10 mV was used consistently. Apparently, a significant spread of IV-traces and resistances in the OFF and ON-states can be observed. In addition, a rather broad distribution of RESET voltages can be identified, as illustrated in more detail in the box chart plot in the inset, showing mean values of SET and RESET voltages with standard deviations and outliers. We assign these deviations to a rather unstable contact between NP and Au contacts due to small contact areas. A typical sample could be switched up to ~15 times until irreversible breakdown occurred. Fig. A.3 (b) represents the respective zero bias resistance of OFF- (green dots) and ON-states (blue dots) of such a sample, obtained by taking the inverse values of slopes of linear fits in a range between 0 V to −0.15 V. On average, an OFF/ON resistance ratio of ~ 10^3 was determined for this specific sample.

A.4 Model for the switching mechanism

We assign the observed bistable switching mechanism to the reversible formation and rupture of Ag filaments in the NP SiO_x shell. To investigate the switching mechanism in this heterosystem, at first complementary finite element simulations of the electric potential and field distributions inside an IDE/CSNP device were conducted using the built-in static electric field tool in standard *Comsol* software. Fig. A.4 (a) shows a resulting excerpt of the electric field distribution of an IDE device, where the cut was taken in the middle of the particle at the exact position of the contact. In this image, the contact on the left side of the NP, the oxide shell as well as the Ag core can be clearly identified. To obtain the electric field distribution, a potential of 10 V was applied to the shown contact, while the contact on the right side was forced to ground (0 V, not shown). As apparent from the color scale ranging from white to red, all the voltage drops in the shell near the interface between NP and contact, featuring significant anisotropy and therefore large electric fields. This is ascribed to the small, point-like contact area which would potentially lead to preferred ion migration in this region. To validate this hypothesis, a tpyical device, which showed resistance switching as described in Fig. A.2, was centrally cut using an in-situ focused ion beam milling FIB/SEM cross-beam instrument (cf. section 4.5), after electrical characterization. This allowed for slowly cutting through the NP while simultaneously monitoring the milling progress. The milling process was stopped as soon as the middle of the particle was reached. Subsequently, the exposed face of the particle was examined in close detail under a tilt-angle of the sample stage of 54°. A typical CSNP after FIB-milling is shown in Fig. A.4 (b). Apparently, the p-Si substrate and the SiO_2 layer, the two Au contacts on the left and right as well as the Ag-core and SiO_x-shell of the NP can be clearly identified. In addition, areas of enhanced brightness are observed on the bottom right and left of the particle (indicated by arrow 1 and 2), being indicative for a material such as metal. In particular, bright areas within the oxide shell on both sides, exemplary marked by arrow 1, appear significantly brighter as compared to the rest of the shell. We assign these areas to spacially confined Ag-ion accumulation in the oxide shell that had occurred during device operation. Their positions correspond to the regions of locally enhanced electric field close to the contacts, as suggested by the simulation results presented in Fig. A.4 (a). In contrast, bright areas below the NP, indicated by arrow 2, may be attributed to residues of the Au contacts still present after ion milling, as they were covered by the particle.

A corresponding proposed model of Ag-ion migration in the NP shell is depicted in Fig. A.4 (c) to (f), with Fig. A.4 (c) schematically illustrating the CRS geometry including all relevant layers. In a first forming step, as shown in image Fig. A.4 (d), a positive bias $+V$ is applied to the upper contact with the electric field pointing towards the bottom contact. Due to the potential difference, Ag^+-ions (green dots) may migrate in the direction of the electric field through the Si oxide and are being neutralized as soon as they reach the bottom contact. As a consequence, Ag-atoms would accumulate at the bottom contact and a conductive filament (CF)

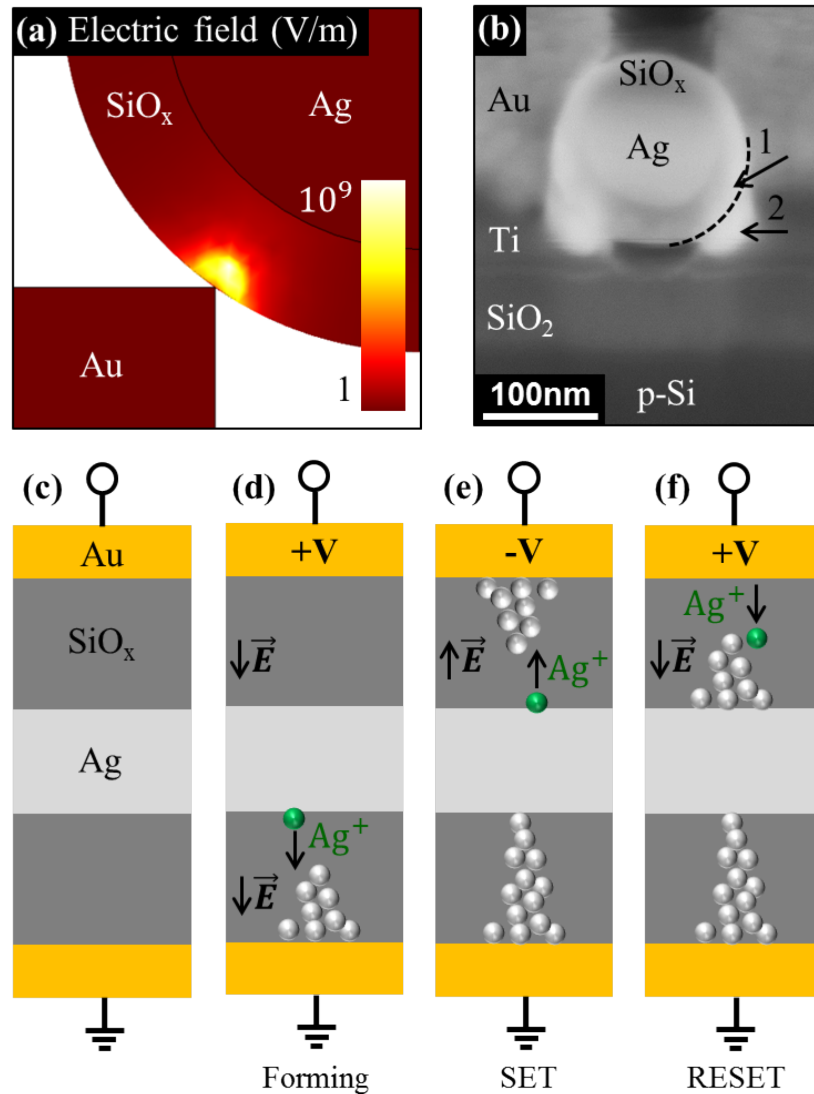

Figure A.4 (a) Excerpt of a cross-section of the electric field distribution inside a CSNP in contact with a Au line of an IDE device, simulated with *Comsol* software. A potential of 10 V is applied to the contact, with the electric field dropping from 7×10^8 V/m to 0 V/m across the NP oxide shell, as indicated by the color scale ranging from white to red, respectively. Strong local field enhancement close to the contact corner is observed. (b) Cross-sectional SEM image of a typical CSNP device after electrical operation and FIB milling. Distinct brighter areas inside (arrow 1) and below the oxide shell (arrow 2) can be identified, indicative for metals. (c) – (f) Schematic of a respective cross-section of a CSNP device, illustrating possible Ag ion migration in the oxide shell. After an initial forming step at positive bias, the core is connected to the ground contact. Subsequent filament formation and rupture is assumed to take place at the upper contact for SET and RESET operations, respectively. Reprinted with permission from [167] © 2020 IEEE.

grows towards the NP core. As soon as the CF reaches the core, bottom contact and core are at nearly equal potential. Hence, as illustrated in Fig. A.4 (e), applying a negative voltage ˇV, the potential mainly drops on the other side of the shell, leading to ion migration and therefore CF formation towards the upper contact. As soon as this second filament reaches the core,

both contacts are connected and current can flow with small resistance. This step corresponds to the SET process (compare Fig. A.2 (a)), yielding a sharp decrease in device resistance. To reset the device, a small positive bias is applied, leading to the reversal of ion migration and eventually to the rupture of the CF, as depicted in Fig. A.4 (f). It is worth mentioning, that for both SET and RESET operations after forming, it is assumed that the CF at the bottom contact remains stable, due to only very small potential drop along the CF. However, it cannot be fully excluded, that i) during SET, a small amount of Ag atoms is removed from the bottom contact and that ii) O^{2-}-ions may additionally contribute to Ag-CF instability. These are also possible explanations for the threshold switching being observed in the other devices, where either of the two CFs appears not to remain stable in the low-voltage regime. Another possible explanation for TS is the rupture of CFs due to Rayleigh instability leading to contraction of the CF to small spherical islands for small fields [145].

A.5 Summary

In summary, the formation of electrical contact to single core-shell Ag/SiOx nanoparticles of size 150 nm using interdigitated electrodes is reported. Two-terminal DC current voltage measurements under vacuum conditions revealed either pronounced, non-volatile bipolar memristive switching featuring OFF/ON ratios in excess of 10^3, or characteristic threshold switching behavior. A switching mechanism based on Ag conductive filaments contributing on both sides of the oxide shell of the NP is proposed. Asymmetric formation and rupture mainly of the Ag-CF in the shell just on one side of the Ag core is assumed during SET and RESET processes, depending on initialization (forming). Differences in forming dynamics and CF stability, which may originate from differences in electrode-CSNP contact resistance may be responsible for a certain system to reveal either of both resistive switching characteristics. This hypothesis is supported by electric field simulations which show critical, highly focused electric field enhancement close to the contact points.
For further improvement of device stability, contact formation via direct top-down lithographical processes to enhance the contact area and stability will be in the focus of future work. Another approach to reduce contact resistance variations would be to investigate different contact materials as well as employing and optimizing various annealing procedures. Complementary, spatially resolved energy dispersive X-ray diffraction elemental analysis of relevant NP cross-sections would allow for direct determination of material composition and shape of CFs in the oxide shell, to verify our conclusions. For further differentiating between EMC- and any possible, additional VCM-type origins of switching behavior, also temperature dependent studies of the ON-state conductivity shall be conducted, as well as electrical measurements in ambient.

B Side-selective coverage of SiNCs by metal evaporation

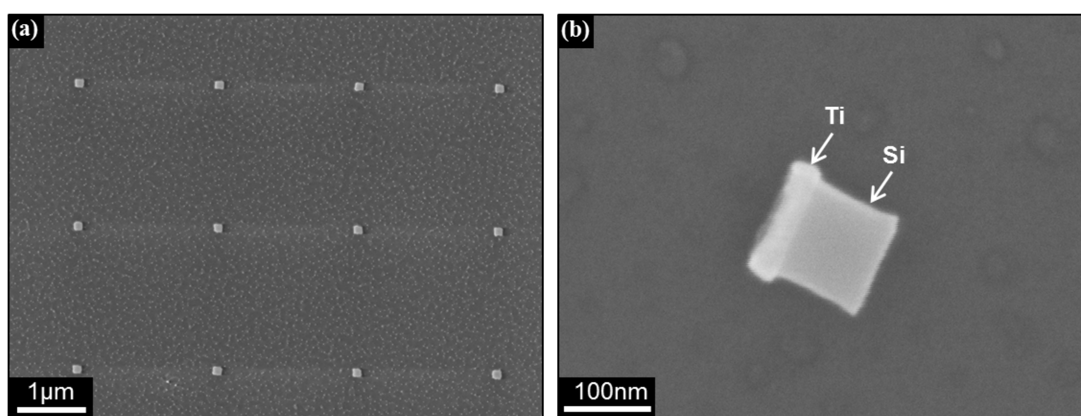

Figure B.1 (a) SiNC array fabricated by EBL and RIE after cleaning by 'piranha' solution. Clearly, homogeneous sized are obtained with a side-length of ~110 nm. (b) Typical SiNC taken from (a) after Ti evaporation (~25 nm) yielding side-specific SiNC coverage.

To generate more degrees of freedom for directed self-assembly of heterogeneous NP agglomerates, the side-selective coverage of SiNC top facets was demonstrated as a first proof of principle. Being able to tune the surface functionality or even the material of one or more sides of SiNCs would allow for addressing specific SiNC sides for directed binding of other NPs or surfaces onto respective sides during a self-assembly process. Hence, as a first step in this direction, the top facet of as prepared and cleaned SiNCs fabricated by EBL and RIE, as can be seen in Fig. B.1 (a) (cf. section 8.2), were covered by a thin layer of titanium (Ti) via evaporation (cf. section 4.1.3). Coverage of the top facet was investigated by under-etching of SiNCs by HF, dispersion of SiNCs by sonication in ethanol (~100 μL) and subsequent drop-casting and SEM imaging. A typical SiNC featuring a ~25 nm thick Ti layer is shown in the SEM image in Fig. B.1 (b), highlighted by a white arrow. Apparently, only the top facet and no other side is covered by Ti due to directional material deposition during the evaporation process. If all sides except the bottom one, which is in contact with the buried oxide layer of the SOI wafer and therefore not exposed, shall be covered by a specific material, ALD deposition could be employed (cf. section 4.1.1). However, if one or more of SiNC sides are supposed to be covered, evaporation under a tilt angle slightly smaller then 90° could be executed by mounting the SOI wafer chip accordingly onto the holder of the evaporation system.

C Self-assembly of 3D germanium-oxide-nanocube colloidal crystals

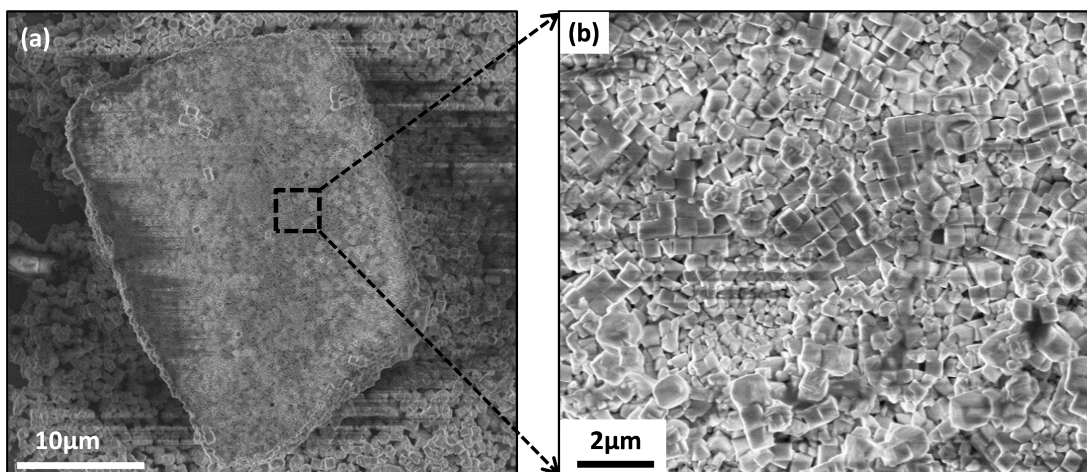

Figure C.1 (a) SEM image of a typical 3D GeO_xNC colloidal crystal featuring nearly rectangular shape and a size of several 10 nm, self-assembled using C12monoPA in EtOH. (b) Zoom-in SEM image of (a) revealing ordered crystalline domains of nanoparticles.

Chemically synthesized Germanium-oxide nanocubes (GeO_xNCs) with a side-length of (360 ± 100) nm [171] served as ideal platform to study self-assembly of 3D colloidal crystals in suspension, as these nanostructures are available in large amounts (several milligrams, provided by Dr. Morteza Javadi, Veinot group, department of chemistry, University of Alberta). Additionally, memristive switching in GeO_x layers has been shown, making them attractive for future studies [55].
The self-assembly process was executed as follows:

- 1 mg of GeO_xNC powder was cleaned and hydroxyl-activated by dispersion in basic 'piranha' solution for 5 min under constant sonication;

- GeO_xNCs were washed by centrifugation (5000 rpm) and re-dispersion in EtOH three-times;

- cleaned GeO_xNCs were surface functionalized and self-assembled in 1 mL EtOH and 1 mmol C12-mono-phosphonic-acid (C12monoPA) under constant agitation on an orbital shaker (250 rpm, >24 h);
- finally, GeO_xNCs were washed again in EtOH. Note that GeO_xNCs are only stable in polar solvents.

Following this surfactant-mediated self-assembly process, micrometer-sized, 3D aggregates of GeO_xNCs were assembled. During this process, SAMs of amphiphilic PA molecules render the surface of GeO_xNCs hydrophobic. Hence, in a polar solvent such as EtOH, hydrophobic interactions cause agglomerate formation. A typical 3D aggregate is shown in the SEM image in Fig. C.1 (a) featuring nearly rectangular shape reproducing GeO_xNC geometry. Typical aggregate sizes were in the range of (33.0 ± 9.6) µm. In addition, ordered microstructure is observed in these colloids, as illustrated in the zoom-in SEM image in Fig. C.1 (b), where ordered crystalline domains of GeO_xNCs are visible.

Bibliography

[1] G. E. Moore: Cramming more components onto integrated circuits, Reprinted from Electronics, volume 38, number 8, April 19, 1965, pp.114 ff. IEEE Solid-State Circuits Society Newsletter **11**(3) (2006), 33–35. DOI: 10.1109/N-SSC.2006.4785860 (cit. on p. 1).

[2] P. Sheridan, W. Ma, and W. Lu, eds.: *Pattern recognition with memristor networks.* IEEE, 2014. DOI: 10.1109/ISCAS.2014.6865326 (cit. on p. 1).

[3] Y. Li, Z. Wang, R. Midya, Q. Xia, and J. J. Yang: Review of memristor devices in neuromorphic computing: Materials sciences and device challenges. Journal of Physics D: Applied Physics **51**(50) (2018), 503002. DOI: 10.1088/1361-6463/aade3f (cit. on p. 1).

[4] J. P. Carbajal, J. Dambre, M. Hermans, and B. Schrauwen: Memristor Models for Machine Learning. Neural Computation **27**(3) (2015), 725–747. DOI: 10.1162/NECO_a_00694 (cit. on p. 1).

[5] G. W. Burr, R. M. Shelby, A. Sebastian, et al.: Neuromorphic computing using non-volatile memory. Advances in Physics: X **2**(1) (2017), 89–124. DOI: 10.1080/23746149.2016.1259585 (cit. on p. 2).

[6] Y. V. Pershin and M. Di Ventra: Neuromorphic, Digital, and Quantum Computation With Memory Circuit Elements. Proceedings of the IEEE **100**(6) (2012), 2071–2080. DOI: 10.1109/JPROC.2011.2166369 (cit. on p. 2).

[7] I. Valov, R. Waser, J. R. Jameson, and M. N. Kozicki: Electrochemical metallization memories—fundamentals, applications, prospects. Nanotechnology **22**(28) (2011), 289502. DOI: 10.1088/0957-4484/22/28/289502 (cit. on pp. 2, 8, 9, 60).

[8] Z. Wang, S. Joshi, S. E. Savel'ev, et al.: Memristors with diffusive dynamics as synaptic emulators for neuromorphic computing. Nature materials **16**(1) (2017), 101–108. DOI: 10.1038/nmat4756 (cit. on pp. 2, 55).

[9] F. Pan, S. Gao, C. Chen, C. Song, and F. Zeng: Recent progress in resistive random access memories: Materials, switching mechanisms, and performance. Materials Science and Engineering: R: Reports **83** (2014), 1–59. DOI: 10.1016/j.mser.2014.06.002 (cit. on pp. 2, 8).

[10] S. Menzel, U. Böttger, M. Wimmer, and M. Salinga: Physics of the Switching Kinetics in Resistive Memories. Advanced Functional Materials **25**(40) (2015), 6306–6325. DOI: 10.1002/adfm.201500825 (cit. on p. 2).

[11] S. Nau, C. Wolf, K. Popovic, A. Blümel, F. Santoni, A. Gagliardi, A. Di Carlo, S. Sax, and E. J. W. List-Kratochvil: Inkjet-Printed Resistive Switching Memory Based on Organic Dielectric Materials: From Single Elements to Array Technology. Advanced Electronic Materials **1**(1-2) (2015), 1400003. DOI: 10.1002/aelm.201400003 (cit. on p. 2).

[12] I. Boybat, M. Le Gallo, S. R. Nandakumar, T. Moraitis, T. Parnell, T. Tuma, B. Rajendran, Y. Leblebici, A. Sebastian, and E. Eleftheriou: Neuromorphic computing with multi-memristive synapses. Nature communications **9**(1) (2018), 2514. DOI: 10.1038/s41467-018-04933-y (cit. on p. 2).

[13] S. S. Iyer: Three-dimensional integration: An industry perspective. MRS Bulletin **40**(3) (2015), 225–232. DOI: 10.1557/mrs.2015.32 (cit. on p. 2).

[14] M. Koyanagi, T. Fukushima, K.-W. Lee, and T. Tanaka: Applications of three-dimensional LSI. MRS Bulletin **40**(3) (2015), 242–247. DOI: 10.1557/mrs.2015.33 (cit. on p. 2).

[15] H. Cong, B. Yu, J. Tang, Z. Li, and X. Liu: Current status and future developments in preparation and application of colloidal crystals. Chemical Society reviews **42**(19) (2013), 7774–7800. DOI: 10.1039/c3cs60078e (cit. on pp. 2, 5, 73).

[16] Z. Nie, A. Petukhova, and E. Kumacheva: Properties and emerging applications of self-assembled structures made from inorganic nanoparticles. Nature nanotechnology **5**(1) (2010), 15–25. DOI: 10.1038/nnano.2009.453 (cit. on pp. 2, 73).

[17] M. Rycenga, J. M. McLellan, and Y. Xia: Controlling the Assembly of Silver Nanocubes through Selective Functionalization of Their Faces. Advanced Materials **20**(12) (2008), 2416–2420. DOI: 10.1002/adma.200800360 (cit. on pp. 2, 5, 6).

[18] Q. Hua, H. Wu, B. Gao, M. Zhao, Y. Li, X. Li, X. Hou, M.-F. Marvin Chang, P. Zhou, and H. Qian: A Threshold Switching Selector Based on Highly Ordered Ag Nanodots for X-Point Memory Applications. Advanced science (Weinheim, Baden-Wurttemberg, Germany) **6**(10) (2019), 1900024. DOI: 10.1002/advs.201900024 (cit. on p. 2).

[19] Q. Liu, S. Long, H. Lv, W. Wang, J. Niu, Z. Huo, J. Chen, and M. Liu: Controllable growth of nanoscale conductive filaments in solid-electrolyte-based ReRAM by using a metal nanocrystal covered bottom electrode. ACS nano **4**(10) (2010), 6162–6168. DOI: 10.1021/nn1017582 (cit. on pp. 2, 56).

[20] B. K. You, J. M. Kim, D. J. Joe, K. Yang, Y. Shin, Y. S. Jung, and K. J. Lee: Reliable Memristive Switching Memory Devices Enabled by Densely Packed Silver Nanocone Arrays as Electric-Field Concentrators. ACS nano **10**(10) (2016), 9478–9488. DOI: 10.1021/acsnano.6b04578 (cit. on p. 2).

[21] F. Alibart, S. Pleutin, O. Bichler, C. Gamrat, T. Serrano-Gotarredona, B. Linares-Barranco, and D. Vuillaume: A Memristive Nanoparticle/Organic Hybrid Synapstor for Neuroinspired Computing. Advanced Functional Materials **22**(3) (2012), 609–616. DOI: 10.1002/adfm.201101935 (cit. on pp. 2, 47).

[22] E. J. Sandouk, J. K. Gimzewski, and A. Z. Stieg: Multistate resistive switching in silver nanoparticle films. Science and technology of advanced materials **16**(4) (2015), 45004. DOI: 10.1088/1468-6996/16/4/045004 (cit. on pp. 2, 47).

[23] J.-Y. Lee, Y.-J. Baek, Q. Hu, Y. Jin Choi, C. Jung Kang, H. H. Lee, H.-M. Kim, K.-B. Kim, and T.-S. Yoon: Multimode threshold and bipolar resistive switching in bi-layered Pt-Fe_2O_3 core-shell and Fe_2O_3 nanoparticle assembly. Applied Physics Letters **102**(12) (2013), 122111. DOI: 10.1063/1.4798534 (cit. on pp. 2, 47, 105).

[24] J. Kane, M. Inan, and R. F. Saraf: Self-assembled nanoparticle necklaces network showing single-electron switching at room temperature and biogating current by living microorganisms. ACS nano **4**(1) (2010), 317–323. DOI: 10.1021/nn901161w (cit. on pp. 2, 47).

[25] X.-Y. Xu, Z.-Y. Yin, C.-X. Xu, J. Dai, and J.-G. Hu: Resistive switching memories in MoS_2 nanosphere assemblies. Applied Physics Letters **104**(3) (2014), 33504. DOI: 10.1063/1.4862755 (cit. on p. 2).

[26] Y. Ko, H. Baek, Y. Kim, M. Yoon, and J. Cho: Hydrophobic nanoparticle-based nanocomposite films using in situ ligand exchange layer-by-layer assembly and their nonvolatile memory applications. ACS nano **7**(1) (2013), 143–153. DOI: 10.1021/nn3034524 (cit. on pp. 2, 6, 47, 105).

[27] G. M. Whitesides, J. K. Kriebel, and B. T. Mayers: VIII. Self-Assembly and Nanostructured Materials. Nanoscale Assembly. Ed. by W. T. S. Huck. Nanostructured Science and Technology. Springer US, 2005 (cit. on p. 5).

[28] J. Zhang, Y. Li, X. Zhang, and B. Yang: Colloidal self-assembly meets nanofabrication: from two-dimensional colloidal crystals to nanostructure arrays. Advanced materials (Deerfield Beach, Fla.) **22**(38) (2010), 4249–4269. DOI: 10.1002/adma.201000755 (cit. on p. 5).

[29] Q. Li, U. Jonas, X. S. Zhao, and M. Kappl: The forces at work in colloidal self-assembly: A review on fundamental interactions between colloidal particles. Asia-Pacific Journal of Chemical Engineering **3**(3) (2008), 255–268. DOI: 10.1002/apj.144 (cit. on p. 5).

[30] A. R. Tao, J. Huang, and P. Yang: Langmuir-Blodgettry of nanocrystals and nanowires. Accounts of chemical research **41**(12) (2008), 1662–1673. DOI: 10.1021/ar8000525 (cit. on p. 5).

[31] M. J. Shiers, R. Leech, C. J. Carmalt, I. P. Parkin, and A. J. Kenyon: Self-assembled ultra-high aspect ratio silver nanochains. Advanced materials (Deerfield Beach, Fla.) **24**(38) (2012), 5227–5235. DOI: 10.1002/adma.201202005 (cit. on p. 5).

[32] D. K. Yi, E.-M. Seo, and D.-Y. Kim: Fabrication of a Mesoscale Wire: Sintering of a Polymer Colloid Arrayed Inside a One-Dimensional Groove Pattern. Langmuir **18**(13) (2002), 5321–5323. DOI: 10.1021/la011565r (cit. on p. 5).

[33] N. Lämmerhardt, S. Merzsch, J. Ledig, A. Bora, A. Waag, M. Tornow, and P. Mischnick: Toward three-dimensional microelectronic systems: directed self-assembly of silicon microcubes via DNA surface functionalization. Langmuir : the ACS journal of surfaces and colloids **29**(26) (2013), 8410–8416. DOI: 10.1021/la401558f (cit. on pp. 5, 6, 72).

[34] N. Lämmerhardt: Selbstorganisation von Halbleiterbausteinen nach DNA-Funktionalisierung - ein Schritt auf dem Weg zu dreidimensionalen mikroelektronischen Systemen. Doctoral Thesis. Braunschweig: Technische Universität Carolo-Wilhelmina zu Braunschweig, 2015 (cit. on p. 5).

[35] H. Cong and W. Cao: Colloidal Crystallization Induced by Capillary Force. Langmuir **19**(20) (2003), 8177–8181. DOI: 10.1021/la0344480 (cit. on p. 6).

[36] Z. Quan, H. Xu, C. Wang, et al.: Solvent-mediated self-assembly of nanocube superlattices. Journal of the American Chemical Society **136**(4) (2014), 1352–1359. DOI: 10.1021/ja408250q (cit. on p. 6).

[37] Q.-Y. Lin, Z. Li, K. A. Brown, et al.: Strong Coupling between Plasmonic Gap Modes and Photonic Lattice Modes in DNA-Assembled Gold Nanocube Arrays. Nano letters **15**(7) (2015), 4699–4703. DOI: 10.1021/acs.nanolett.5b01548 (cit. on p. 6).

[38] H. Hu, M. Gopinadhan, and C. O. Osuji: Directed self-assembly of block copolymers: a tutorial review of strategies for enabling nanotechnology with soft matter. Soft matter **10**(22) (2014), 3867–3889. DOI: 10.1039/c3sm52607k (cit. on p. 6).

[39] A. Le Bris, F. Maloum, J. Teisseire, and F. Sorin: Self-organized ordered silver nanoparticle arrays obtained by solid state dewetting. Applied Physics Letters **105**(20) (2014), 203102. DOI: 10.1063/1.4901715 (cit. on p. 6).

[40] A. George, M. Knez, G. Hlawacek, D. Hagedoorn, H. H. J. Verputten, R. van Gastel, and J. E. t. Elshof: Nanoscale patterning of organosilane molecular thin films from the gas phase and its applications: fabrication of multifunctional surfaces and large area molecular templates for site-selective material deposition. Langmuir : the ACS journal of surfaces and colloids **28**(5) (2012), 3045–3052. DOI: 10.1021/la204437r (cit. on pp. 6, 27, 49).

[41] M. Speckbacher, M. Rinderle, W. Kaiser, E. A. Osman, D. Chryssikos, A. Cattani–Scholz, J. M. Gibbs, A. Gagliardi, and M. Tornow: Directed Assembly of Nanoparticle Threshold–Selector Arrays. Advanced Electronic Materials **5**(7) (2019), 1900098. DOI: 10.1002/aelm.201900098 (cit. on pp. 6, 27, 47–57, 59, 61, 62).

[42] S. Kinge, T. Gang, W. J. M. Naber, van der Wiel, Wilfred G, and D. N. Reinhoudt: Magnetic nanoparticle assembly on surfaces using click chemistry. Langmuir : the ACS journal of surfaces and colloids **27**(2) (2011), 570–574. DOI: 10.1021/la103715y (cit. on p. 6).

[43] Y. Xia, B. Gates, Y. Yin, and Y. Lu: Monodispersed Colloidal Spheres: Old Materials with New Applications. Advanced Materials **12**(10) (2000), 693–713 (cit. on p. 6).

[44] R. K. Grötsch, C. Wanzke, M. Speckbacher, A. Angı, B. Rieger, and J. Boekhoven: Pathway Dependence in the Fuel-Driven Dissipative Self-Assembly of Nanoparticles. Journal of the American Chemical Society **141**(25) (2019), 9872–9878. DOI: 10.1021/jacs.9b02004 (cit. on p. 6).

[45] S. Mühlig, A. Cunningham, S. Scheeler, C. Pacholski, T. Bürgi, C. Rockstuhl, and F. Lederer: Self-assembled plasmonic core-shell clusters with an isotropic magnetic dipole response in the visible range. ACS nano **5**(8) (2011), 6586–6592. DOI: 10.1021/nn201969h (cit. on pp. 6, 76).

[46] G. M. Whitesides and B. Grzybowski: Self-assembly at all scales. Science **295**(5564) (2002), 2418–2421. DOI: 10.1126/science.1070821 (cit. on p. 6).

[47] R. K. Grötsch, A. Angı, Y. G. Mideksa, C. Wanzke, M. Tena-Solsona, M. J. Feige, B. Rieger, and J. Boekhoven: Dissipative Self-Assembly of Photoluminescent Silicon Nanocrystals. Angewandte Chemie (International ed. in English) **57**(44) (2018), 14608–14612. DOI: 10.1002/anie.201807937 (cit. on p. 7).

[48] M. Speckbacher, D. Reiser, and J. M. Dlugosch: *Introduction to memristive devices laboratory*. München: Professur für Molekularelektronik, 2019 (cit. on p. 7).

[49] L. Chua: Memristor-The missing circuit element. IEEE Transactions on Circuit Theory **18**(5) (1971), 507–519. DOI: 10.1109/TCT.1971.1083337 (cit. on p. 7).

[50] D. B. Strukov, G. S. Snider, D. R. Stewart, and R. S. Williams: The missing memristor found. Nature **453**(7191) (2008), 80–83. DOI: 10.1038/nature06932 (cit. on p. 7).

[51] H.-S. P. Wong, H.-Y. Lee, S. Yu, Y.-S. Chen, Y. Wu, P.-S. Chen, B. Lee, F. T. Chen, and M.-J. Tsai: Metal–Oxide RRAM. Proceedings of the IEEE **100**(6) (2012), 1951–1970. DOI: 10.1109/JPROC.2012.2190369 (cit. on pp. 8, 9, 11).

[52] R. Waser, R. Bruchhaus, and S. Menzel: Redox-based Resistive Switching Memories. Nanoelectronics and information technology. Ed. by R. Waser. Weinheim, Germany: Wiley-VCH Verlag &Co. KGaA, 2012, 685–708 (cit. on pp. 8, 9).

[53] D. Ielmini and R. Waser, eds.: *Resistive switching: From fundamentals of nanionic redox processes to memristive device applications*. 1st ed. Weinheim: Wiley-VCH Verlag &Co. KGaA, 2016 (cit. on pp. 8, 9, 11).

[54] J. Zhou, K.-H. Kim, and W. Lu: Crossbar RRAM Arrays: Selector Device Requirements During Read Operation. IEEE Transactions on Electron Devices **61**(5) (2014), 1369–1376. DOI: 10.1109/TED.2014.2310200 (cit. on p. 9).

[55] O. N. Gorshkov, I. N. Antonov, A. I. Belov, A. P. Kasatkin, and A. N. Mikhaylov: Resistive switching in metal-insulator-metal structures based on germanium oxide and stabilized zirconia. Technical Physics Letters **40**(2) (2014), 101–103. DOI: 10.1134/S1063785014020084 (cit. on pp. 9, 115).

[56] R. Waser: Resistive non-volatile memory devices. Microelectronic Engineering **86**(7-9) (2009), 1925–1928. DOI: 10.1016/j.mee.2009.03.132 (cit. on p. 11).

[57] H.-S. P. Wong, S. Raoux, S. Kim, J. Liang, J. P. Reifenberg, B. Rajendran, M. Asheghi, and K. E. Goodson: Phase Change Memory. Proceedings of the IEEE **98**(12) (2010), 2201–2227. DOI: 10.1109/JPROC.2010.2070050 (cit. on p. 11).

[58] I. Langmuir: The constitution and fundamental properties of solids and liquids. II. Liquids. Journal of the American Chemical Society **39**(9) (1917), 1848–1906. DOI: 10.1021/ja02254a006 (cit. on pp. 11, 27).

[59] K. B. Blodgett: Films Built by Depositing Successive Monomolecular Layers on a Solid Surface. Journal of the American Chemical Society **57**(6) (1935), 1007–1022. DOI: 10.1021/ja01309a011 (cit. on pp. 11, 27).

[60] F. Schreiber: Structure and growth of self-assembling monolayers. Progress in Surface Science **65** (2000), 151–256. DOI: 10.1016/S0079-6816(00)00024-1 (cit. on pp. 11, 27, 49).

[61] G. Witte and C. Wöll: Growth of aromatic molecules on solid substrates for applications in organic electronics. Journal of Materials Research **19**(7) (2004), 1889–1916. DOI: 10.1557/JMR.2004.0251 (cit. on pp. 11, 27).

[62] C. D. Bain, E. B. Troughton, Y. T. Tao, J. Evall, G. M. Whitesides, and R. G. Nuzzo: Formation of monolayer films by the spontaneous assembly of organic thiols from solution onto gold. J. Am. Chem. Soc. **111**(1) (1989), 321–335. DOI: 10.1021/ja00183a049 (cit. on pp. 11, 40, 94).

[63] B. Voigtländer, S. Karthäuser, S. N. Filimonov, and S. L. Tait: Bottom-Up Approaches by Self-Organization Techniques. Nanoelectronics and information technology. Ed. by R. Waser. Weinheim, Germany: Wiley-VCH Verlag &Co. KGaA, 2012, 305–319 (cit. on p. 11).

[64] M. Dasog, J. Kehrle, B. Rieger, and J. G. C. Veinot: Silicon Nanocrystals and Silicon-Polymer Hybrids: Synthesis, Surface Engineering, and Applications. Angewandte Chemie (International ed. in English) **55**(7) (2016), 2322–2339. DOI: 10.1002/anie.201506065 (cit. on pp. 11, 21, 73, 85).

[65] T. Franklin and B. Steven L., eds.: *Functionalization of semiconductor surfaces*. Hoboken, New Jersey: John Wiley & Sons, Inc, 2012 (cit. on p. 11).

[66] A. Cattani-Scholz, D. Pedone, M. Dubey, S. Neppl, B. Nickel, P. Feulner, J. Schwartz, G. Abstreiter, and M. Tornow: Organophosphonate-based PNA-functionalization of silicon nanowires for label-free DNA detection. ACS nano **2**(8) (2008), 1653–1660. DOI: 10.1021/nn800136e (cit. on p. 11).

[67] B. Mann and H. Kuhn: Tunneling through Fatty Acid Salt Monolayers. Journal of Applied Physics **42**(11) (1971), 4398–4405. DOI: 10.1063/1.1659785 (cit. on p. 12).

[68] D. K. Aswal, S. Lenfant, D. Guerin, J. V. Yakhmi, and D. Vuillaume: Self assembled monolayers on silicon for molecular electronics. Analytica chimica acta **568**(1-2) (2006), 84–108. DOI: 10.1016/j.aca.2005.10.027 (cit. on pp. 12, 14, 15, 27).

[69] H. B. Akkerman and B. d. Boer: Electrical conduction through single molecules and self-assembled monolayers. Journal of Physics: Condensed Matter **20**(1) (2008), 13001. DOI: 10.1088/0953-8984/20/01/013001 (cit. on pp. 12, 14, 97).

[70] X. D. Cui, A. Primak, X. Zarate, J. Tomfohr, O. F. Sankey, A. L. Moore, T. A. Moore, D. Gust, G. Harris, and S. M. Lindsay: Reproducible Measurement of Single-Molecule Conductivity. Science **294**(5542) (2001), 571–574. DOI: 10.1126/science.1064354 (cit. on p. 13).

[71] B. Xu and N. J. Tao: Measurement of Single-Molecule Resistance by Repeated Formation of Molecular Junctions. Science **301**(5637) (2003), 1221–1223. DOI: 10.1126/science.1087481 (cit. on p. 13).

[72] N. P. Guisinger, M. E. Greene, R. Basu, A. S. Baluch, and M. C. Hersam: Room Temperature Negative Differential Resistance through Individual Organic Molecules on Silicon Surfaces. Nano letters **4**(1) (2004), 55–59. DOI: 10.1021/nl0348589 (cit. on p. 13).

[73] A. Vezzoli, R. J. Brooke, N. Ferri, S. J. Higgins, W. Schwarzacher, and R. J. Nichols: Single-Molecule Transport at a Rectifying GaAs Contact. Nano letters **17**(2) (2017), 1109–1115. DOI: 10.1021/acs.nanolett.6b04663 (cit. on p. 13).

[74] D. J. Wold and C. D. Frisbie: Formation of metal-molecule-metal tunnel junctions: microcontacts to alkanethiol monolayers with a conducting AFM tip. Journal of the American Chemical Society **122** (2000), 2970–2971. DOI: 10.1021/ja994468h (cit. on p. 13).

[75] M. A. Reed, C. Zhou, C. J. Muller, T. P. Burgin, and J. M. Tour: Conductance of a molecular junction. Science **278** (1997), 252–254. DOI: 10.1126/science.278.5336.252 (cit. on p. 13).

[76] C. J. Muller, J. M. van Ruitenbeek, and de Jongh L.J.: Experimental observation of the transition from weak link to tunnel junction. Physica C: Superconductivity **191**(3-4) (1992), 485–504. DOI: 10.1016/0921-4534(92)90947-B (cit. on p. 13).

[77] J. C. Love, L. A. Estroff, J. K. Kriebel, R. G. Nuzzo, and G. M. Whitesides: Self-assembled monolayers of thiolates on metals as a form of nanotechnology. Chemical reviews **105**(4) (2005), 1103–1169. DOI: 10.1021/cr0300789 (cit. on pp. 13, 43).

[78] A. Pathak, A. Bora, K.-C. Liao, H. Schmolke, A. Jung, C.-P. Klages, J. Schwartz, and M. Tornow: Disorder-derived, strong tunneling attenuation in bis-phosphonate monolayers. Journal of physics. Condensed matter : an Institute of Physics journal **28**(9) (2016), 94008. DOI: 10.1088/0953-8984/28/9/094008 (cit. on pp. 13, 43, 97).

[79] Y. Selzer, A. Salomon, and D. Cahen: Effect of Molecule−Metal Electronic Coupling on Through-Bond Hole Tunneling across Metal−Organic Monolayer−Semiconductor Junctions. Journal of the American Chemical Society **124**(12) (2002), 2886–2887. DOI: 10.1021/ja0177511 (cit. on p. 13).

[80] A. Bora, A. Pathak, K.-C. Liao, M. I. Vexler, A. Kuligk, A. Cattani-Scholz, B. Meinerzhagen, G. Abstreiter, J. Schwartz, and M. Tornow: Organophosphonates as model system for studying electronic transport through monolayers on SiO_2/Si surfaces. Applied Physics Letters **102**(24) (2013), 241602. DOI: 10.1063/1.4811441 (cit. on pp. 13, 14, 97).

[81] M. Baghbanzadeh, C. M. Bowers, D. Rappoport, et al.: Anomalously Rapid Tunneling: Charge Transport across Self-Assembled Monolayers of Oligo(ethylene glycol). Journal of the American Chemical Society **139**(22) (2017), 7624–7631. DOI: 10.1021/jacs.7b02770 (cit. on p. 13).

[82] L. Yuan, R. Breuer, L. Jiang, M. Schmittel, and C. A. Nijhuis: A Molecular Diode with a Statistically Robust Rectification Ratio of Three Orders of Magnitude. Nano letters **15**(8) (2015), 5506–5512. DOI: 10.1021/acs.nanolett.5b02014 (cit. on p. 13).

[83] J. G. Kushmerick, D. B. Holt, J. C. Yang, J. Naciri, M. H. Moore, and R. Shashidhar: Metal-molecule contacts and charge transport across monomolecular layers: measurement and theory. Physical Review Letters **89**(8) (2002), 86802. DOI: 10.1103/PhysRevLett.89.086802 (cit. on p. 13).

[84] K. B. Saller, H. Riedl, P. Lugli, G. Koblmüller, and M. Tornow: One-step transfer printing of patterned nanogap electrodes. Journal of Vacuum Science & Technology B **37**(4) (2019), 40602. DOI: 10.1116/1.5100560 (cit. on p. 13).

[85] S. Pfaehler, K. Keim, R. Csiki, Q. H. Nguyen, K.-C. Liao, M. Stutzmann, J. Schwartz, A. Cattani-Scholz, and M. Tornow, eds.: *A nanogap electrode platform for organic monolayer-film devices*. IEEE, 2016. DOI: 10.1109/NANO.2016.7751507 (cit. on p. 13).

[86] T. Haeberle, A. Pathak, A. Bora, M. Tornow, P. Lugli, and J. Schwartz, eds.: *High-yield metal transfer printing on alkyl bis-phosphonate monolayers*. IEEE, 2015. DOI: 10.1109/NANO.2015.7485973 (cit. on p. 13).

[87] A. Bezryadin, C. Dekker, and G. Schmid: Electrostatic trapping of single conducting nanoparticles between nanoelectrodes. Applied Physics Letters **71**(9) (1997), 1273–1275. DOI: 10.1063/1.119871 (cit. on p. 13).

[88] S. M. Luber, S. Strobel, H.-P. Tranitz, W. Wegscheider, D. Schuh, and M. Tornow: Nanometre spaced electrodes on a cleaved AlGaAs surface. Nanotechnology **16**(8) (2005), 1182–1185. DOI: 10.1088/0957-4484/16/8/034 (cit. on p. 13).

[89] S. Strobel, R. M. Hernández, A. G. Hansen, and M. Tornow: Silicon based nanogap device for studying electrical transport phenomena in molecule-nanoparticle hybrids. Journal of physics. Condensed matter : an Institute of Physics journal **20**(37) (2008), 374126. DOI: 10.1088/0953-8984/20/37/374126 (cit. on p. 13).

[90] T. Diederichs, Q. H. Nguyen, M. Urban, R. Tampé, and M. Tornow: Transparent Nanopore Cavity Arrays Enable Highly Parallelized Optical Studies of Single Membrane Proteins on Chip. Nano letters **18**(6) (2018), 3901–3910. DOI: 10.1021/acs.nanolett.8b01252 (cit. on p. 13).

[91] A. Köhler and H. Bässler: *Electronic processes in organic semiconductors: An introduction.* Weinheim: Wiley-VCH Verlag &Co. KGaA, 2015 (cit. on p. 14).

[92] P. Stallinga: *Electrical characterization of organic electronic materials and devices.* 1st ed. Chichester, West Sussex, United Kingdom: John Wiley & Sons, Ltd, 2009 (cit. on p. 14).

[93] A. Vilan: Analyzing Molecular Current-Voltage Characteristics with the Simmons Tunneling Model: Scaling and Linearization. The Journal of Physical Chemistry C **111**(11) (2007), 4431–4444. DOI: 10.1021/jp066846s (cit. on p. 15).

[94] J. G. Simmons: Generalized Formula for the Electric Tunnel Effect between Similar Electrodes Separated by a Thin Insulating Film. Journal of Applied Physics **34**(6) (1963), 1793–1803. DOI: 10.1063/1.1702682 (cit. on p. 15).

[95] C. W. Tornøe, C. Christensen, and M. Meldal: Peptidotriazoles on Solid Phase: [1,2,3]-Triazoles by Regiospecific Copper(I)-Catalyzed 1,3-Dipolar Cycloadditions of Terminal Alkynes to Azides. The Journal of Organic Chemistry **67**(9) (2002), 3057–3064. DOI: 10.1021/jo011148j (cit. on pp. 16, 98).

[96] V. D. Bock, H. Hiemstra, and J. H. van Maarseveen: CuI-Catalyzed Alkyne-Azide "Click" Cycloadditions from a Mechanistic and Synthetic Perspective. European Journal of Organic Chemistry **2006**(1) (2006), 51–68. DOI: 10.1002/ejoc.200500483 (cit. on pp. 16, 51).

[97] H. C. Kolb, M. G. Finn, and K. B. Sharpless: Click Chemistry: Diverse Chemical Function from a Few Good Reactions. Angewandte Chemie International Edition **40**(11) (2001), 1433–7851. DOI: 10.1002/1521-3773(20010601)40:112004::AID-ANIE20043.0.CO;2-5 (cit. on pp. 16, 98).

[98] M. Meldal and C. W. Tornøe: Cu-catalyzed azide-alkyne cycloaddition. Chemical reviews **108**(8) (2008), 2952–3015. DOI: 10.1021/cr0783479 (cit. on pp. 16, 51).

[99] R. Huisgen, G. Szeimies, and L. Moebius: 1.3-Dipolare Cycloadditionen, XXXII. Kinetik der Additionen organischer Azide an CC-Mehrfachbindungen. Chemische Berichte **100** (1967), 2494–2507. DOI: 10.1002/cber.19671000806 (cit. on pp. 16, 51).

[100] K. V. Gothelf and K. A. Jørgensen: Asymmetric 1,3-Dipolar Cycloaddition Reactions. Chemical reviews **98** (1998), 863–909. DOI: 10.1021/cr970324e (cit. on p. 16).

[101] P. Appukkuttan, W. Dehaen, V. V. Fokin, and E. van der Eycken: A microwave-assisted click chemistry synthesis of 1,4-disubstituted 1,2,3-triazoles via a copper(I)-catalyzed three-component reaction. Organic letters **6**(23) (2004), 4223–4225. DOI: 10.1021/ol048341v (cit. on p. 16).

[102] M. S. Azam, S. L. Fenwick, and J. M. Gibbs-Davis: Orthogonally reactive SAMs as a general platform for bifunctional silica surfaces. Langmuir : the ACS journal of surfaces and colloids **27**(2) (2011), 741–750. DOI: 10.1021/la1041647 (cit. on pp. 17, 27, 51, 96, 97).

[103] K. E. Sickafus: Introduction to the kinetic Monte Carlo method. Radiation Effects in Solids. Ed. by A. F. Voter. Los Alamos, USA, 2007, 1–23 (cit. on p. 18).

[104] H. Baessler: Charge Transport in Disordered Organic Photoconductors a Monte Carlo Simulation Study. physica status solidi b **175**(1) (1993), 15–56. DOI: 10.1002/pssb.2221750102 (cit. on p. 18).

[105] M. Jakob, M. Javadi, J. G. C. Veinot, A. Meldrum, A. Kartouzian, and U. Heiz: Ensemble Effects in the Temperature-Dependent Photoluminescence of Silicon Nanocrystals. Chemistry (Weinheim an der Bergstrasse, Germany) **25**(12) (2019), 3061–3067. DOI: 10.1002/chem.201804986 (cit. on pp. 21, 76).

[106] R. W. Johnson, A. Hultqvist, and S. F. Bent: A brief review of atomic layer deposition: From fundamentals to applications. Materials Today **17**(5) (2014), 236–246. DOI: 10.1016/j.mattod.2014.04.026 (cit. on p. 25).

[107] S. M. George: Atomic layer deposition: an overview. Chemical reviews **110**(1) (2010), 111–131. DOI: 10.1021/cr900056b (cit. on p. 25).

[108] S. Franssila: *Introduction to microfabrication*. 2nd ed. Chennai, India: John Wiley & Sons, Ltd, 2010 (cit. on pp. 26, 28, 29).

[109] E. L. Hanson, J. Schwartz, B. Nickel, N. Koch, and M. F. Danisman: Bonding self-assembled, compact organophosphonate monolayers to the native oxide surface of silicon. Journal of the American Chemical Society **125**(51) (2003), 16074–16080. DOI: 10.1021/ja035956z (cit. on p. 27).

[110] G.-J. Zhang, T. Tanii, T. Zako, T. Hosaka, T. Miyake, Y. Kanari, T. Funatsu, and I. Ohdomari: Nanoscale patterning of protein using electron beam lithography of organosilane self-assembled monolayers. Small (Weinheim an der Bergstrasse, Germany) **1**(8-9) (2005), 833–837. DOI: 10.1002/smll.200500091 (cit. on pp. 27, 49).

[111] V. M. Donnelly and A. Kornblit: Plasma etching: Yesterday, today, and tomorrow. Journal of Vacuum Science & Technology A: Vacuum, Surfaces, and Films **31**(5) (2013), 50825. DOI: 10.1116/1.4819316 (cit. on p. 28).

[112] M. Shearn, Sun, Xiankai, Henry, David, A. Yariv, and A. Scherer, eds.: *Advanced Plasma Processing: Etching, Deposition, and Wafer Bonding Techniques for Semiconductor Applications*. 1st ed. IntechOpen, 2010. DOI: 10.5772/8564 (cit. on p. 28).

[113] J. Moers and S. Okazaki: Advanced Optical and Particle Beam Lithography. Nanoelectronics and information technology. Ed. by R. Waser. Weinheim, Germany: Wiley-VCH Verlag &Co. KGaA, 2012, 201–216 (cit. on pp. 29, 30).

[114] D. F. Kyser and N. S. Viswanathan: Monte Carlo simulation of spatially distributed beams in electron–beam lithography. Journal of Vacuum Science and Technology **12**(6) (1975), 1305–1308. DOI: 10.1116/1.568524 (cit. on p. 30).

[115] M. Razeghi: *Fundamentals of solid state engineering*. 3rd ed. New York: Springer -Verlag, 2009 (cit. on p. 30).

[116] M. Speckbacher, E. A. Osman, J. M. Gibbs, and M. Tornow, eds.: *Directed self-assembly of silicon nanocubes fabricated by nano imprint-lithography.* Piscataway, NJ: IEEE, 2018. doi: 10.1109/NANO.2018.8626349 (cit. on pp. 31, 72, 77, 85, 89, 90, 92, 97, 98, 105).

[117] M. D. Austin, H. Ge, W. Wu, M. Li, Z. Yu, D. Wasserman, S. A. Lyon, and S. Y. Chou: Fabrication of 5nm linewidth and 14nm pitch features by nanoimprint lithography. Applied Physics Letters **84**(26) (2004), 5299–5301. doi: 10.1063/1.1766071 (cit. on p. 31).

[118] W. Wu: Nanoimprint Lithography. Nanoelectronics and information technology. Ed. by R. Waser. Weinheim, Germany: Wiley-VCH Verlag &Co. KGaA, 2012, 221–229 (cit. on p. 31).

[119] H. Schift: Nanoimprint lithography: An old story in modern times? A review. Journal of Vacuum Science & Technology B: Microelectronics and Nanometer Structures **26**(2) (2008), 458. doi: 10.1116/1.2890972 (cit. on p. 31).

[120] S. Y. Chou: Nanoimprint lithography. Journal of Vacuum Science & Technology B: Microelectronics and Nanometer Structures **14**(6) (1996), 4129. doi: 10.1116/1.588605 (cit. on p. 31).

[121] J. Haisma, M. Verheijen, K. van der Heuvel, and J. van den Berg: Mold-assisted nanolithography: A process for reliable pattern replication. Journal of Vacuum Science & Technology B: Microelectronics and Nanometer Structures **14**(6) (1996), 4124–4128. doi: 10.1116/1.588604 (cit. on p. 31).

[122] A. Stierle, H.-D. Carstanjen, S. Hofmann, and Seek, Oliver, H.: Structural and Chemical Characterization on the Nanoscale. Nanoelectronics and information technology. Ed. by R. Waser. Weinheim, Germany: Wiley-VCH Verlag &Co. KGaA, 2012, 235–252 (cit. on pp. 35, 36, 39).

[123] G. Binnig, C. F. Quate, and and Ch. Gerber: Atomic Force Microscope. Physical Review Letters **56**(9) (1986), 930–934. doi: 10.1103/PhysRevLett.56.930 (cit. on p. 37).

[124] P. Ebert and K. Szot: Scanning Probe Analysis. Nanoelectronics and information technology. Ed. by R. Waser. Weinheim, Germany: Wiley-VCH Verlag &Co. KGaA, 2012, 257–279 (cit. on pp. 37, 41).

[125] D. Sarid: Review of scanning force microscopy. Journal of Vacuum Science & Technology B: Microelectronics and Nanometer Structures **9**(2) (1991), 431–437. doi: 10.1116/1.585585 (cit. on p. 37).

[126] L. G. Rosa and J. Liang: Atomic force microscope nanolithography: dip-pen, nanoshaving, nanografting, tapping mode, electrochemical and thermal nanolithography. Journal of physics. Condensed matter : an Institute of Physics journal **21**(48) (2009), 483001. doi: 10.1088/0953-8984/21/48/483001 (cit. on p. 39).

[127] J. F. Watts and J. Wolstenholme: *An introduction to surface analysis by XPS and AES.* New York: Wiley-Interscience, 2005 (cit. on p. 39).

[128] C. D. Wagner, W. M. Riggs, L. E. Davis, J. F. Moulder, and G. E. Muilenberg: *Handbook of X-ray photoelectron spectroscopy. A reference book of standard data for use in X-ray photoelectron spectroscopy.* Eden Prairie, Minnesota, USA: Perkin-Elmer Corporation, 1979 (cit. on pp. 39, 96).

[129] M. Paszkiewicz and F. Allegretti: Electron spectroscopy of surfaces. Elemental and chemical analysis with X-ray photoelectron spectroscopy. Userguide F-Praktikum in den Bachelor- und Masterstudiengangen. München: Physik Department, Technische Universität München, 1.02.2018 (cit. on p. 40).

[130] M. A. A. Rasheed, ed.: *Mueller-matrix ellipsometry: a review*. Society of Photo-Optical Instrumentation Engineers, 1997. DOI: 10.1117/12.283870 (cit. on p. 40).

[131] H. Lee, H. Kim, T. N. Van, D.-W. Kim, and J. Y. Park: Nanoscale resistive switching Schottky contacts on self-assembled Pt nanodots on $SrTiO_3$. ACS applied materials & interfaces **5**(22) (2013), 11668–11672. DOI: 10.1021/am4032086 (cit. on p. 47).

[132] J. W. E. McCafferty: An X-ray photoelectron spectroscopy sputter profile study of the native air-formed oxide film of titanium. Applied Surface Science **143** (1999), 92–100 (cit. on pp. 48, 57).

[133] A. Andrieux-Ledier, B. Tremblay, and A. Courty: Stability of self-ordered thiol-coated silver nanoparticles: oxidative environment effects. Langmuir : the ACS journal of surfaces and colloids **29**(43) (2013), 13140–13145. DOI: 10.1021/la402916b (cit. on p. 51).

[134] C. H. Moran, M. Rycenga, Q. Zhang, and Y. Xia: Replacement of Poly(vinyl pyrrolidone) by Thiols: A Systematic Study of Ag Nanocube Functionalization by Surface-Enhanced Raman Scattering. The journal of physical chemistry. C, Nanomaterials and interfaces **115**(44) (2011), 21852–21857. DOI: 10.1021/jp207868a (cit. on pp. 51, 76).

[135] J. Albadi, M. Keshavarz, F. Shirini, and M. Vafaie-nezhad: Copper iodide nanoparticles on poly(4-vinyl pyridine): A new and efficient catalyst for multicomponent click synthesis of 1,4-disubstituted-1,2,3-triazoles in water. Catalysis Communications **27** (2012), 17–20. DOI: 10.1016/j.catcom.2012.05.023 (cit. on p. 51).

[136] Y. Yin, Y. Lu, B. Gates, and Y. Xia: Template-Assisted Self-Assembly: A Practical Route to Complex Aggregates of Monodispersed Colloids with Well-Defined Sizes, Shapes, and Structures. Journal of the American Chemical Society **123**(36) (2001), 8718–8729. DOI: 10.1021/ja011048v (cit. on p. 52).

[137] Z. Wang, M. Rao, R. Midya, et al.: Threshold Switching of Ag or Cu in Dielectrics: Materials, Mechanism, and Applications. Advanced Functional Materials **28**(6) (2018), 1704862. DOI: 10.1002/adfm.201704862 (cit. on pp. 55, 58).

[138] A. Bricalli, E. Ambrosi, M. Laudato, M. Maestro, R. Rodriguez and D. Ielmini: *2016 International Electron Devices Meeting: Technical digest*. Piscataway, NJ: IEEE, 2016 (cit. on pp. 55, 58).

[139] H. Sun, Q. Liu, C. Li, S. Long, H. Lv, C. Bi, Z. Huo, L. Li, and M. Liu: Direct Observation of Conversion Between Threshold Switching and Memory Switching Induced by Conductive Filament Morphology. Advanced Functional Materials **24**(36) (2014), 5679–5686. DOI: 10.1002/adfm.201401304 (cit. on p. 55).

[140] J. Song, J. Woo, A. Prakash, D. Lee, and H. Hwang: Threshold Selector With High Selectivity and Steep Slope for Cross-Point Memory Array. IEEE Electron Device Letters **36**(7) (2015), 681–683. DOI: 10.1109/LED.2015.2430332 (cit. on pp. 55, 57).

[141] J. Yoo, J. Woo, J. Song, and H. Hwang: Threshold switching behavior of Ag-Si based selector device and hydrogen doping effect on its characteristics. AIP Advances **5**(12) (2015), 127221. DOI: 10.1063/1.4938548 (cit. on pp. 55, 57).

[142] R. Midya, Z. Wang, J. Zhang, et al.: Anatomy of Ag/Hafnia-Based Selectors with 10^{10} Nonlinearity. Advanced materials (Deerfield Beach, Fla.) **29**(12) (2017). DOI: 10.1002/adma.201604457 (cit. on p. 55).

[143] G. M. Crouch, D. Han, S. K. Fullerton-Shirey, D. B. Go, and P. W. Bohn: Addressable Direct-Write Nanoscale Filament Formation and Dissolution by Nanoparticle-Mediated Bipolar Electrochemistry. ACS nano **11**(5) (2017), 4976–4984. DOI: 10.1021/acsnano.7b01657 (cit. on p. 56).

[144] Jeonghwan Song, Jiyong Woo, A. Prakash, Daeseok Lee, and Hyunsang Hwang: Threshold Selector With High Selectivity and Steep Slope for Cross-Point Memory Array. IEEE Electron Device Letters **36**(7) (2015), 681–683. DOI: 10.1109/LED.2015.2430332 (cit. on p. 58).

[145] C.-P. Hsiung, H.-W. Liao, J.-Y. Gan, T.-B. Wu, J.-C. Hwang, F. Chen, and M.-J. Tsai: Formation and instability of silver nanofilament in Ag-based programmable metallization cells. ACS nano **4**(9) (2010), 5414–5420. DOI: 10.1021/nn1010667 (cit. on pp. 58, 66, 80, 111).

[146] S. Dirkmann, M. Ziegler, M. Hansen, H. Kohlstedt, J. Trieschmann, and T. Mussenbrock: Kinetic simulation of filament growth dynamics in memristive electrochemical metallization devices. Journal of Applied Physics **118**(21) (2015), 214501. DOI: 10.1063/1.4936107 (cit. on pp. 58, 60).

[147] D. Li, M. Li, F. Zahid, J. Wang, and H. Guo: Oxygen vacancy filament formation in TiO_2: A kinetic Monte Carlo study. Journal of Applied Physics **112**(7) (2012), 73512. DOI: 10.1063/1.4757584 (cit. on pp. 58, 60).

[148] S. Qin, Z. Liu, G. Zhang, J. Zhang, Y. Sun, H. Wu, H. Qian, and Z. Yu: Atomistic study of dynamics for metallic filament growth in conductive-bridge random access memory. Physical chemistry chemical physics : PCCP **17**(14) (2015), 8627–8632. DOI: 10.1039/c4cp04903a (cit. on pp. 58, 61).

[149] J. R. Jameson, N. Gilbert, F. Koushan, J. Saenz, J. Wang, S. Hollmer, and M. Kozicki: Effects of cooperative ionic motion on programming kinetics of conductive-bridge memory cells. Applied Physics Letters **100**(2) (2012), 23505. DOI: 10.1063/1.3675870 (cit. on p. 58).

[150] W. Zhang, Y. Liu, D. Zhou, H. Wang, W. Liang, and F. Yang: Fast diffusion of silver in TiO_2 nanotube arrays. Beilstein journal of nanotechnology **7** (2016), 1129–1140. DOI: 10.3762/bjnano.7.105 (cit. on p. 59).

[151] W. Kaiser, J. Popp, M. Rinderle, T. Albes, and A. Gagliardi: Generalized Kinetic Monte Carlo Framework for Organic Electronics. Algorithms **11**(4) (2018), 37. DOI: 10.3390/a11040037 (cit. on pp. 60, 61).

[152] Y. Yang, P. Sheridan, and W. Lu: Complementary resistive switching in tantalum oxide-based resistive memory devices. Applied Physics Letters **100**(20) (2012), 203112. DOI: 10.1063/1.4719198 (cit. on pp. 66, 80).

[153] Z. Wang, U. Helmersson, and P.-O. Käll: Optical properties of anatase TiO_2 thin films prepared by aqueous sol–gel process at low temperature. Thin Solid Films **405**(1-2) (2002), 50–54. DOI: 10.1016/S0040-6090(01)01767-9 (cit. on p. 67).

[154] A. I. Kingon, J.-P. Maria, and S. K. Streiffer: Alternative dielectrics to silicon dioxide for memory and logic devices. Nature **406** (2000), 1032–1038. DOI: 10.1038/35023243 (cit. on pp. 67, 69).

[155] S. A. Campbell, D. C. Gilmer, X.-C. Wang, M.-T. Hsieh, H.-S. Kim, W. L. Gladfelter, and J. Yan: MOSFET transistors fabricated with high permitivity TiO_2 dielectrics. IEEE Transactions on Electron Devices **44**(1) (1997), 104–109. DOI: 10.1109/16.554800 (cit. on p. 67).

[156] M. Speckbacher, M. Jakob, M. Döblinger, J. G. C. Veinot, A. Kartouzian, U. Heiz, and M. Tornow: Nonvolatile memristive switching in self-assembled nanoparticle dimers. ACS Applied Electronic Materials **2**(4) (2020), 1099–1105. DOI: 10.1021/acsaelm.0c00099 (cit. on pp. 73–79, 81–83).

[157] J. N. Israelashvili: *Intermolecular and surface forces.* Vol. 3. Oxford: Academic Press, 2011 (cit. on p. 76).

[158] J. Wu, L. Ling, J. Xie, G. Ma, and B. Wang: Surface modification of nanosilica with 3-mercaptopropyl trimethoxysilane: Experimental and theoretical study on the surface interaction. Chemical Physics Letters **591** (2014), 227–232. DOI: 10.1016/j.cplett.2013.11.043 (cit. on p. 76).

[159] S. H. Jo and W. Lu: CMOS compatible nanoscale nonvolatile resistance switching memory. Nano letters **8**(2) (2008), 392–397. DOI: 10.1021/nl073225h (cit. on p. 80).

[160] S. H. Jo, K.-H. Kim, and W. Lu: Programmable resistance switching in nanoscale two-terminal devices. Nano letters **9**(1) (2009), 496–500. DOI: 10.1021/nl803669s (cit. on p. 80).

[161] U. Chand, C.-Y. Huang, D. Kumar, and T.-Y. Tseng: Metal induced crystallized poly-Si-based conductive bridge resistive switching memory device with one transistor and one resistor architecture. Applied Physics Letters **107**(20) (2015), 203502. DOI: 10.1063/1.4935862 (cit. on p. 80).

[162] X. Zhang, S. Liu, X. Zhao, et al.: Emulating Short-Term and Long-Term Plasticity of Bio-Synapse Based on Cu/a-Si/Pt Memristor. IEEE Electron Device Letters **38**(9) (2017), 1208–1211. DOI: 10.1109/LED.2017.2722463 (cit. on p. 80).

[163] A. Younis, D. Chu, C. M. Li, T. Das, S. Sehar, M. Manefield, and S. Li: Interface thermodynamic state-induced high-performance memristors. Langmuir : the ACS journal of surfaces and colloids **30**(4) (2014), 1183–1189. DOI: 10.1021/la404389b (cit. on p. 105).

[164] T. H. Kim, E. Y. Jang, N. J. Lee, D. J. Choi, K.-J. Lee, J.-t. Jang, J.-s. Choi, S. H. Moon, and J. Cheon: Nanoparticle assemblies as memristors. Nano letters **9**(6) (2009), 2229–2233. DOI: 10.1021/nl900030n (cit. on p. 105).

[165] A. Kiazadeh, H. L. Gomes, da Costa, Ana M. Rosa, J. A. Moreira, D. M. d. Leeuw, and S. C. Meskers: Intrinsic and extrinsic resistive switching in a planar diode based on silver oxide nanoparticles. Thin Solid Films **522** (2012), 407–411. DOI: 10.1016/j.tsf.2012.08.041 (cit. on p. 105).

[166] M. Asbahi, S. Mehraeen, F. Wang, N. Yakovlev, K. S. L. Chong, J. Cao, M. C. Tan, and J. K. W. Yang: Large Area Directed Self-Assembly of Sub-10 nm Particles with Single Particle Positioning Resolution. Nano letters **15**(9) (2015), 6066–6070. DOI: 10.1021/acs.nanolett.5b02291 (cit. on p. 105).

[167] M. Speckbacher, X. Xi, and M. Tornow, eds.: *Resistive switching in single core-shell nanoparticles.* Piscataway, NJ: IEEE, 2020. DOI: 10.1109/NANO46743.2019.8993937 (cit. on pp. 105–108, 110).

[168] X. Xi: Memristive phenomena in nanoparticle-based devices. Master's thesis. München: Technische Universität München, 2019 (cit. on p. 105).

[169] E. Linn, R. Rosezin, C. Kügeler, and R. Waser: Complementary resistive switches for passive nanocrossbar memories. Nature materials **9**(5) (2010), 403–406. DOI: 10.1038/nmat2748 (cit. on p. 108).

[170] F. Nardi, S. Balatti, S. Larentis, D. C. Gilmer, and D. Ielmini: Complementary Switching in Oxide-Based Bipolar Resistive-Switching Random Memory. IEEE Transactions on Electron Devices **60**(1) (2013), 70–77. DOI: 10.1109/TED.2012.2226728 (cit. on p. 108).

[171] M. Javadi, Z. Yang, and J. G. C. Veinot: Surfactant-free synthesis of GeO_2 nanocrystals with controlled morphologies. Chemical communications (Cambridge, England) **50**(46) (2014), 6101–6104. DOI: 10.1039/c4cc01490a (cit. on p. 115).

List of publications

The following journal publications and conference contributions evolved from this work.

Journal articles and conference proceedings

- M. Speckbacher, M. Rinderle, W. Kaiser, E. A. Osman, D. Chryssikos, A. Cattani–Scholz, J. M. Gibbs, A. Gagliardi, and M. Tornow: Directed Assembly of Nanoparticle Threshold–Selector Arrays. Advanced Electronic Materials 5(7) (2019), 1900098. doi:10.1002/aelm.201900098
- M. Speckbacher, M. Jakob, M. Döblinger, J. G. C. Veinot, A. Kartouzian, U. Heiz, and M. Tornow: Non-volatile memristive switching in self-assembled nanoparticle dimers. ACS Applied Electronic Materials, 2(4) (2020). 1099–1105, doi: 10.1021/acsaelm.0c00099
- M. Speckbacher, E. A. Osman, J. M. Gibbs, and M. Tornow: Directed self-assembly of silicon nanocubes fabricated by nano imprint-lithography. Piscataway, NJ:IEEE (2018). doi: 10.1109/NANO.2018.8626349
- M. Speckbacher, X. Xi, and M. Tornow: Resistive switching in single core-shell nanoparticles. Piscataway, NJ: IEEE, (2020). doi: 10.1109/NANO46743.2019.8993937
- R. K. Grötsch, C. Wanzke, M. Speckbacher, A. Angi, B. Rieger, and J. Boekhoven: Pathway Dependence in the Fuel-Driven Dissipative Self-Assembly of Nanoparticles. Journal of the American Chemical Society 141(25) (2019), 9872–9878. doi: 10.1021/jacs.9b02004
- A. I. Berg, S. Brivio, S. Brown, et al.: Synaptic and neuromorphic functions: general discussion. Faraday discussions 213(0) (2019), 553–578. doi: 10.1039/C8FD90065E
- J. M. Dlugosch, D. Devendra, D. Chryssikos, S. Artmeier, M. Speckbacher, T. Kamiyama, and M. Tornow: Metallic top contacts to self-assembled monolayers of aliphatic phosphonic acids on titanium nitride. Piscataway, NJ:IEEE (2020), accepted.

Conference presentations

- M. Speckbacher, E. A. Osman, J. M. Gibbs, and M. Tornow: Electrical characterization of self-assembled monolayers for on-chip self-assembly formed by Cu(I)-catalyzed alkyne-azide cycloaddition. (Poster) 2017 CeNS/SFB1032 Workshop Venice: Design and Control of Nanosystems (San Servolo, Venice, Italy)
- M. Speckbacher, E. A. Osman, J. M. Gibbs, and M. Tornow: On-chip self-assembly of nanoparticle threshold selector arrays. (Contributed talk) 2018 International Workshop "Novel Concepts and Electronic Phenomena in Heterosystems" (Tutzing, Germany)
- M. Speckbacher, O. Bienek, and M. Tornow: Conductive filament localization in nanoscale electrochemical metallization cells. (Contributed talk) 2019 E-MRS Fall Meeting (Warsaw, Poland)

Acknowledgments

At this point, i would like to thank everyone who contributed to this work.

In particular, i would like to thank my supervisor Prof. Dr. Marc Tornow for giving me the opportunity to conduct my work in his group and for always supporting me in a very dedicated manner. Thanks for giving me freedom to do exciting research and for always being there for fruitful discussions and guidance on a regular basis.

Next, a special thanks goes to all my colleagues in the group of Molecular Electronics making sure there was always a good atmosphere in the lab, in the office and while visiting conferences: Simon, Julian, Hung, Takuya, Domenikos, Daniel, Kai and Henry. A big thank you also goes to my master student Xinrui Xi showing lots of commitment.

I big thanks to Regina Hutschenreiter, Susanne Maier, Katharina Blahetek, Rosemarie Mittermeier and Peter Weiser, supporting me a lot with administrative issues and in the lab.

A big thank you also goes to all my colleagues from ATUMS in Germany and in Canada, especially to Juli Gibbs, Eiman Osman, Jon and Leah Veinot, Mahmoud Almadhoun, Mori Javadi, Frank Hegmann, Raphael Grötsch, Job Boekhoven, Matthias Jakob and Uli Heiz for fruitful collaborations and an inspiring and exciting time at the UofA and at yearly ATUMS meetings.

I would like to also thank all the people from WSI and ZNN, who were always up for helpful discussions.

Finally, i would like to express a hearty thank you to my wife Tamara, my parents and sister Renate, Peter and Elisabeth, as well as Patricia and Wolfgang and all my friends for supporting me in good and difficult times during my PhD. Without your constant support, all this would not have been possible.